Performance and science reach of the Probe of Extreme Multimessenger Astrophysics for ultrahigh-energy particles

Luis A. Anchordoqui,[1,2,3] Douglas R. Bergman,[4] Mario E. Bertaina,[5] Francesco Fenu,[5] John F. Krizmanic,[6] Alessandro Liberatore,[5] Angela V. Olinto,[7] Mary Hall Reno,[8] Fred Sarazin,[9] Kenji Shinozaki,[5] Jorge F. Soriano,[1,2] Ralf Ulrich,[10] Michael Unger,[10] Tonia M. Venters,[11] and Lawrence Wiencke[9]

[1]*Department of Physics and Astronomy, Lehman College, City University of New York, New York 10468, USA*
[2]*Department of Physics, Graduate Center, City University of New York, New York 10016, USA*
[3]*Department of Astrophysics, American Museum of Natural History, New York 10024, USA*
[4]*High Energy Astrophysics Institute and Department of Physics and Astronomy, University of Utah, Salt Lake City, Utah 84112, USA*
[5]*Dipartimento di Fisica, Universitá di Torino, Torino 10125, Italy*
[6]*CRESST/NASA Goddard Space Flight Center, Greenbelt, Maryland 20771, USA*
University of Maryland, Baltimore County, Baltimore, Maryland 21250, USA
[7]*Department of Astronomy & Astrophysics, KICP, EFI, The University of Chicago, Chicago, Illinois 60637, USA*
[8]*Department of Physics and Astronomy, University of Iowa, Iowa City, Iowa 52242, USA*
[9]*Department of Physics, Colorado School of Mines, Golden, Colorado 80401, USA*
[10]*Institut für Kernphysik, Karlsruher Institut für Technologie, 76021 Karlsruhe, Germany*
[11]*Astrophysics Science Division, NASA Goddard Space Flight Center, Greenbelt, Maryland 20771, USA*

(Received 25 October 2019; published 24 January 2020)

The Probe of Extreme Multimessenger Astrophysics (POEMMA) is a potential NASA Astrophysics Probe-class mission designed to observe ultrahigh-energy cosmic rays (UHECRs) and cosmic neutrinos from space. POEMMA will monitor colossal volumes of the Earth's atmosphere to detect extensive air showers (EASs) produced by extremely energetic cosmic messengers: UHECRs above 20 EeV over the full sky and cosmic neutrinos above 20 PeV. We focus most of this study on the impact of POEMMA for UHECR science by simulating the detector response and mission performance for EAS from UHECRs. We show that POEMMA will provide a significant increase in the statistics of observed UHECRs at the highest energies over the entire sky. POEMMA will be the first UHECR fluorescence detector deployed in space that will provide high-quality stereoscopic observations of the longitudinal development of air showers. Therefore it will be able to provide event-by-event estimates of the calorimetric energy and nuclear mass of UHECRs. The particle physics in the interactions limits the interpretation of the shower maximum on an event-by-event basis. In contrast, the calorimetric energy measurement is significantly less sensitive to the different possible final states in the early interactions. POEMMA will increase by a factor of 30 fluorescence observations, with accurate measurements of the *shower maximum*. We study the prospects to discover the origin and nature of UHECRs using expectations for measurements of the energy spectrum, the distribution of arrival direction, and the atmospheric column depth at which the EAS longitudinal development reaches maximum. We also explore supplementary science capabilities of POEMMA through its sensitivity to particle interactions at extreme energies and its ability to detect ultrahigh-energy neutrinos and photons produced by top-down models including cosmic strings and superheavy dark matter particle decay in the halo of the Milky Way.

DOI: 10.1103/PhysRevD.101.023012

I. INTRODUCTION

After over 80 years of the first measurement of extensive air showers (EASs) by Pierre Auger [1], the astrophysical sources of these extremely energetic cosmic rays remain unknown. Ultrahigh energy (UHE) cosmic rays (CRs) have been observed with energies $E \gtrsim 10^{20}$ eV $\equiv 100$ EeV, which is more than 7 orders of magnitude higher than what the LHC beam can currently achieve. The nature

of the astrophysical sources and their acceleration mechanism(s) remains a mystery [2–4]. The understanding is further muddled by the uncertainty in the nuclear composition of UHECRs above 50 EeV.

A succession of increasingly sized ground-based experiments has led to the Pierre Auger Observatory (Auger) [5,6], with an exposure $\mathcal{E} \sim 65\,000$ km^2 sr yr collected in 15 years of operation [7], and the Telescope Array (TA) [8,9], with $\mathcal{E} \sim 10\,000$ km^2 sr yr collected in 10 years. Both of these experiments have precisely measured key features in the UHECR spectrum: a pronounced hardening around 5 EeV (the so-called "nkle"feature) and a suppression of the flux above about 40 EeV [10–13]. The differential energy spectra measured by TA and Auger agree within systematic errors below 10 EeV. However, even after energy rescaling, a large difference remains at and beyond the flux suppression [14].

The EAS longitudinal development is characterized by the number of particles as a function of the atmospheric column depth X in g/cm^2. A well-defined peak of the longitudinal profile is observed when the number of $e^{\pm}$ in the electromagnetic shower is at its maximum. This shower maximum or $X_{\rm max}$ becomes a powerful observable for studying the UHECR nuclear composition. This is because breaks in the elongation rate—the rate of change of $\langle X_{\rm max}\rangle$ per decade of energy—can be related to changes in the nuclear composition [15,16], even when uncertainties in the UHE particle physics limit the accuracy of mapping between $X_{\rm max}$ and the nucleus baryon number A.

At around the ankle, the measurements of $X_{\rm max}$ by TA [17,18] and Auger [19–22] are both consistent with a predominantly light composition. For $E \gtrsim 10$ EeV, Auger data show both a significant decrease in the elongation rate and a decrease of the shower-to-shower fluctuations of $X_{\rm max}$ with energy. These two effects indicate a gradual increase of A with rising energy. Indeed, at $E \approx 30$ EeV the interpretation of Auger data with LHC-tuned hadronic interaction models leads to $A \approx 14$–20. The Auger and TA collaborations have also conducted a thorough joint analysis concluding that at the current level of statistics and understanding of systematics, both data sets are compatible with being drawn from the same parent distribution [23,24]. Above about 10 EeV TA data are compatible with a pure protonic composition, but also with the mixed composition determined by the Auger Collaboration [23,24]; Auger data are more constraining and not compatible with the pure protonic option available with TA alone. Moreover, the Auger Collaboration has reported additional model-independent evidence for a mixed nuclear composition around the ankle in the correlations between $X_{\rm max}$ and the shower size at ground [25]. All in all, while there remain some differences in the details of composition measurements between Auger and TA, Auger has provided evidence of heavier composition with increasing energies above 10 EeV and TA measurements are not in contradiction with that interpretation.

UHECR deflections by intervening magnetic fields constitute the main challenge for source identification. The typical deflection of UHECRs in the extragalactic magnetic field, $B \sim 1$ nG [26], can be estimated to be

$$\theta_{\rm eg} \approx 1.5^\circ Z \sqrt{\frac{d}{3.8\ {\rm Mpc}}\frac{\lambda}{0.1\ {\rm Mpc}}}\frac{B}{\rm nG}\left(\frac{E}{10\ {\rm EeV}}\right)^{-1}, \quad (1)$$

where d is the source distance, λ the magnetic field coherence length, and Z the charge of the UHECR in units of the proton charge [27,28]. Typical values of the deflections of UHECRs crossing the Galaxy are somewhat larger [29],

$$\theta_{\rm G} \sim 10^\circ Z\left(\frac{E}{10\ {\rm EeV}}\right)^{-1}, \quad (2)$$

preventing small-scale clustering with directional pointing to the sources. However, individual sources could still be isolated in the sky if the UHECR flux is dominated by the contribution of a limited number of sources. Indeed, the reduction of the UHECR horizon, because of the so-called "Greisen-Zatsepin-Kuzmin (GZK) interactions" on the cosmic microwave background (CMB) [30,31], implies that fewer and fewer sources contribute to the flux at higher and higher energy.

Assuredly, the most recent result concerning the origin of UHECRs has been the discovery (statistical significance $>5\sigma$) of a large-scale hemispherical asymmetry in the arrival direction distribution of events recorded by Auger [32,33]. The data above 8 EeV are well represented by a dipole with an amplitude $A = (6.5^{+1.3}_{-0.9})\%$ pointing in the direction $(l, b) = (233^\circ, -13^\circ) \pm 10^\circ$ in galactic coordinates, favoring an extragalactic origin for UHECRs. However, Auger and TA data have yielded only a few clues to the precise location of the sources. For instance, the TA Collaboration has reported an excess above the isotropic background-only expectation in cosmic rays with energies above 57 EeV [34]. In addition, searches in Auger data revealed a possible correlation with nearby starburst galaxies, with a (post-trial) 4σ significance, for events above 39 EeV [35]. The smearing angle and the anisotropic fraction corresponding to the best-fit parameters are $13^{+4^\circ}_{-3}$ and $(10 \pm 4)\%$, respectively. The energy threshold coincides with the observed suppression in the spectrum, implying that when we properly account for the barriers to UHECR propagation in the form of energy loss mechanisms [30,31] we obtain a self-consistent picture for the observed UHECR horizon. With current statistics the TA Collaboration cannot make a statistically significant corroboration or refutation of the starburst hypothesis [36]. A slightly weaker association (2.7σ) with active galactic nuclei emitting γ rays (γAGN) is also found in Auger events

above 60 EeV [35]. For γAGN, the maximum deviation from isotropy is found at an intermediate angular scale of $7^{+4^\circ}_{-2}$ with an anisotropic fraction of $(7 \pm 4)\%$.

Extremely fast spinning young pulsars [37–39], active galactic nuclei (AGNs) [40–43], starburst galaxies (SBGs) [44–46], and gamma-ray bursts [47–54] can partially accommodate Auger and TA observations, but a convincing unified explanation of all data is yet to be realized. What is clearly needed is a more dramatic increase in UHECR exposure. The Probe of Extreme Multimessenger Astrophysics (POEMMA) will accomplish this by using space-based UHECR observations with excellent angular, energy, and nuclear composition resolution [55]. In addition, both Auger and TA are undergoing upgrades. TA × 4 is designed to cover the equivalent of Auger's aperture [56]. Auger's upgrade ("ugerPrime"[57]) focuses on more detailed measurements of each shower observed. This will enable event-by-event probabilistic composition assignment (hence, selection of low-Z events).

In this paper we investigate the sensitivity of POEMMA to address challenges of UHECR astrophysics and explore the potential of this experiment to probe fundamental physics. The layout of the paper is as follows. In Sec. II we provide an overview of the POEMMA design and the mission specifications. Aspects of the simulated detector response are discussed in Sec. III and the POEMMA UHECR performance is studied in Sec. IV. After that, in Sec. V we examine the POEMMA science reach. We also evaluate whether the UHECR capabilities of POEMMA for baryonic cosmic rays are also applicable to fluorescence detection of extreme energy photons and ultrahigh-energy neutrino interactions deep in the atmosphere. Finally, we summarize our results and draw our conclusions in Sec. VI.

II. THE POEMMA EXPERIMENT

The POEMMA instruments and mission leveraged from previous work developed for the Orbiting Wide-field Light-collectors (OWL) mission [58], together with the experience on the fluorescence detection camera for the Joint Experimental Missions of the Extreme Universe Space Observatory (JEM-EUSO) [59], and the recently proposed CHerenkov from Astrophysical Neutrinos Telescope concept [60] to form a multimessenger probe of the most extreme environments in the Universe.

POEMMA was selected by NASA as one of the several concept study proposals to provide science community input for a new class of NASA missions, called astrophysics probes. Such astrophysics probes will be examined by the 2020 Astronomy and Astrophysics Decadal Survey in support of the development of a recommended portfolio of future astrophysics missions.[1] The astrophysics probe mission concepts were funded for 18-month studies, including week-long dedicated engineering study runs. The POEMMA study was performed at the Instrument Design Lab and the Mission Design Lab in the Integrated Design Center at NASA/GSFC [61]. The probe studies were developed with specific instructions to define this unique NASA Class B mission, including phase A start date (October 1, 2023), launch date (November 1, 2029), and launch vehicle guidance, with a total lifecycle (NASA phases A through E) costs between 400M and 1B in FY2018 dollars. In this context, POEMMA is considered as a potential probe mission in terms of the 2020 astrophysics decadal review assessment of the probe-class concept. In this section we provide a summary of the POEMMA mission specifications developed under the probe study.

A. Instrument design

Building on the OWL study [58], POEMMA is composed of two identical satellites flying in formation with the ability to observe overlapping atmospheric volumes during nearly moonless nights in configurations ranging from nadir viewing to that just above the limb of the Earth. The satellites will fly at an altitude of about 525 km with separations ranging from 300 km for stereo fluorescence UHECR observations to 25 km when pointing at the Earth's limb for both fluorescence and Cherenkov observations of UHECRs and cosmic neutrinos. Each POEMMA satellite consists of a 4-meter diameter Schmidt telescope with a fast ($f/0.64$) optical design. The optical effective area ranges from 6 to 2 m^2 depending on the angle of incidence of the signal. The visible portion of the EAS disk is a few hundred meters wide and determines the required pixel angular resolution in the Schmidt telescope focal plane: a spatial size of 1 km from 525 km leads to pixel angular resolution of ∼0.1° to accurately view the EAS development. Each POEMMA telescope monitors a substantial 45° field of view (FoV) with fine pixel angular resolution of 0.084° and a refractive aspheric aberration corrector plate. A lens-cap lid (or shutter door) and a cylindrical light shield shroud protect the mirror from stray light and micrometeoroids. The mirrors act as large light collectors with modest imaging requirements; i.e., the POEMMA optics imaging requirements are ∼10^4 away from the diffraction limit. The primary mirror is 4 m diameter, whereas the corrector lens 3.3 m diameter. The concept of the POEMMA photometer and spacecraft is shown in Fig. 1.

The POEMMA focal surface (1.6 m diameter) is composed of a hybrid of two types of cameras: over 85% of the focal surface is dedicated to the POEMMA fluorescence camera (PFC), while the POEMMA Cherenkov camera (PCC) occupies the crescent moon shaped edge of the focal surface, which images the limb of the Earth. The PFC is composed of the EUSO designed

[1]NASA Research Announcement Astrophysics Probe Mission Concept Studies, Solicitation: NNH16ZDA001N-APROBES.

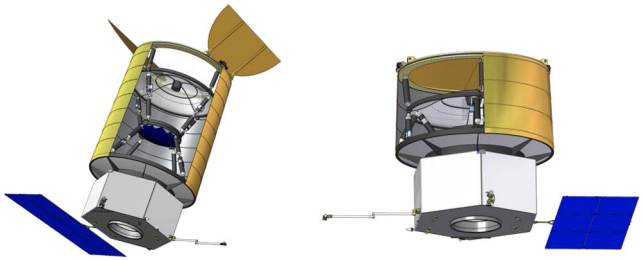

FIG. 1. Schematic representation of POEMMA (photometer and spacecraft) deployed with open shutter doors (left) and in stowed position for launch (right). Cutaways in the light shield display the internal structure of corrector plate and focal surface in the middle of the payload (blue). The spacecraft bus is shown with solar panel (blue) and communications antenna deployed in both images.

Photo Detector Modules (PDM) based on multianode photomultiplier tubes (MAPMTs) as flown in suborbital missions in EUSO-Balloon [62], EUSO-SPB1 [63], and EUSO-SPB2 [64], and in the mini-EUSO [65] and CALET [66] experiments onboard the International Space Station. The sampling time between images for the PFC is 1 μs. The much faster PCC is composed of silicon photomultipliers (SiPMs) designed to detect the 10 to 100 ns Cherenkov flashes. The PFC registers UHECR tracks from near the nadir when the in stereo mode extended to just below the Earth's limb when in the tilted neutrino mode, where the PCC registers light within the Cherenkov emission cone of up-going showers around the limb of the Earth and also from UHECRs above the limb of the Earth. A schematic representation of the POEMMA's hybrid focal surface is shown in Fig. 2.

B. Mission synopsis

The POEMMA mission involves two satellites flying in formation in a relatively low-altitude (525 km), near-equatorial orbit (28.5° inclination). Each satellite operates independently and telemeters data to the ground for combined analysis. Both satellites will be launched in a stowed configuration on a single launch vehicle. Once on orbit, the telescopes will be deployed along with the solar array, light shield, and communications antenna. The mirror and data module are attached to the satellite bus.

Both satellites will be launched as a dual manifest in an Atlas V using the long payload fairing. The satellites will be inserted into a circular orbit at an inclination of about 28.5° and an initial altitude of 525 km and a separation of 300 km. The most common flight configuration will be the UHECR stereo observation mode. The target-of-opportunity (ToO) observing mode will involve the instruments slewing to view the celestial source location as well as a maneuver to closer distance such that both satellites observe the same Cherenkov signal from Earth-skimming neutrinos from the transient source [67] for long-duration

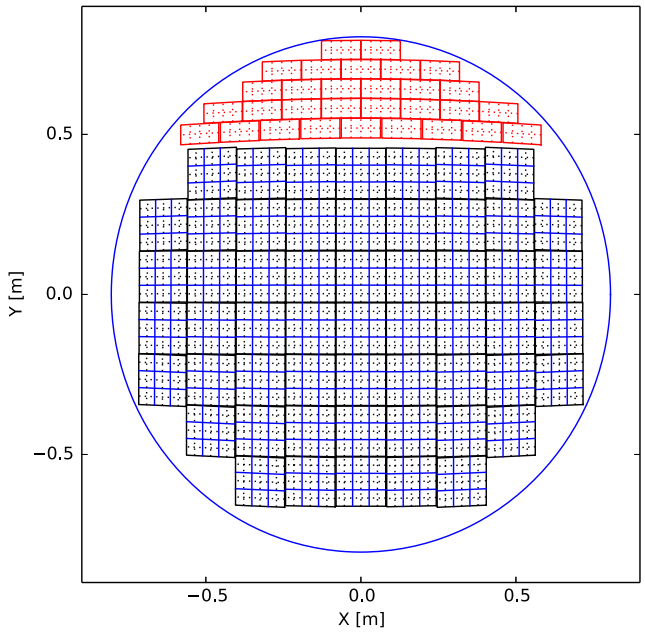

FIG. 2. POEMMA's hybrid focal surface of 1.6 m diameter. The PFC (blue), composed of 55 photodetector modules (PDMS; total 126,720 MAPMT pixels) with 1 μs time gates, and the PCC (red) with 28 SiPM focal surface units. The PCC observes a solid angle of 9° by 30° to monitor the Earth's limb for up-going EASs.

(>1 day) bursts. Once extreme transient event alerts are received, for example, from the gravitational wave signature of a binary neutron-star merger, the satellites will maneuver to a closer separation distance of about 25 km and an appropriate attitude and slew to follow the ToO of the transient source as it rises and sets over the Earth's limb. While the PCC is searching for neutrinos from the ToO, each PFC continues to observe UHECRs in a common volume, providing two correlated monocular views of EASs. A sequence of observing formation stages, varying between stereo and ToO modes, will be planned to address each science goal for the minimum 3-year mission with a 5-year mission goal.

III. SIMULATED DETECTOR RESPONSE

POEMMA's two identical satellites fly in formation to observe EASs in two different modes: precision UHECR stereo mode and a tilted configuration, denoted as neutrino mode, when also viewing τ-lepton EASs sourced near the Earth's limb. In stereo mode, the UHECR measurement performance is optimized by separating the POEMMA satellites by 300 km and tilted slightly away from the nadir for each to view a common area and stereoscopically reconstruct the EASs from UHECRs. In neutrino mode, the satellites slew to view the source and are separated by 25 km to put both in the Cherenkov light pool from the upward-moving τ-lepton EASs, using the PCCs, and also measure UHECRs using the PFCs with a higher geometry

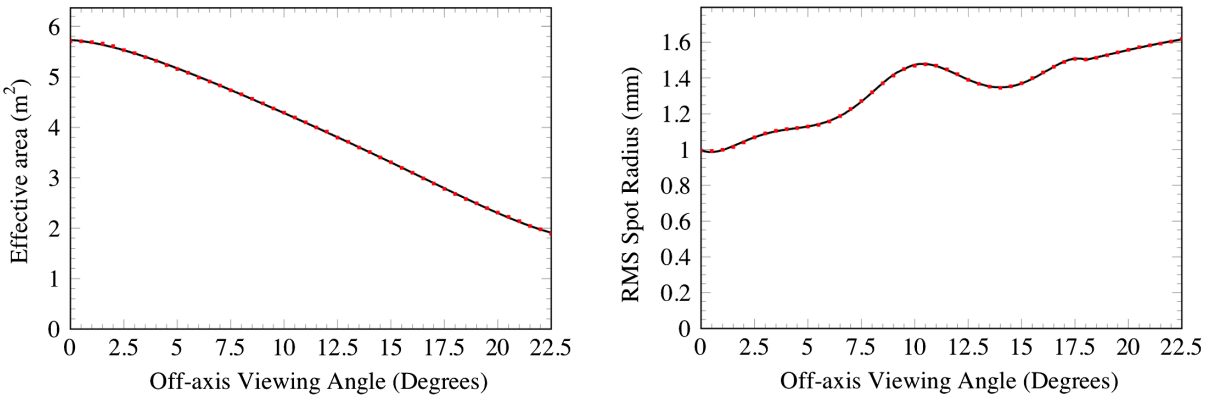

FIG. 3. The effective area (left) and the root mean square (RMS) spot radius (right) as a function of viewing angle for a POEMMA Schmidt telescope.

factor, but reduced performance due to the more monocularlike UHECR reconstruction response. Note that both instruments also view a common atmospheric volume in limb-viewing mode. Here we detail the two separate simulations used to determine the stereo and monocular UHECR performance.

Both simulations use the same parametric optical models derived from ray tracing optical design software (ZEMAX) [68]. Each satellite carries a Schmidt telescope with a 3.3-meter diameter optical aperture, defined by the corrector lens, and 45° full FoV. In Fig. 3 we show the effective area and RMS spot radius as a function of the viewing angle. The effective area includes the effects of the transmission through the corrector lens (94% transmission) and mirror reflectivity (95%).

A. Stereo simulations

The UHECR simulated stereo response was performed using an end-to-end simulation originally developed for the OWL [58] study but updated for POEMMA. The simulation assumes an isotropic UHECR flux impinging the Earth and uses a fast EAS generator [69] that provides the one-dimensional EAS profiles as Gaisser-Hillas functions [70]. POEMMA's 0.084° focal plane pixel FoV translates to a spatial distance of ~0.8 km at sea level for nadir viewing from an altitude of 525 km, indicating that the one-dimensional EAS modeling is a good approximation. Starting point fluctuations of the EAS are included and the EAS generator can model any nuclei. A comparison of proton primaries to that produced by the CONEX [71] one-dimensional EAS simulation using QGSJETII-04 is shown in Table I.

A detailed atmospheric model is required to define the EAS development, the fluorescence light generation, the generated and scattered Cherenkov light emission, and the fluorescence and Cherenkov light attenuation based on an optical depth between the EAS and POEMMA observations. We employ a static, baseline model for the definition of the atmosphere profile using the model of Shibata [72] to define the overburden and density. The temperature profile, needed to account for the altitude dependence of the fluorescence yield, is taken from the 1976 standard atmosphere while the index of refraction of air uses a parametric model of Hillas [73]. The fluorescence light is generated in the wavelength band from 282 to 523 nm based on the measured relative yields from each specific line [74,75], with the total fluorescence yield defined by recent measurements compiled by the Particle Data Group [76]. The pressure and temperature dependence of the fluorescence emission uses the model of Kakimoto *et al.* [77]. For simulating the PFC response, Cherenkov light is generated in the wavelength band 200–600 nm in bins of 25 nm based on a standard prescription [78].

The fluorescence and Cherenkov light attenuation includes the effects of Rayleigh scattering [79] and ozone absorption. The Earth's ozone layer efficiently attenuates optical signals at shorter wavelengths ($\lambda \lesssim 330$ nm). An ozone attenuation model [80] is used with an altitude dependent profile derived from Total Ozone Mapping Spectrometer measurements [81]. The optical fluorescence

TABLE I. Comparison of the POEMMA EAS simulation based on the distributions from 1000 modeled proton UHECRs with 30° zenith angle to that from CONEX.

EAS energy (EeV)	POEMMA N_{max}	CONEX N_{max}	POEMMA X_{max} (g/cm^2)	CONEX X_{max} (g/cm^2)
1	$6.30 \pm 0.27 \times 10^8$	$6.15 \pm 0.22 \times 10^8$	750 ± 62	739 ± 70
10	$6.12 \pm 0.21 \times 10^9$	$6.10 \pm 0.19 \times 10^9$	815 ± 58	793 ± 62
100	$5.91 \pm 0.18 \times 10^{10}$	$5.94 \pm 0.20 \times 10^{10}$	868 ± 53	849 ± 60

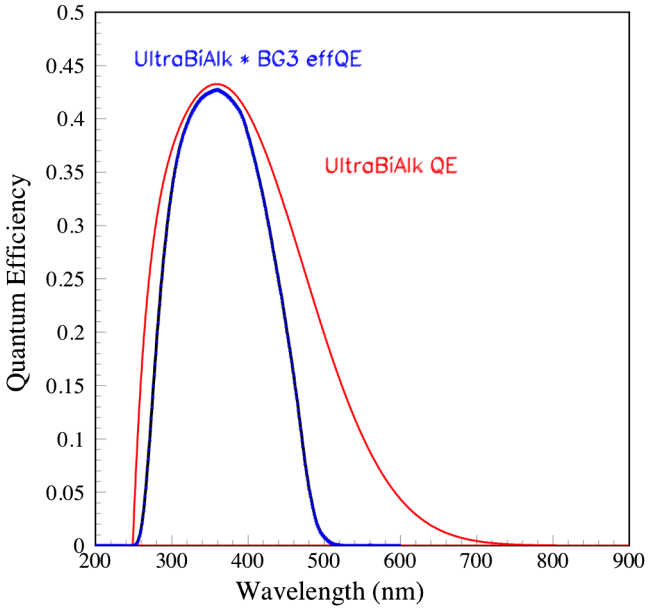

FIG. 4. The QE as a function of wavelength used to model the PFC response as well as the effective QE after taking into account the transmission of the BG3 UV filter.

and (scattered) Cherenkov wavelength dependent signals delivered to the POEMMA satellites at 525 km altitude are then convolved with a model of performance of each POEMMA Schmidt telescope.

The effective area and RMS point-spread function (PSF) are modeled using a parametric description based upon the optical design that relies on ray tracing. The wavelength-dependent signals are attenuated by a UV filter and then mapped onto a POEMMA focal plane assuming 3-mm spatial pixel size. The quantum efficiency (QE) of the photodetector is modeled using the wavelength dependence based on that reported by the manufacturer (Hamamatsu). The incident angle of the EAS optical signal determines the effective collecting area and the PSF of the optics; these are used to then generate photoelectrons (PE) by using Poisson statistics after accounting for the bandpass of the BG3 UV filter and QE of the photodetectors (see Fig. 4). This process uses 1 μs sampling time to record the EAS signals while also providing the integrated EAS profile in the POEMMA focal planes.

We have performed detailed simulation studies using POEMMA's optical performance to determine POEMMA's UHECR exposure, angular resolution, and nuclear composition ($X_{\max}$) resolution. For the stereo UHECR mode, we modeled a satellite configuration with a 300-km separation and tilted ($\pm 12.2°$) to view a common atmospheric volume between the two satellites. The PFC instrument response model is derived from the ESAF simulations (described in the Appendix A), which take into account the effects of air glow background, the PFC trigger, and electronic response. A single POEMMA telescope pointing in the nadir mode was modeled using the methodology of the stereo simulation. The UHECR event selection was then tuned by setting requirements on the number of pixels above a PE threshold to achieve a similar trigger UHECR aperture as reported by the ESAF simulations; see Appendix A. This condition was then used for the modeling of POEMMA's stereo response for the condition of separating the satellites by 300 km and tilting them to view a common volume of atmosphere between them.

Each measured EAS trajectory in the POEMMA focal planes defines a unique geometrical plane. Simple geometry determines a line in three-dimensional space where these two planes intersect, corresponding to the EAS trajectory. As long as the opening angle between these planes is larger than $\sim 5°$, the reconstruction of the EAS trajectory is robust, due to POEMMA's excellent EAS pixel angular resolution, yielding superb UHECR angular resolution. Figure 5 shows POEMMA's stereo reconstructed angular resolution, which is $\sim 1°$ or better above 30 EeV, and highlights the strength of the stereo reconstruction technique when one has good pixel angular resolution. In

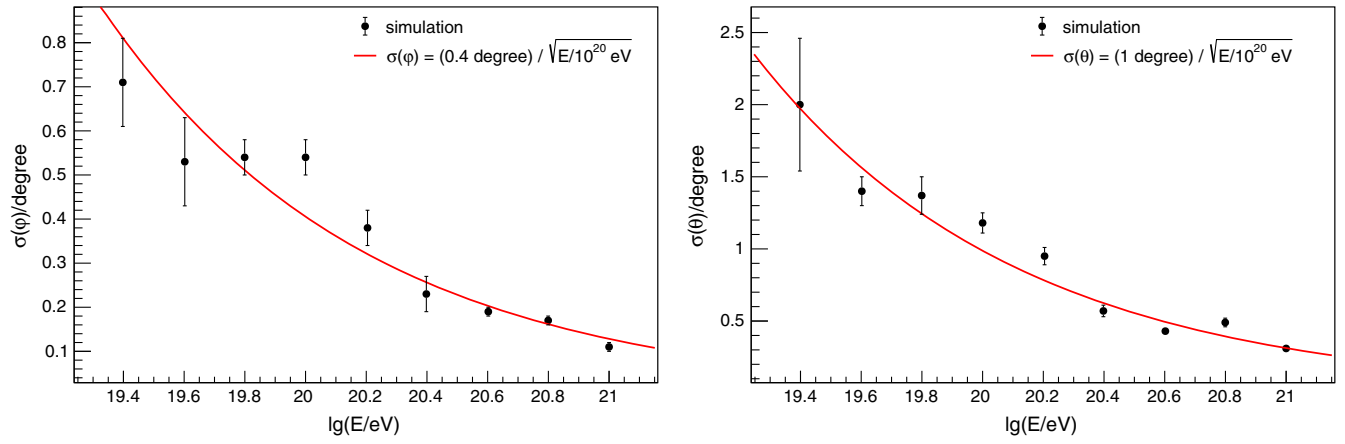

FIG. 5. POEMMA's simulated stereo-reconstructed angular resolution versus UHECR energy: left, azimuth angle; right, zenith angle.

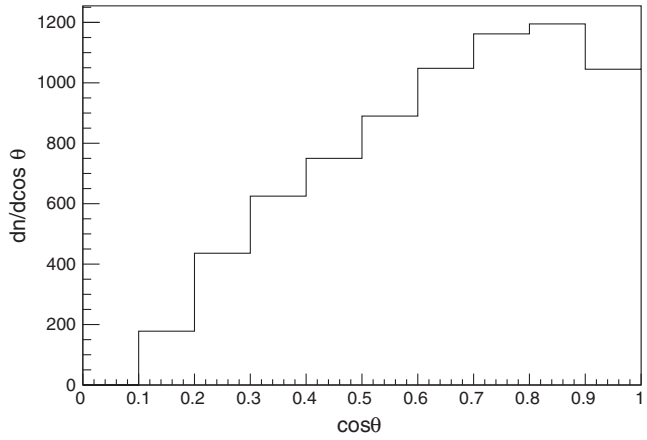

FIG. 6. Distribution of zenith angles of triggered events above 50 EeV.

Fig. 6 we show zenith angle distribution of triggered events above 50 EeV and in Fig. 7 we show an example 50 EeV UHECR as measured in the POEMMA focal planes.

The stereo trigger condition in each satellite leads to a highly efficient reconstruction fraction of ∼80%, with the losses due mainly to the requirement of the ∼5° opening angle between each EAS geometrical plane. To estimate the energy resolution in stereo mode we performed simulations with ESAF in monocular mode (see Appendix A), assuming $\sigma = 1°$ angular resolution in both zenith and azimuth angles based on the results of the stereo reconstruction (see Fig. 5). This leads to a resolution of 26% and 24% at 50 and 100 EeV, respectively. Since the two satellites provide an independent measurement of the same EAS, the resolution can be expected to be a factor of $\sqrt{2}$ better than the monocular one with fixed geometry, i.e., 18% and 17% at 50 and 100 EeV, respectively. It is worthwhile noting that these numbers can be considered conservative, because the ESAF simulations used a lower quantum efficiency and a larger time binning (2.5 μs) than will be used in POEMMA (1 μs). A partial estimate of the $X_{\max}$ resolution is evaluated by considering the effects of the finite PE statistics when reconstructing the shower profile. The results, shown in Fig. 8, give an $X_{\max}$ resolution of 20 g/cm^2 at 30 EeV. The $X_{\max}$ resolution is further degraded by effects of angular resolution and acceptance. We consider all these effects in Sec. IV to estimate the total $X_{\max}$ resolution.

POEMMA is expected to operate also in tilt mode when observing the Cherenkov signal from tau neutrinos and also to exploit different combinations of stereoscopic vision. By tilting the instrument the EAS distance increases and therefore the energy threshold of the instrument increases as well. Moreover, it is expected that the background increases as the column density of air glow emitting layer increases with the tilt angle. This is taken into account assuming that such an increase is proportional to $\cos(\theta)^{-1}$. In Fig. 9 we exhibit the UHECR proton aperture, after taking into account event reconstruction efficiency, for stereo viewing, as well as that when the satellites are tilted by 47° for the condition when POEMMA is viewing the limb of the Earth in neutrino mode. The stereo results are based on the stereo POEMMA simulation, whereas the 47° tilted mode results are based on the ESAF simulation using monocular reconstruction of POEMMA.

B. Duty cycle and exposure

The estimation of the UHECR exposure of a space-based experiment like POEMMA requires accounting for: (i) the characteristics of the EAS development in the atmosphere

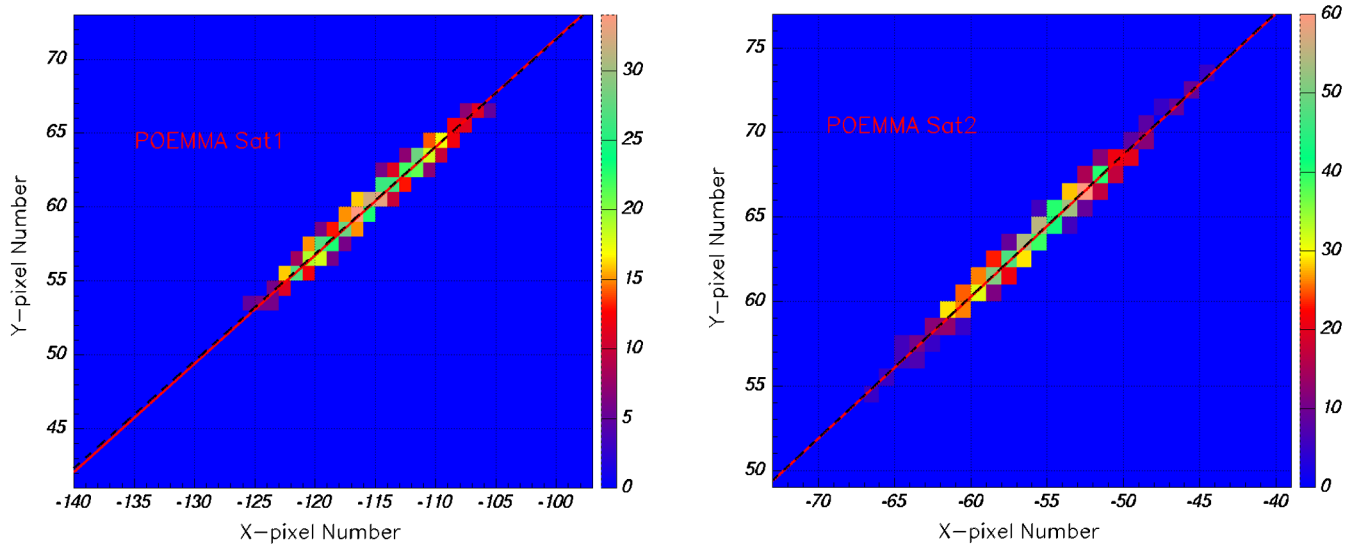

FIG. 7. A stereo reconstructed 50 EeV UHECR in the two POEMMA focal planes. The solid line denotes the simulated trajectory while the dashed line shows the reconstructed trajectory. The color map provided the photoelectron statistics in each pixel.

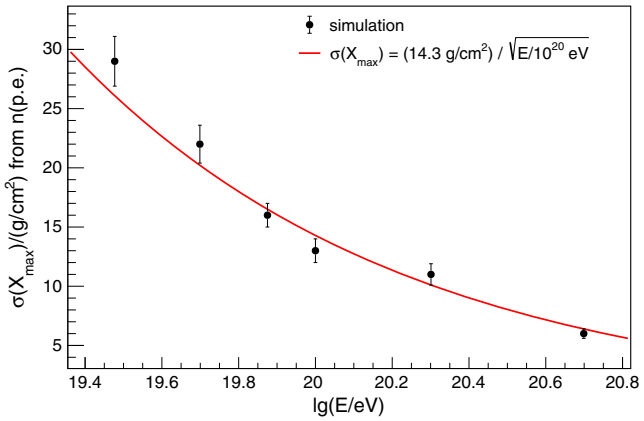

FIG. 8. Single-photometer $X_{\max}$ resolution from photoelectron statistics.

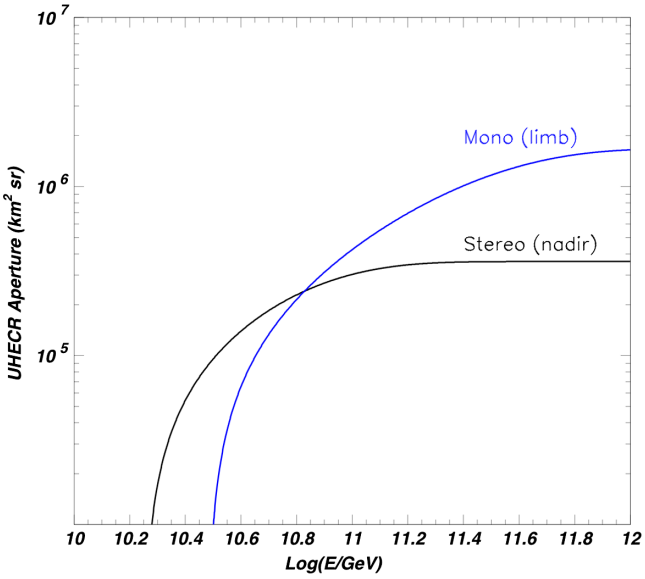

FIG. 9. The simulated UHECR aperture after event reconstruction for POEMMA for the stereo mode and tilted mode.

as observed from space, (ii) the properties of the telescope, including its orbit and FoV, (iii) the various sources of *steady* background like night glow and moonlight, (iv) the overall optical transmission properties of the atmosphere, in particular, the possible presence of clouds, and (v) the effect of anthropogenic light, or other light sources such as transient luminous events (TLEs) and meteors. Topics (i) and (ii) are the principal factors determining the threshold in energy and the maximum aperture of the telescope. Topic (iii) limits the observational duty cycle of the mission. Topics (iv) and (v) affect the instantaneous aperture of the telescope. The role of each of the above-listed aspects has been studied in the past to evaluate their contribution to the determination of the JEM-EUSO exposure. A detailed description of such studies was reported in [59].

The observational duty cycle of POEMMA is the fraction of time in which the EAS measurement is not hampered by the brightness of the atmosphere. The atmospheric brightness, which is mainly due to the night-glow and backscattered moonlight, is variable over time. We define the observational duty cycle as the fraction of time η_0 in which the background intensity $I_{\rm BG}$ is lower than a given value $I_{\rm BG}^{\rm thr}$. The moonless condition is assumed to be $I_{\rm BG} = 500$ photons $\mathrm{m}^{-2}\,\mathrm{sr}^{-1}\,\mathrm{ns}^{-1}$ in the range $300 < \lambda/\mathrm{nm} < 500$. This produces a signal of $\sim$1.5 photoelectron $\mathrm{pixel}^{-1}\,\mu\mathrm{s}^{-1}$ for POEMMA. To remain conservative, herein we adopt $I_{\rm BG}^{\rm thr} = 1{,}500$ photons $\mathrm{m}^{-2}\,\mathrm{sr}^{-1}\,\mathrm{ns}^{-1}$. In this condition, the signal of a 100 EeV shower is still more than fives times brighter than the background level well around the shower maximum. The backscattered moonlight is calculated from the moon phase and its apparent position as seen from the POEMMA orbit. The zenith angle of the Sun is required to be greater than 109° for an orbiting altitude of 525 km. The observational duty cycle $\eta_0(I_{\rm BG} < I_{\rm BG}^{\rm thr})$ is of the order of $\sim$20%. This value is actually conservative at $E \gtrsim 100$ EeV, where it is possible to also operate in higher background levels.

Another source of background is the UV emission produced by direct particles interacting in the detector, particularly with the corrector lens due to its large size and transparency. For the JEM-EUSO mission, which was designed to use three lenses, the increase of UV light due to this contribution was determined to be negligible ($\sim$1%). This will also be the case for POEMMA. A point worth noting at this juncture is that this estimate takes into account the UV emission in the corrector lens due to trapped electrons in the center of the South Atlantic anomaly, where the flux of particles exceeds by orders of magnitude the average value.

In addition to the diffuse sources of background, there are transient or steady local sources, such as lightning and TLEs, auroras or city lights. To estimate the effect of lightning and TLEs, we consider the rate of events detected by the Tatiana satellite [82]. We find this prevents observation by $\sim$4%, simply scaling the JEM-EUSO estimated value [59] by taking into account the longer residence time of POEMMA in the equatorial and tropical regions, which are the most active ones for lightning phenomena. This scaling does not take into account the double counting due to the fact that the presence of lightning is very often associated with the presence of high clouds. This is explicitly done to reinforce the conservative nature of our calculation. Because of the POEMMA equatorial orbit the presence of auroras is negligible. This was evaluated for JEM-EUSO (ISS orbit) and even in the case of maximum solar activity, the effect is of the level of $\sim$1%.

To evaluate the effect of light sources on the Earth, which are mainly anthropogenic, we use the Defense Meteorological Satellite Program database. To remain

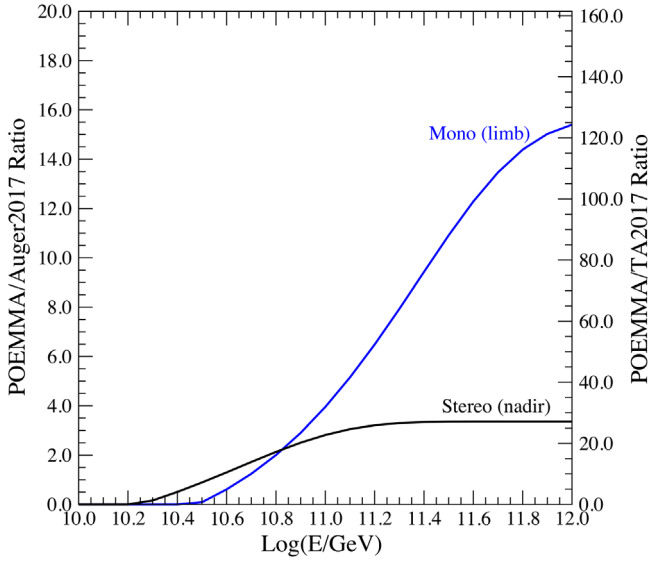

FIG. 10. Examples of the 5-year POEMMA stereo and tilted monocular UHECR exposure in terms of Auger exposure and TA until ICRC-2017.

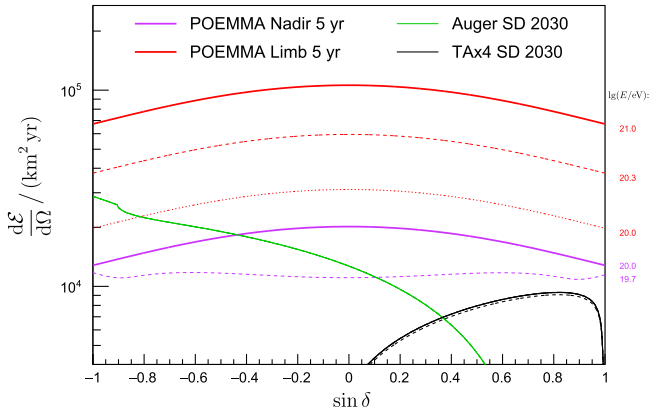

FIG. 11. Differential exposure as a function of declination in different modes, assuming a single-mode operation for the full 5-year benchmark. Purple curves denotes the stereo (near-nadir) mode at $10^{19.7}$ (dashed) and 10^{20} eV (solid). Red curves denote the limb-viewing mode at 10^{20} (dashed), $10^{20.3}$ (dash), and 10^{21} eV (solid). The exposures of the surface detectors of Auger and TA (including the TA × 4 upgrade) assuming being in operation until 2030 are shown as green and black curves, respectively.

conservative, in the study for JEM-EUSO it was assumed that no measurement of EASs is performed if, in a region viewed by a PDM, there is at least one pixel which detects a light intensity which exceeds the average level by a factor of 3 or more. The average level of intensity essentially corresponds to the typical condition on oceans. With this assumption, the inefficiency of the instantaneous aperture is about 7%. For POEMMA, the FoV of a PDM is four times larger, but the trigger logic works at the elementary cell (EC) level, which is 1/9 of a PDM. Therefore, by assuming the same rule at EC level, the above results for JEM-EUSO remain anyway conservative also for POEMMA.

In order to quantify the reduction of the effective instantaneous aperture of the telescope due to the presence of clouds, a study on the distribution of clouds as a function of top altitude H_C, optical depth τ_C, and geographical location was performed using several meteorological data sets and reported in [83]. Showers were simulated using ESAF according to the matrix of cloud occurrence determining the trigger efficiency in the different conditions, and obtaining the corresponding aperture to estimate the ratio κ_C between the aperture when the role of clouds is included, compared to purely clear atmosphere. Selecting the cases of clouds with $\tau_C < 1$, or shower maximum above the cloud-top altitude (i.e., $H_{max} > H_C$) leads to $\kappa_C \sim 72\%$ almost independently of energy [59,83].

All of the above factors give an overall conversion factor from geometrical aperture to exposure of about 13% for POEMMA at 525 km. Based on the UHECR stereo and tilted monocular UHECR apertures, we calculate the POEMMA 5-year exposures, for both stereo (nadir) and mono (limb) configurations, compared to the Auger and TA exposures reported at the 2017 ICRC conference [7,84]. Both the stereo and monocular reconstruction studies show an 80% reconstruction efficiency and a 13% duty cycle based on adapting JEM-EUSO studies assumed for POEMMA observations. In Fig. 10 we show the 5-year POEMMA exposures in relation to Auger and TA.

Apart from the effect of the clouds, the sky coverage of the POEMMA exposure is determined by its orbit and the observable dark night time for a given direction in the celestial sphere. The uniformity over the right ascension slightly deviates from the uniformity due to the seasonal variation of the time that POEMMA stays in the Earth's umbra per orbital period, which is longest around equinoxes. An effect of the Earth's orbit eccentricity appears as the excess in the observation time for the winter time in the Southern hemisphere when the Earth revolves at the slowest velocity.

The differential distribution of the exposure is primarily expressed as a function of the declination. As can be seen in Fig. 6, at lower energies the trigger efficiency increases with zenith angles. On the other hand, the effective area of the instantaneous apertures is proportional to the cosine of the zenith angle. These effects compose the exposures in terms of the observable time and geometrical apertures. The zenith angle dependence is mostly irrelevant for the highest energies.

The differential exposure as a function of declination for 5 years of the POEMMA operations in each of the two different modes is shown in Fig. 11. Purple curves denote the stereo (near-nadir) mode at 50 (dashed) and 100 EeV (solid). Red curves denote the limb-viewing mode at 100 (dashed) and 200 EeV (dash), and 1 ZeV (solid). The exposures of the surface detectors assuming being in

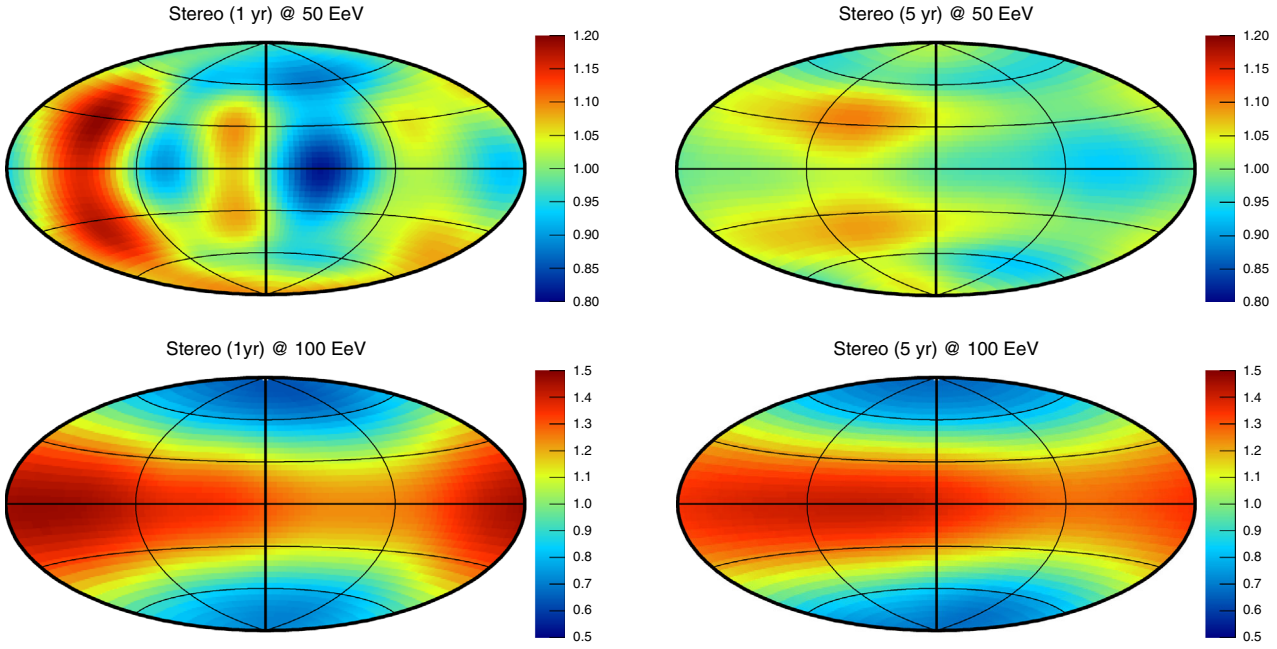

FIG. 12. POEMMA's UHECR sky exposures in declination versus right ascension: The color scale denoting the exposure variations in terms of the mean response taking into account the positions of the sun and the moon during the observation cycle.

operation until 2030 are shown as green and black curves for Auger and TA including the TA × 4 upgrade, respectively. In this figure, the absolute exposures in units of km^2 sr yr have been normalized considering the overall effect of the clouds as studied for JEM-EUSO in Refs. [59,83]. Compared with geographically settled surface detectors, the major advantage of POEMMA is the full sky coverage over the whole celestial sphere with the single experiment that may reduce the systematic uncertainties, e.g., in energy scale, for comparing the different parts of the sky.

In the same references, the climatology of cloud distribution and the fundamental role in the overall exposure have been studied. According to these studies, showers from the large zenith angles develop at higher altitudes and thus, seen from POEMMA, they are more impervious to the presence of clouds. The effects on the exposure map depend upon the event selection cuts applied on the analysis of air showers with respect to the cloud characteristics such as cloud-top height. For the different conditions compared in Fig. 11, different cuts should be optimized according to the science purpose.

In Fig. 12 we show celestial sky coverage maps, where a ∼50% variation is evident in the uniformity of the UHECR sky exposure assuming an isotropic flux. Thus, POEMMA is sensitive to UHECR sources in both the Northern and Southern hemisphere. POEMMA will measure the UHECR source distribution on the full celestial sphere under a single experimental framework with a well-defined UHECR acceptance, mitigating the issues of cross-comparisons inherent to viewing different portions of the sky with multiple experiments. The response shown in each panel of Fig. 12 was calculated assuming that the POEMMA telescopes point in a near-nadir viewing configuration used in stereo mode. The ability of the space-based POEMMA telescopes to tilt towards the Northern or Southern hemisphere allows for the sky exposure to enhance for a specific hemisphere. Likewise, it is easy for POEMMA to change its pointing direction for a sequence of orbital periods to further tailor the UHECR sky coverage.

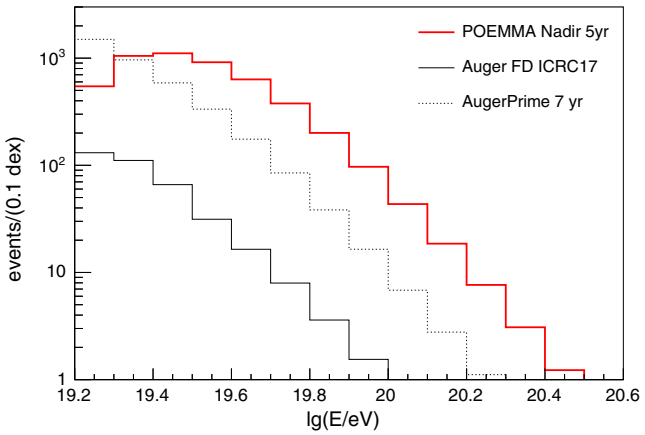

FIG. 13. Number of UHE events with composition information detected by POEMMA for 5 years of data taking in stereo (near-nadir) operational mode (red line). For comparison, the current event statistics collected with the fluorescence detector of the Pierre Auger Observatory is shown as solid black lines and the expected number of events from AugerPrime are indicated by dashed black lines.

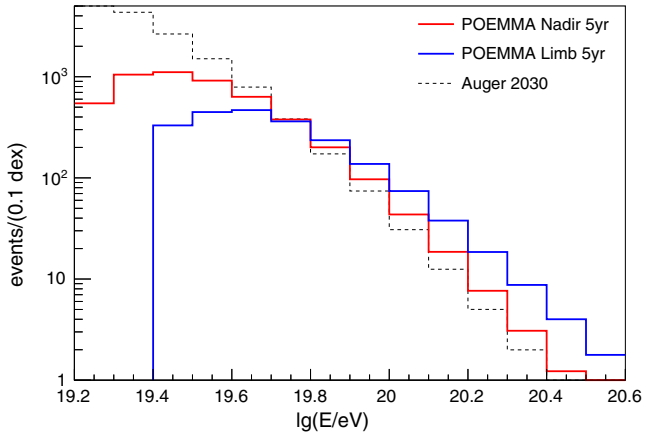

FIG. 14. Number of UHE events detected by POEMMA for 5 years of data taking in stereo (near-nadir) (red line) and limb-viewing (blue line) operational mode assuming the Auger energy spectrum. The expected number of events collected by Auger in case of a continued operation until 2030 is shown as dashed black line.

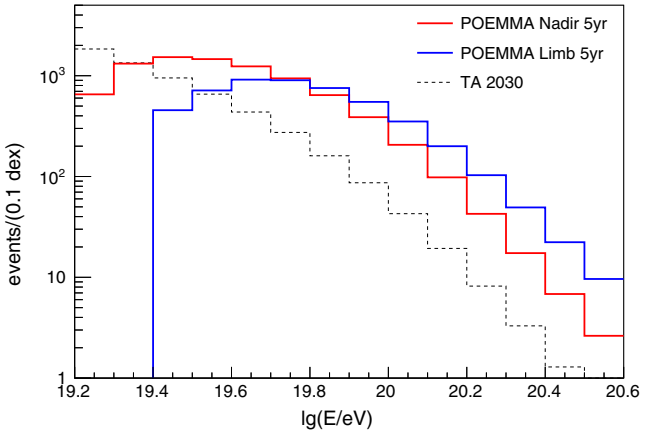

FIG. 15. Number of UHE events detected by POEMMA for 5 years of data taking in stereo (near-nadir) (red line) and limb-viewing (blue line) operational mode assuming the TA energy spectrum. The expected number of events collected by TA (including its upgrade TAx4) in case of a continued operation until 2030 is shown as a dashed black line.

IV. UHECR PERFORMANCE

POEMMA is designed to obtain definitive measurements of the UHECR spectrum, nuclear composition, and source location for $E \gtrsim 20$ EeV. UHECR events are well reconstructed by POEMMA when the two orbiting satellites stereoscopically record the waxing and waning of the EAS fluorescence signal. The video recordings with 1 μs snapshots from each POEMMA satellite define a plane (the observer-EAS plane). The intersection of the two planes from both satellites determines a line in three-dimensional space corresponding to the EAS trajectory. For opening angles between these two planes larger than $\sim 5°$, the reconstruction of the EAS trajectory is robust given POEMMA's excellent pixel angular resolution, yielding superb UHECR angular resolution.

The expected number of events detected during 5 years in stereo and limb-viewing operational mode is shown in Figs. 13–15. To estimate the event rate in these figures we assumed that the UHE flux follows the fit of the Auger combined spectrum given in [7] (Figs. 13 and 14) and the one from TA given in [84] (Fig. 15). The comparison of the events in stereo mode with the current statistics of the Auger FD shows that POEMMA will be a giant leap forward regarding the detection of cosmic rays with the fluorescence technique. POEMMA will increase the number of UHE cosmic-ray events with direct observation of $X_{\max}$ and energy from 62 (last integral bin of the Auger FD analysis above 30 EeV) to more than 2000.[2]

[2]Indirect estimates of $X_{\max}$ with the surface detector of Auger were reported in [22] with 517 events above $10^{19.5}$ eV and a resolution of 45 g/cm^2. The AugerPrime detector could detect about 700 events above this energy within 7 years of running time and a resolution of about 30 g/cm^2 [57].

The integral number of events will be a factor of 1.5 larger than the one used by Auger to study correlations with starburst galaxies above 40 EeV and 2.1 larger than the one for γAGN above 60 EeV [35]. Moreover, contrary to the Auger data set, the POEMMA exposure covers the full sky and each event detected by POEMMA in stereo mode will have a measurement of the shower maximum and thus allow to study the correlations for different cosmic-ray rigidities.

The UHECR aperture in limb-viewing mode starts to outperform the stereo operation above 60 EeV. However, due to the steeply falling cosmic-ray flux above the suppression, the expected number of events beyond the crossover is of the same order of magnitude (75 for stereo and 146 for limb viewing assuming the Auger spectrum). Given that stereo events have a better energy resolution and provide information about the shower maximum, we foresee that most of the UHECR data-taking time will be spent in stereo (near-nadir) mode. The collected exposures at 40 at 100 EeV after 5 years of operation are shown in Fig. 16.

An estimate of the $X_{\max}$ resolution of POEMMA in stereo mode is shown in Fig. 17. The contribution from the PE statistics was studied with a full simulation in Sec. III and amounts to about 20 g/cm^2 at 30 EeV for one photometer and decreases approximately with $\sqrt{E}$ (see Fig. 8). The uncertainty in the measured zenith angle of the shower affects the calculation of the slant depth of the shower maximum. A preliminary analytic propagation of this uncertainty to the resolution of $X_{\max}$ is indicated as gray lines in Fig. 17 averaged over the expected arrival directions of triggered events. Since inclined events are more affected than vertical ones, the overall resolution depends on the maximum zenith angle of the data sample

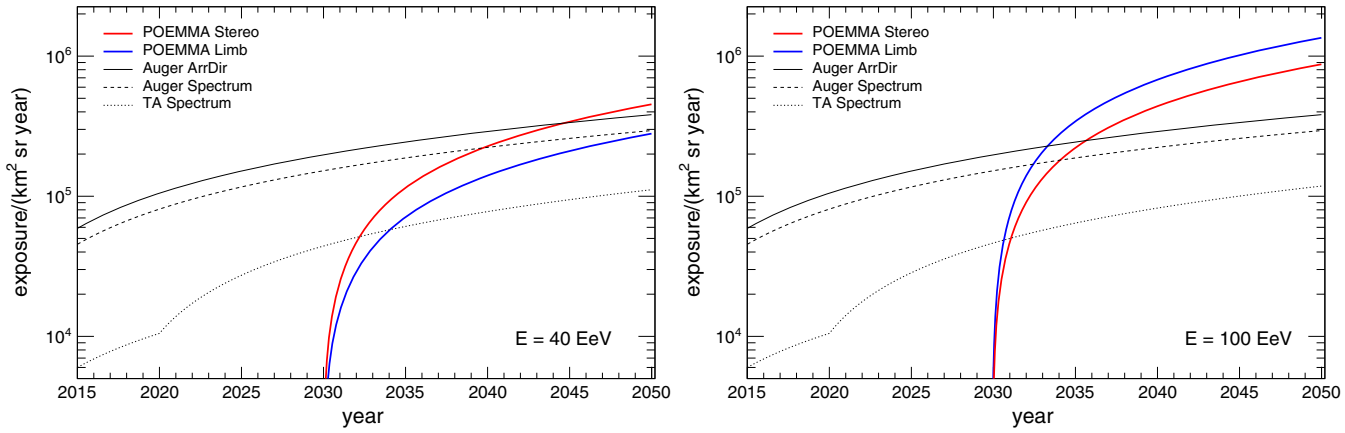

FIG. 16. Exposure as a function of time collected by Auger, TA (including TAx4) and POEMMA. For Auger the exposure for two different event selections is shown. The left panel shows the exposures at 40 EeV and the right panel at 100 EeV.

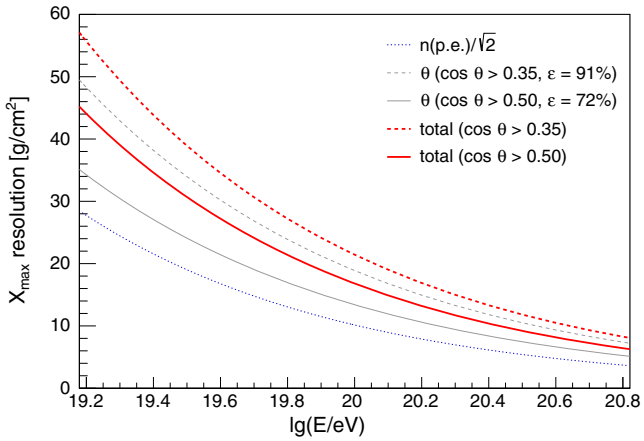

FIG. 17. Preliminary estimate of the $X_{\max}$ resolution of POEMMA in stereo mode. The contributions from the photoelectron statistics and angular resolution are shown in blue and gray, respectively. The total resolution, obtained by adding both contributions in quadrature, is shown in red for two cuts on the maximum zenith angle.

(a possible correlation between the zenith angle and angular resolution has not been taken into account yet). The total $X_{\max}$ resolution of POEMMA, including both angular resolution and PE statistics, is about 31 g/cm^2 at 30 EeV for events below 60° (72% of the data sample) and 39 g/cm^2 below 70° (91% of the data sample). At 100 EeV the resolution is 17 and 21 g/cm^2, respectively.

V. SCIENCE REACH

The typical observables for comparing data to model predictions are the energy spectrum, the mass spectrum, and the distribution of arrival directions of UHECR reaching the Earth. From these observables, the last one provides the most unambiguous conclusions about the locations of the sources. In this section, we determine the sensitivity of POEMMA to measure the first two observables and discuss the discovery reach of anisotropy searches using the third observable. We also investigate supplementary science capabilities of POEMMA. We first determine the sensitivity to probe particle interactions at extreme energies and after that we explore the potential for observing extreme energy photons produced in the decay of superheavy dark matter (DM) particles clustered in the halo of the Milky Way. We then present the UHE neutrino sensitivity based on stereo fluorescence measurements of neutrinos interacting deep in the atmosphere.

A. Energy spectrum

The all-particle spectrum contains information about the source distribution, emission properties, nuclear composition, and propagation effects. Indeed, there is a fair amount of work devoted to deducing such fundamental information from details of spectral features. The standard approach involves establishing some hypothesis about source properties and, using either Monte Carlo simulations or analytic methods, inferring the mean spectrum one expects to observe here on Earth. Since at present we have a limited understanding of source distributions and properties, it is common practice to assume spatially homogeneous and isotropic UHECR emissions, and compute a mean spectrum based on this assumption. Obviously, in the real world this assumption cannot be correct, especially at the highest energies where GZK interactions severely limits the number of sources visible to us at Earth. However, one can quantify the possible deviation from the mean prediction based on the understanding we do have on the source density and the possible distance to the closest source populations. Such a subsequent statistical moment beyond the mean prediction is referred to as the *ensemble fluctuation* [85]. It depends on, and consequently provides information on, the distribution of discrete local sources, source nuclear composition, and energy losses during propagation. The ensemble fluctuation in the energy spectrum is one manifestation of the cosmic variance,

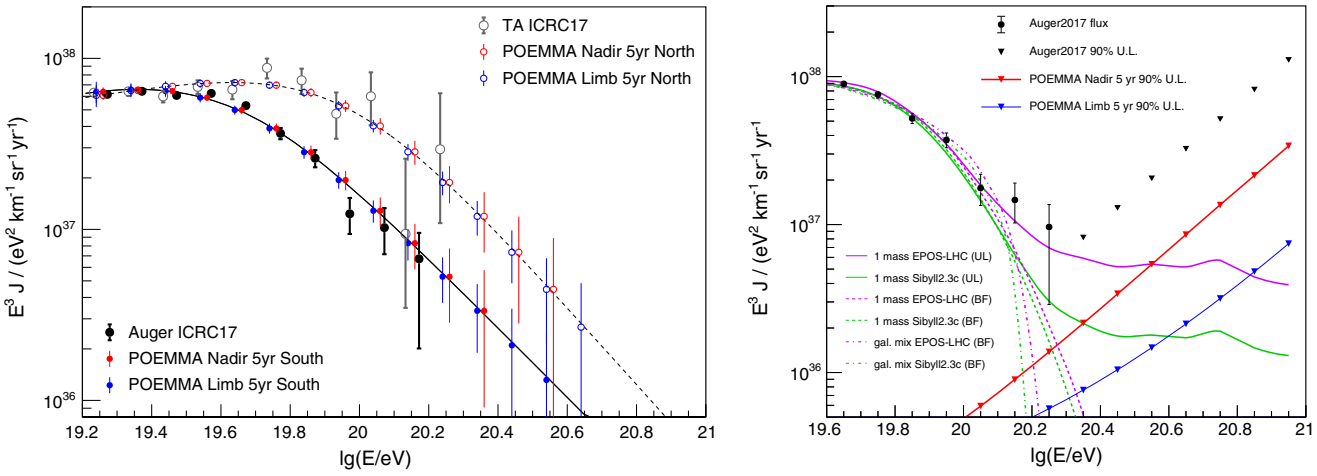

FIG. 18. Left: Energy spectrum of UHECRs as measured by TA and Auger in the Northern and Southern hemisphere, respectively. The energy scale of the two experiments were cross-calibrated by ±5.2% as derived by the UHECR Spectrum Working Group at low energies. Red and blue dots with error bars illustrate the expected accuracy reached with POEMMA in stereo and limb-viewing mode within 5 years of operation. Right: Flux suppression at UHE as measured by the Pierre Auger Observatory (data points) [7]. Ninety percent confidence upper limits of the flux at UHE are shown as downward triangles (ideal limits without taking into account event migration due to the limited energy resolution of the observatories). Black, Pierre Auger Observatory 2017; red, POEMMA 5 year stereo mode; blue, POEMMA 5-year limb-viewing mode. Various model predictions for the shape of the flux suppression from [86] are superimposed as black lines.

which should also come out directly via eventual identification of nearby source populations.

POEMMA will have full-sky coverage for UHECRs due to the nature of the 525 km, 28.5° inclination orbit and large 45° full FoV for each telescope. Therefore, the satellites will observe the source distribution on the full celestial sphere under a single experimental framework with a well-defined acceptance. This implies that POEMMA will be sensitive to ensemble fluctuations in the energy spectrum for two "realizations of the Universe." For example, it will be able to detect spectral variations in the northern and southern skies, or else distinct ensemble fluctuations associated with the spatial anisotropy of the dipolar asymmetry observed by Auger [32]. In the left panel of Fig. 18 we show the UHECR spectrum as observed by Auger and TA together with the expected accuracy reached with POEMMA in stereo and limb-viewing mode after 5 years of data collection, assuming normalization to each of the experiments. As can be seen, the high-statistics sample with high resolution to be collected by POEMMA will provide a final verdict on whether the Auger and TA discrepancy in the measurement of the spectrum at the highest energies is due to physics, statistics, or systematic uncertainties in the energy calibration.

The abrupt softening of the spectrum due to energy losses via photopion production and/or photodisintegration in the CMB (also known as GZK cutoff) is the only unequivocal prediction ever made concerning the spectral shape [30,31]. The discovery of a suppression at the end of the spectrum was first reported by HiRes [10] and Auger [11], and later confirmed by TA [13]; by now the significance in Auger data is well in excess of 20σ compared to a continuous power law extrapolation beyond the ankle feature [12]. Although the existence of the flux suppression has been firmly established, an alternative interpretation for the suppression region was put forward in [87], wherein it is postulated that the end-of-steam for cosmic accelerators is coincidentally near the putative GZK cutoff. Note that this alternative interpretation predicts an increasingly heavier composition from the ankle towards the suppression region, with a mix of protons and heavies undergoing acceleration to the same rigidity, so that their maximum energy scales as $E_Z^{\max} \sim ZE_p^{\max}$, where $E_p^{\max}$ is the maximum proton energy. Yet another model to explain the suppression postulates that the maximum energy is constrained by GZK interactions at the source [46]. This model also yields a change towards a heavier composition at higher energies, but predicts a different scaling for the maximum energy because while the acceleration capability of the sources grows linearly in Z, the energy loss per distance traveled decreases with increasing A. A general feature of the GZK cutoff is that of a slight recovery of the spectrum if the source emission spectra extend to energies far beyond 100 EeV. This is in sharp contrast to models that postulate that the suppression is primarily caused by the limiting acceleration energy at the sources, which makes the observed spectrum steeper than that at lower energy, developing a sharp cutoff.

In the right panel of Fig. 18 we show the sensitivity of POEMMA to observe the GZK recovery. The sensitivity is given by the 90% confidence level upper limit for the case of zero observation with zero background [88].

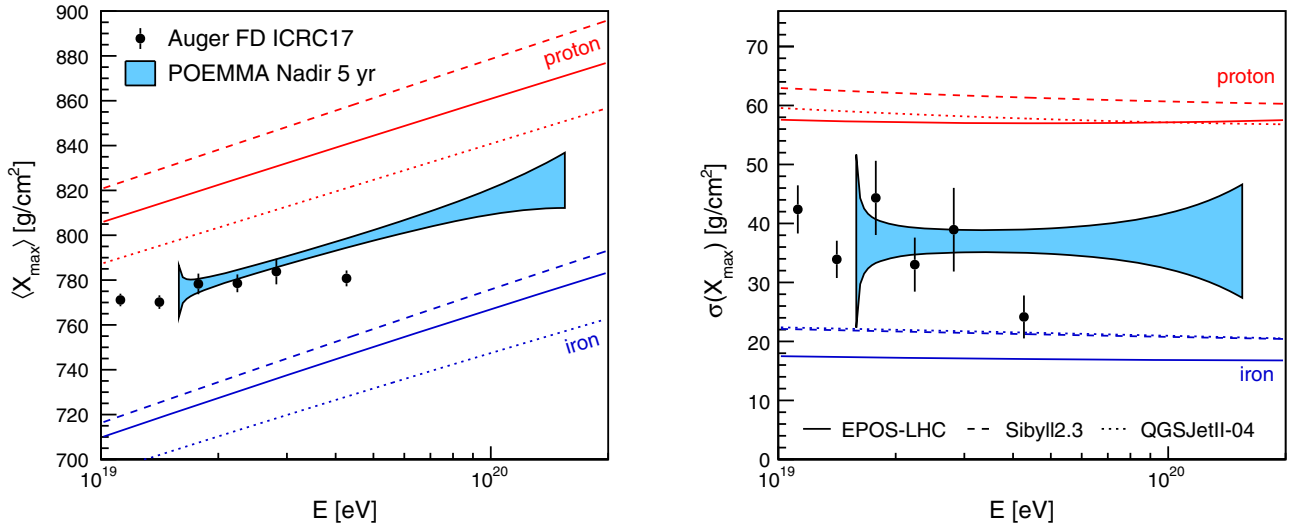

FIG. 19. Capability of POEMMA to measure $\langle X_{\max}\rangle$ and $\sigma(X_{\max})$ for composition studies at UHE. The width of the blue band illustrates the expected statistical uncertainties given the number of events per 0.1 in logarithm of energy in 5-year stereo operation, the $X_{\max}$ resolution and efficiency from Fig. 17 for $\theta < 70°$, and intrinsic shower-to-shower fluctuations of 40 g/cm^2. The band spans the energy range for which more than ten events are within a 0.1 dex bin.

Therefore, these sensitivities are for the ideal case of perfect energy resolution and the actual sensitivity will be somewhat worse due to the nonzero probability of a net migration of events from lower energies towards the low-flux UHE energy range. It should be noted that if a post-GZK recovery is observed in stereo mode, the POEMMA instruments could tilt to increase the sensitivity for the highest energy UHECRs.

The ideal POEMMA sensitivity is compared to generic model predictions of the spectral falloff [86] built on the UFA15 [89] model that explains the shape of the spectrum and its complex composition evolution via photodisintegration of accelerated nuclei in the photon field surrounding the source, but also allowing for a subdominant purely protonic component that is constrained by UHECR composition measurements [20], limits on astrophysical neutrinos (IceCube [90] and ANITA [91]) and gamma-ray observations (Fermi-LAT [92]).

B. Nuclear composition

The measurement of the composition of UHECRs is one of the key ingredients to constrain their origin. The event-by-event measurement of energy and $X_{\max}$ with fluorescence telescopes is well suited to perform composition studies [93]. As can be seen in Fig. 19, the high statistics and good energy and $X_{\max}$ resolution of POEMMA will allow for high-precision composition studies at hitherto unexplored energies, while at the same time providing an overlap with existing compositions measurements from Auger at low energies.

EASs initiated by photons have a larger $X_{\max}$ than showers initiated by nuclei with the same energy. This is because the radiation length is more than 2 orders of magnitude shorter than the mean-free path for photonuclear interaction, and therefore this leads to a reduced transfer of energy to the hadronic component of the EAS [94]. The development of EAS initiated by a photon is hence delayed (compared to a baryon-induced shower) by the typically small multiplicity of electromagnetic interactions. On the other hand, for showers of a given total energy E, heavy nuclei have smaller $X_{\max}$ than light nuclei because they have a larger cross section and interact sooner, and because the energy is already shared among A nucleons, so the shower develops more quickly. More concretely, $\langle X_{\max}\rangle$ scales approximately as $\ln(E/A)$ [15,16]. In addition, the standard deviation $\sigma(X_{\max})$ is smaller for heavier nuclei because the subshower fluctuations average out. By contrast, protons or He can have a deep or shallow first interaction, and the shower-to-shower fluctuations in subsequent development are larger. Therefore, only light cosmic rays have large $X_{\max}$, permitting a fraction of events to be unambiguously identified as light nuclei. The high event statistics with good $X_{\max}$ resolution would allow POEMMA not only to isolate baryons from photon and neutrino primaries, but also to distinguish between protons, light nuclei, medium mass nuclei, and heavies [95].

In addition, if a hot spot of a nearby source is identified, protons can be further discriminated from CNO and heavies by looking at the distribution of arrival directions. This is because while sources of UHECR protons exhibit anisotropy patterns that become denser and compressed with rising energy, nucleus-emitting sources imprint layers on the sky that become more distant from the source position with rising energy [96]. The peculiar shape of the hot spots from nucleus accelerators is steered by the

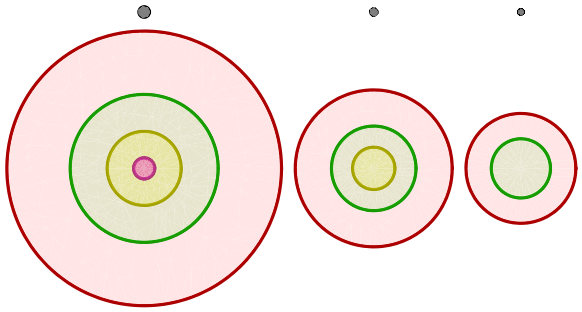

FIG. 20. Circles representing the composition-layered structure of hot spots at different energies, for proton sources (top) and nuclei sources (bottom). The radii of the circles respect the proportions of the angular sizes given by (2), for protons (black), helium (magenta), nitrogen (yellow), silicon (green), and iron (red), as well as for 40 (left), 70, (center) and 100 EeV (right).

competition between energy loss during propagation and deflection on the Galactic magnetic field: for a nucleus of charge Ze and baryon number A, the bending of the cosmic ray decreases as Z/E with rising energy, while the energy loss per distance traveled decreases with increasing A. The potential for nucleus-proton discrimination is shown schematically in Fig. 20, and can be understood as follows. If the source emits only protons, the size of the corresponding "spot" should decrease as $1/E$ with rising energy due to reduced deflection in magnetic fields. In contrast, if the source produces a mixed composition, a different quality emerges. Lighter compositions tend to shorter mean-free paths at higher energies, so as their energy increases they begin to disappear from the sample leaving behind only the lower energy component. The latter suffers a relatively smaller magnetic deflection compared to heavier nuclei at all energies. One thus ends up with a hot spot in which the energies of the species observed closer to the source have a lower rather than higher energy, as they would in the case that the source emitted only protons.

Despite the fact the Galactic magnetic field is highly anisotropic, to anticipate the sensitivity of POEMMA herein we assume that the deflection of particles is isotropic around the line of sight, and given by (2). We further assume that the fixed parameters of the statistical analysis should match the anisotropy clues provided by Auger data. Hence, we adopt a search angular window $\Delta = 13°$, a source distance ~4 Mpc, a threshold energy $E_0 = 39$ EeV, and source spectrum $\propto E^{-5.03}$ that are consistent with both the energy spectrum above 40 EeV reported by the Auger Collaboration [7] and the source spectra of nearby starburst galaxies as estimated in [97]. With this simplified picture in mind, we assume that UHECRs are *normally* distributed around the source direction, which defines the center of the hot spot. The deflection δ, which characterizes the angle between the arrival direction and the line of sight, is a random variable distributed according to a one-sided von Mises distribution, bounded by a window size Δ with zero mean and a dispersion parameter $\kappa = 1/\theta^2(E, Z)$. The probability density for an UHECR to have energy in $[E, E + dE]$ and deflection in $[\delta, \delta + d\delta]$ is found to be

$$f(E, \delta|A, Z) = \mathcal{A}E^{-5.03} \exp\left[-\frac{E}{E_A}\right]\Theta(E - E_0) \times \exp\left[\frac{\cos\delta}{\theta^2(E, Z)}\right]\Theta(\Delta - \delta), \quad (3)$$

where $\mathcal{A}$ is a normalization constant and E_A is the cutoff energy in the observed spectrum of the various species. Following [97] we take $E_4 = 60$ EeV, $E_{14} = 80$ EeV, $E_{28} = 130$ EeV, and $E_{56} = 210$ EeV, which accounts for energy losses during propagation. Before proceeding, we pause to note that in the actual data analysis one should also consider the variations of the magnetic field for UHECRs arriving from different points of the sky. A full consideration of the anisotropic magnetic deflections would require an adjustment of the distribution in (3) to incorporate an azimuthal variable around the line of sight, and should also take into account the source direction in the sky. Notwithstanding, our assumption of isotropy around the line of sight provides a demonstration of the search procedure while keeping the complexity at a reasonable level at this stage.

To carry out the statistical analysis we adopt the Kolmogorov-Smirnov test. The power of a statistical test is the probability that the null hypothesis is rejected if it is actually false. The probability of rejecting the null hypothesis, while it is true, depends on the significance level of the test α. For a chosen null hypothesis $\mathcal{H}_0$ and significance level α, there is a critical value for the test statistic, t_c, above which there is a fraction α of the data simulated following $\mathcal{H}_0$. For a given alternative hypothesis $\mathcal{H}_k$, the fraction β_k of the data with test statistic $t < t_c$ is the probability of not rejecting the null hypothesis while it is false. All in all, the power of the test for a given $\mathcal{H}_k$ is $\mathcal{P}_k = 1 - \beta_k$.

We simulate data sets $\mathcal{D}_{x,N}$ following the distributions in (3), where $x \in \{p, {}^4\mathrm{He}, {}^{14}\mathrm{N}, {}^{56}\mathrm{Fe}\}$ and $N = \dim \mathcal{D}_{x,N}$ is the number of data points in the hot spot. For each value of N, which roughly corresponds to a given live time of the POEMMA mission, we consider as a null hypothesis a pure proton composition, $\mathcal{H}_{\mathrm{p},N}$, and the different nuclei as alternative hypotheses $\mathcal{H}_{\mathrm{x},N}$. To estimate the performance of POEMMA we take an event rate above E_0 of $\Gamma \sim 280\ \mathrm{yr}^{-1}$. A 13° angular radius solid angle covers a fraction $f_{\mathrm{sky}} \sim 0.013$ of the sky. Within a hot spot, one expects both background and source contributions, with a ratio $f_{\mathrm{events}} = n_{\mathrm{ev}}/n_{\mathrm{bg}}$. With this, the required live time of the experiment to measure a hot spot of N events can be roughly estimated to be

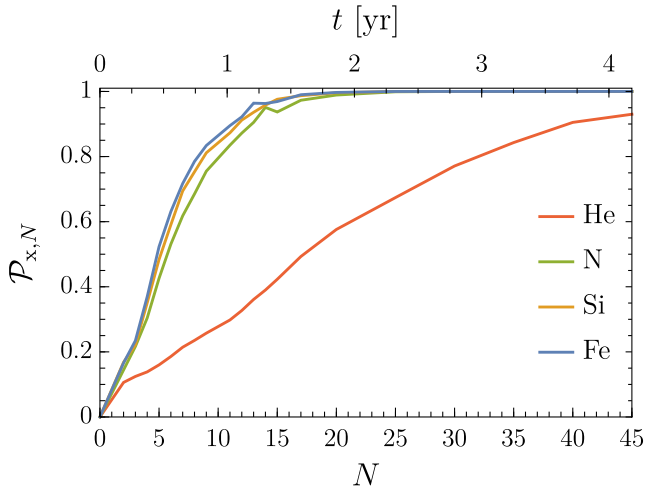

FIG. 21. Power of the statistical test for different alternative hypotheses, that is, different nuclei and number of events per hot spot. The horizontal axis on the top indicates the projected timescale for POEMMA.

$$T \sim \frac{N}{\Gamma f_{\rm sky} f_{\rm events}}. \tag{4}$$

For $f_{\rm events} \sim 3$, as observed in [7] from the direction of the nearby radiogalaxy Centaurus A, $T \sim 0.09N$ yr. The projected sensitivity of POEMMA is shown in Fig. 21. For hot spots of 20 or more events, the discovery power (with $\alpha = 0.05$) is almost 1 for nuclei other than helium. Therefore, we conclude that if the hot spot is composed of nuclei heavier than nitrogen, in 2 years of operation POEMMA will be able to exclude a pure proton origin at the 95% C.L.

C. Anisotropy searches

1. Large-scale anisotropy searches using spherical harmonics

The most direct way to determine the location of the sources is to search for anisotropy in the distribution of arrival directions. The distribution of arrival directions, like any field on the unit sphere, can be conveniently decomposed in spherical harmonics [98]. Specifically, we can decompose the angular distribution of events Φ in some direction $\hat{n}$ by separating the dominant monopole contribution from the anisotropic one, $\Delta(\hat{n})$, according to

$$\Phi(\hat{n}) = \frac{N}{4\pi f_1} W(\hat{n})[1 + \Delta(\hat{n})], \tag{5}$$

where $W(\hat{n})$ is the relative coverage of the experiment varying from 0 to 1, $f_1 = \int d\hat{n} W(\hat{n})/(4\pi)$ is the fraction of the sky effectively covered by POEMMA, and N is the total number of observed UHECRs [99,100].

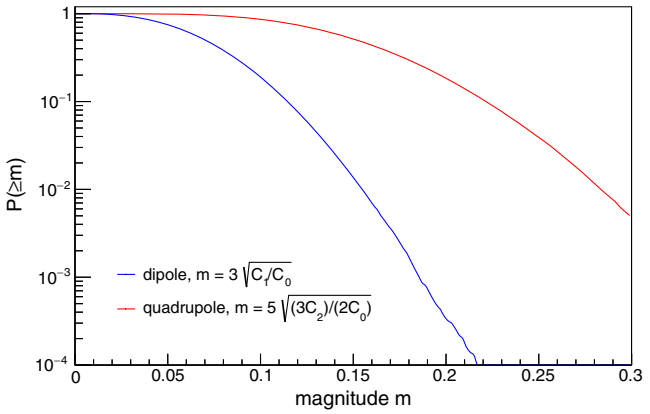

FIG. 22. Cumulative distributions for the dipole and quadrupole moments for isotropically distributed skies with $N = 1400$ events.

Along these lines, the multipolar expansion of $\Delta(\hat{n})$ into the spherical harmonics basis $Y_{\ell m}(\hat{n})$ is given by

$$\Delta(\hat{n}) = \sum_{\ell=1}^{\infty} \sum_{m=-\ell}^{\ell} a_{\ell m} Y_{\ell m}(\hat{n}), \tag{6}$$

where the $a_{\ell m}$ coefficients encode any anisotropy signal. An unambiguous measurement of the full set of spherical harmonic coefficients requires full-sky coverage. Indeed, using the orthogonality of the spherical harmonics basis one can directly recover the multipolar moments $a_{\ell m}$. The partial-sky coverage of ground-based experiments, encoded in the $W(\hat{n})$ function, prevents direct determination of the $a_{\ell m}$ coefficients. Although the exhaustive information of the distribution of arrival directions is encoded in the full set of multipole coefficients, the characterization of any important overall property of the anisotropy becomes evident in the angular power spectrum

$$C(\ell) = \frac{1}{2\ell + 1} \sum_{m=-\ell}^{\ell} a_{\ell m}^2, \tag{7}$$

which is a coordinate independent quantity. Any significant anisotropy of the angular distribution over scales $\simeq 1/\ell$ radians would be captured in a nonzero power in the mode ℓ. For a 5-year mission with $N = 1400$ events, we have $\langle C(\ell) \rangle = (4\pi N)^{-1} \simeq 6 \times 10^{-5}$ [101].

In order to assess the sensitivity of POEMMA to dipolar and quadrupolar anisotropy patterns, we consider the distribution of dipole and quadrupole moment magnitudes for an isotropic 1400 event sky, as shown in Fig. 22. From this distribution, it is straightforward to estimate that with POEMMA, dipole (quadrupole) moments above ~11% (~21%) and ~18.5% (~33%) can be probed at the 84% and 99.9% confidence level sensitivities at 40 EeV.

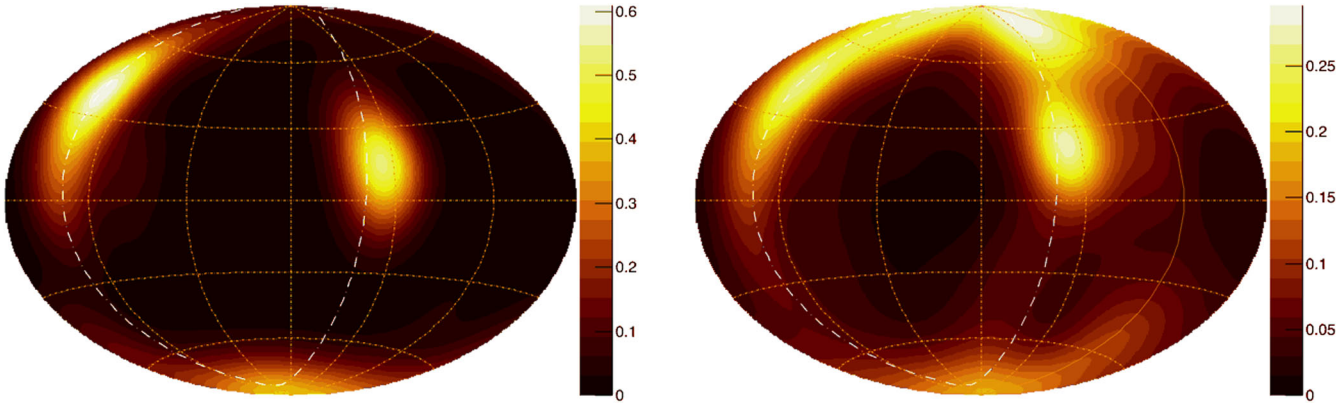

FIG. 23. Left: Skymap of nearby starburst galaxies from Refs. [35,103] weighted by radio flux at 1.4 GHz, the attenuation factor accounting for energy losses incurred by UHECRs through propagation, and the exposure of POEMMA. The map has been smoothed using a von Miser-Fisher distribution with concentration parameter corresponding to a search radius of 15.0° as found in Ref. [35]. The color scale indicates $\mathcal{F}_{\rm src}$, the probability density of the source sky map, as a function of position on the sky. The white dot-dashed line indicates the supergalactic plane. Right: Same as at left for nearby galaxies from the 2MRS catalog [105] and weighting by K-band flux corrected for Galactic extinction.

2. *Intermediate-scale anisotropy searches through cross-correlations with astrophysical catalogs*

One commonly invoked test for anisotropy on intermediate scales is motivated by the expectation that UHECRs will point back to their sources above a given threshold energy. The exact value of the threshold energy is unknown due to uncertainties in the Galactic and extragalactic magnetic fields. However, the expectation is that the threshold energy occurs at roughly the same energies at which the flux of UHECRs is attenuated by cosmological photon backgrounds. UHECR attenuation results in a horizon distance for UHECRs within which astrophysical sources appear to be anisotropic; hence, the expectation is that above a given energy threshold, the arrival directions of UHECRs will be similarly anisotropic and will be, to a given degree, correlated with the positions of their sources on the sky, with angular separations corresponding to the degree of magnetic deflection (angular separations ∼ few tens of degrees). As such, statistical tests cross-correlating arrival directions of UHECR events with astrophysical catalogs are effective in detecting anisotropy at intermediate scales and may also provide clues about the UHECR source population(s) and the amount of deflection due to intervening magnetic fields [102]. Previous searches conducted by the Auger and TA collaborations utilizing this approach have provided hints of anisotropy [34,35], with the strongest signal arising from cross-correlation with a catalog of starburst galaxies (significance $\sim 4.5\sigma$ [103]).

As can be seen in Fig. 16, POEMMA will attain an exposure of $\sim 1.5 \times 10^5$ km^2 sr year above 40 EeV within 5 years of operation. Furthermore, the POEMMA exposure will cover the entire sky, providing sensitivity to starburst galaxies that are not accessible to Auger or TA. As such, within its nominal mission lifetime, POEMMA will be capable of detecting anisotropy to high significances, achieving 5σ discovery reach for search parameters within the vicinity of the signal regions for anisotropy hints reported by the Auger [35,103] and TA [34] collaborations. In order to determine the reach of POEMMA in such cross-correlation searches, we implement a simple statistical study simulating POEMMA data sets assuming various astrophysical scenarios (i.e., starbursts and AGNs). Mock data sets are constructed by drawing a given fraction of events, $f_{\rm sig}$, from an astrophysical source sky map and drawing the rest $(1 - f_{\rm sig})$ from an isotropic sky map, where both sky maps are weighted by the variation in POEMMA exposure over the sky (see Fig. 11). We construct the astrophysical source sky maps from catalogs of candidate UHECR sources, weighting each individual source by its electromagnetic flux, accounting for UHECR attenuation due to energy losses during propagation, and smoothing with a von Mises-Fisher distribution with a given angular spread, Θ (see examples in Fig. 23). For the purposes of this study, we use the same astrophysical catalogs as in Refs. [35,103], which include a catalog of starburst galaxies selected based on their continuum emission at 1.4 GHz, a catalog of radio-loud and radio-quiet AGNs included in the 70 Month *Swift*-BAT All-sky Hard X-ray Survey [104], and a catalog of galaxies at distances greater than 1 Mpc from the 2MASS Redshift Survey (2MRS) of nearby galaxies [105]. For calculating the UHECR attenuation factors, we adopted composition scenario A from Ref. [35], which best matches Auger composition and spectral measurements. For the threshold energy values, we adopted the values found in Ref. [103], which corresponds to roughly 1400 events with 5 years of POEMMA, assuming the Auger cosmic-ray spectrum. We construct mock data sets several scenarios for each catalog, varying the signal fraction of events, $f_{\rm sig}$, and the angular spread, Θ. For each mock data set, we perform a statistical

TABLE II. TS values for scenarios with $\Theta = 15°$.

Catalog	$f_{\rm sig}$	TS	σ
SBG	5%	6.2	2.0
	10%	24.7	4.6
	15%	54.2	7.1
	20%	92.9	9.4
2MRS	5%	2.4	1.0
	10%	8.7	2.5
	15%	20.0	4.1
	20%	35.2	5.6
Swift-BAT AGN	5%	10.4	2.8
	10%	39.6	6.0
	15%	82.4	8.8
	20%	139.3	11.6

analysis testing the astrophysical hypothesis against the null hypothesis of isotropy. In so doing, we follow the likelihood ratio approach of Abbasi *et al.* [[36]; see also [3,35,106]], constructing profiles of the test statistic (TS) as a function of $f_{\rm sig}$ and Θ and finding the maximum TS value. Since TS values vary over realizations of the mock data sets, we simulate 1000 data sets for each scenario and compute the average TS value at particular values of $f_{\rm sig}$ and Θ in order to construct the TS profiles. Motivated by reported search radii of $\sim 15°$ found in Ref. [103], we present results for selected scenarios in which $\Theta = 15°$ in Table II and Fig. 24. See Appendix B for more details on the maximum-likelihood methodology and a more complete table of results for all scenarios considered in this study.

It is worth noting that though many of the scenarios included in this study are very similar to the maximumlikelihood search parameters obtained by the Auger collaboration [103], the maximum TS values obtained from our simulations may be somewhat different than expected based on the maximum TS values obtained Auger. This is likely due to the fact that certain catalogs contain powerful sources in regions of the sky that are not accessible by Auger. The impact is that in simulations in which we assume the same signal fraction as found by Auger, the signal events are now distributed over more sources, spreading out the anisotropic events over a wider portion of the sky and making each individual source less significant. The result is that the TS values obtained from the simulations may be somewhat lower than expected, perhaps even lower than Auger found. This is most noticeable in the starburst scenario with simulation parameters $f_{\rm sig} = 10\%$ and $\Theta = 15°$. The Auger exposure map does not include M82, a nearby powerful starburst galaxy, that would be included in our simulations. The result is that the TS value predicted by the simulations (24.7; significance $\sim 4.6\sigma$) is somewhat lower than the TS value reported by Auger (29.5; post-trial significance $\sim 4.5\sigma$). However, if starbursts are the sources of UHECRs, we would expect that adding a powerful source like M82 would increase the fraction of events that would correlate with starburst galaxies. As such, we also present scenarios in which the signal fraction is higher, and in these scenarios, we see that POEMMA will detect the signal to very high significances.

D. Fundamental physics

In this section we explore the potential of the POEMMA mission to probe fundamental physics. We begin with a discussion of measurements of the pp cross section beyond collider energies. After that, we study the sensitivity of POEMMA for two typical messengers of top-down models: photons and neutrinos.

1. Inelastic proton-air and proton-proton cross sections

The showers absorbed in the atmosphere observed by POEMMA correspond to a calorimetric fixed target experiment with $E_0 > 40$ EeV. The collisions of the primary

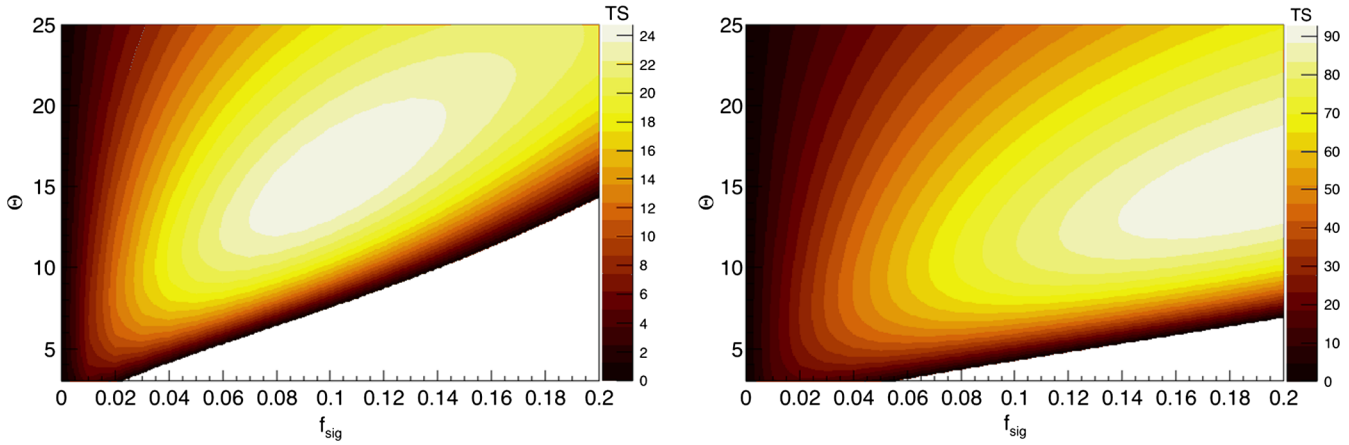

FIG. 24. TS profile for 1400 events for a particular scenario using the starburst source sky map in Fig. 23. In the scenario pictured here, the fraction of events drawn from the source sky map is $f = 10\%$ (left) and 20% (right), and the angular spread is $\Theta = 15°$.

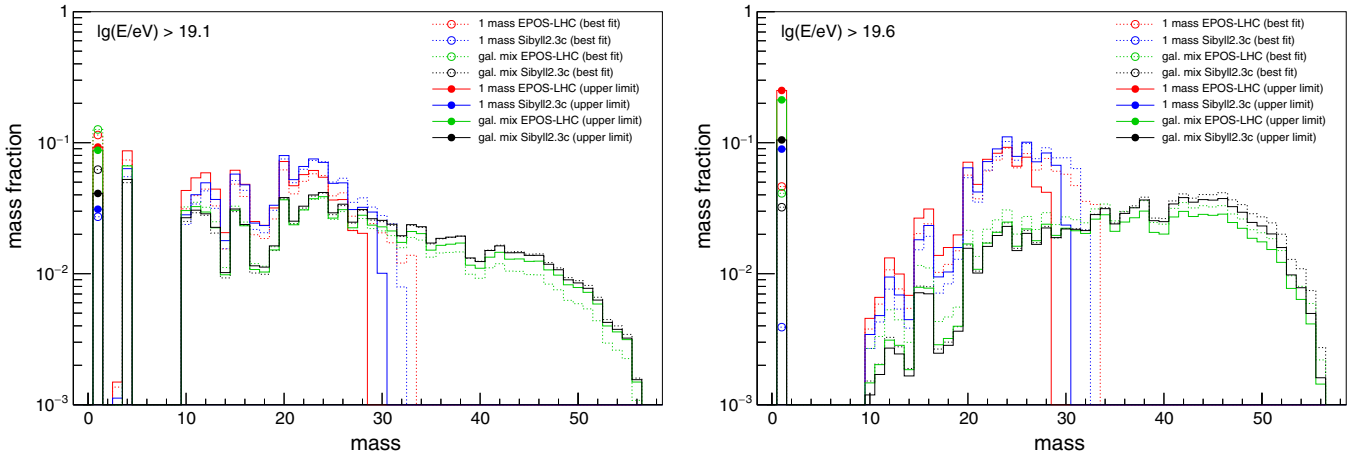

FIG. 25. Composition scenarios with UHE protons from [86] at $10^{19.1}$ (left) and $10^{19.6}$ eV (right). There is no helium left above 40 EeV and the mass distribution is broad with a peak at around $A \sim 40$.

cosmic-ray particles with atoms of the atmosphere happen at equivalent center-of-mass energies per nucleon-nucleon pair of above $\sqrt{s_{NN}} = \sqrt{2E_0 m_p} = 283$ TeV. When those numbers are put into perspective with the capabilities of the LHC, where the beam energy is limited to 7 TeV and the maximum center-of-mass energy to 14 TeV, it is clear that there is an exciting opportunity to study fundamental particle physics at extreme energies. In this section we estimate the potential of POEMMA to measure the elemental inelastic cross sections at center-of-mass energies above 283 TeV. For this purpose we follow here the analysis procedure developed by the Pierre Auger Collaboration [107], where the exponential slope of the high-$X_{\rm max}$ tail is measured and related to the proton-air cross section $\sigma_{p\text{-air}}$. The exponential slope Λ_η is defined via

$$\frac{dN}{dX_{\rm max}} \propto \exp(-X_{\rm max}/\Lambda_\eta) \tag{8}$$

for all $X_{\rm max}$ values above a minimum grammage $X_{\rm max} > X_{\rm max}^{\rm start}$. The slope Λ_η is inversely proportional to the proton-air cross section via

$$\sigma_{p\text{-air}} = \frac{\langle m_{\rm air}\rangle}{k\Lambda_\eta}, \tag{9}$$

with $\lambda_{p\text{-air}} = k\Lambda_\eta$ being the interaction length of protons in the air, and $\langle m_{\rm air}\rangle$ is the mean target mass of air. Using the measurement of Λ_η automatically enriches the proton contribution in a mixed mass scenario since protons are the most deeply penetrating cosmic-ray nuclei. Thus, this approach is well suited for a first demonstration of the POEMMA capability.

The choice of $X_{\rm max}^{\rm start}$ is critical and determines the statistical power of the analysis as well as the systematic effects of model or mass dependence. The value of $X_{\rm max}^{\rm start}$ can be defined via the fraction η of the most deeply penetrating events. It was shown that $\eta = 0.2$ yields optimal results in the case of the Pierre Auger Observatory for events with an average energy of $\sqrt{s_{NN}} = 57$ TeV and an assumed maximum helium contamination of 25% [107]. In the following, we investigate estimates of η at higher energies for POEMMA, informed by the p-air cross section analysis of the Pierre Auger Collaboration.

In general, the distribution $dN/dX_{\rm max}$ depends to a large extent on the cosmic-ray mass composition. We adopt as benchmark composition models the recent fits to Auger data from [86] shown in Fig. 25. As can be seen, there is no helium in these models above 40 EeV. Indeed there is almost no helium production at sources, and the small attenuation length of ^{4}He on the CMB [108] further suppresses the flux on Earth. Inspired by these models we investigated two simple scenarios as potential limiting cases of the mass composition at Earth above 40 EeV: an optimistic one with a flux composition ratio of p:Si = 1:3 and a conservative one with p:N = 1:9. Obviously, a larger proton fraction directly leads to a better statistical precision and a better handle to limit systematic uncertainties. Heavier nuclei contribute less to the high $X_{\rm max}$ tail than lighter nuclei do, so nitrogen contributes more to the $X_{\rm max}$ tail than silicon, even with equal composition ratios. Thus, 90% nitrogen corresponds to the most conservative assumption studied here. The more realistic mass distributions (for the galactic mixture) shown in Fig. 25 are significantly more favorable for a Λ_η measurement than this extreme 90% nitrogen scenario.

It is anticipated that $N = 1400$ events integrated over an energy above 40 EeV will be observed by POEMMA, when the measured shape of the cosmic-ray spectrum above the ankle by the Pierre Auger Observatory is used [7]. The flux as measured by the TA Collaboration could yield a much higher number of events, c.f. Figs. 14 and 15, but we do not include this option here.

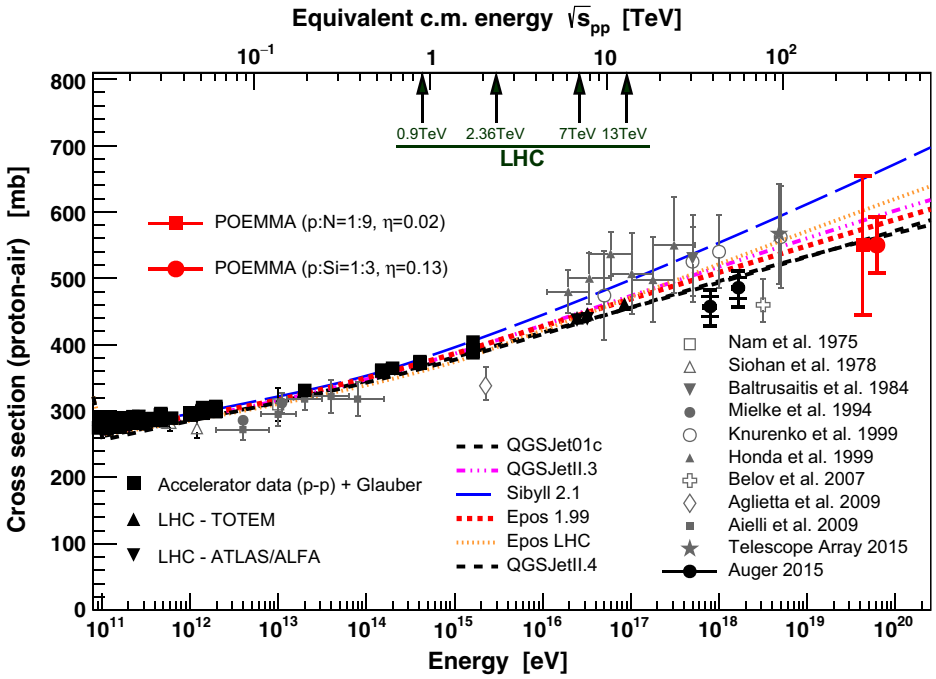

FIG. 26. Potential of a measurement of the UHE proton-air cross section with POEMMA. Shown are also current model predictions and a complete compilation of accelerator data converted to a proton-air cross section using the Glauber formalism. The expected uncertainties for two composition scenarios (left, $p:N = 1:9$; right, $p:Si = 1:3$) are shown as red markers with error bars. The two points are slightly displaced in energy for better visibility.

Since the measurement is entirely focused on the exponential slope of the tail the expected Gaussian detector resolution on the order of 35 g/cm^2 in $X_{\max}$ and 0.2 in $\Delta E/E$ does not affect this. The exponential slope Λ_η is determined by using an unbinned log L fit [109] approximated by the result in the large $X_{\max}$ limit, as described in Appendix C. Thus, the relative statistical uncertainty of Λ_η is simply $1/\sqrt{N_{\text{tail}}}$, where $N_{\text{tail}} = N\eta$ is the number of events in the tail of the $X_{\max}$ distribution.

In the following, we use two different choices for η following the guidance of the Pierre Auger Observatory: for the $p:N = 1:9$ case, η reflecting the proton content of 0.1 is reduced by an additional fraction 0.2 to minimize the potential impact of the nonproton primaries that contaminate the high $X_{\max}$ tail; for the p:Si case, since Si is a heavier primary that affects Λ_η much less, we use a fraction of 0.5 of the proton content 0.25 for the tail measurement. We arrive with a very conservative effective $\eta = 0.1 \times 0.2 = 0.02$ for the pessimistic scenario of $p:N = 1:9$, and $\eta = 0.25 \times 0.5 = 0.13$ for the more optimistic one with $p:\text{Si} = 1:3$.

Now, using the estimate of the overall number of events above 40 EeV of $N = 1400$ and combining it with expectations from cosmic-ray propagation simulations indicating possible mass composition scenarios, we can determine a projected measurement of the proton-air cross section as shown in Fig. 26. In this plot the uncertainties of the left point for POEMMA correspond to the p:N=1:9 and the right point to $p:\text{Si} = 1:3$ proton fraction scenarios. The analysis described here is not yet optimized for the actual POEMMA observations and we study two very different potential scenarios. For illustration purposes, the central value of the projected POEMMA points in Fig. 26 is located at the lower range of the model prediction. This is what some of the recent data from the Pierre Auger Observatory and also LHC suggest [110–112].

In the final step, these data are also converted into the fundamental inelastic proton-proton cross section $\sigma_{pp}^{\text{inel}}$ using an inverse Glauber formalism.

2. *Searches for superheavy dark matter*

One of the leading objectives of the particle physics program is to identify the connection between DM and the standard model (SM). Despite the fact there is ample evidence for DM existence, the specific properties and the identity of the particle DM remain elusive [113]. For many decades, the favored models characterized DM as relic density of weakly interacting massive particles (WIMPs) [114]. Theoretical ideas and experimental efforts have focused mostly on production and detection of thermal relics, with mass typically in the range of a few to a hundred GeV. However, despite numerous direct and indirect detection searches [115,116], as well as searches for DM produced at particle accelerators [117,118], there has thus far been no definitive observation of the WIMP

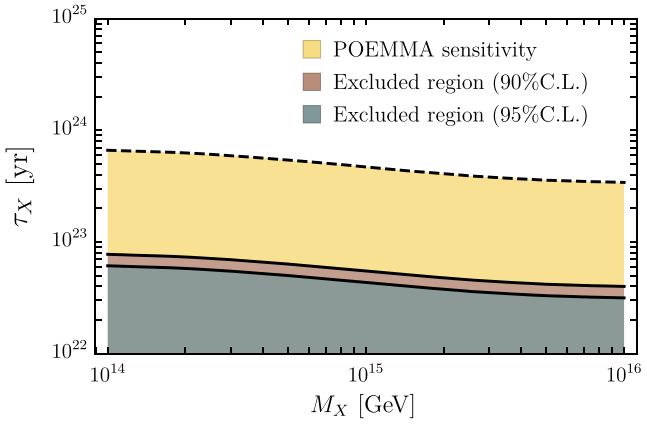

FIG. 27. Lower limit on the lifetime of SHDM particles together with the sensitivity (defined as the observation of one photon event above $10^{11.3}$ GeV in 5 years of data collection) of POEMMA operating in stereo mode [122].

particle. Moreover, as of today, there have been no definitive hints for new physics beyond the SM at any accessible energy scale [119], suggesting that nature does not too much care about our notion of naturalness. Anthropic reasoning, bastioned by probabilistic arguments of the string theory landscape, seems to indicate that if the Universe is fine-tuned, then the natural mass range for the particle DM would be the Planck scale [120–122]. Without DM, the epoch of galaxy formation would occur later in the Universe; thus galaxies would not form in time for our existence. However, it is only the DM abundance and not any other details of the dark sector that is critical for life to exist. Then it is quite reasonable to expect that the DM sector would not be as fine-tuned as the visible SM sector. Production of nonthermal superweakly interacting superheavy dark matter (SHDM) particles is ubiquitous in string theory [123,124]. While SHDM must be stable over cosmological timescales, instanton decays induced by operators involving both the hidden sector and the SM sector may give rise to observable signals in the spectrum of UHECRs [125,126].

When SHDM decays into SM particles, photons and neutrinos dominate the final state. The energy spectra depend on the exact decay mechanism and are somewhat model dependent. There are several computational schemes proposed in the literature [127–130], which predict accurately the secondary spectra of SM particles produced in the decay of SHDM X-particles and agree well each other. The expected energy distribution on Earth follows the initial decay spectrum, whereas the angular distribution incorporates the (uncertain) distribution of dark matter in the Galactic halo via the line-of-sight integral [131–134]. The photon energy flux is estimated to be $\Phi_\gamma \propto (M_X \tau_X)^{-1}$, where M_X is the mass of the particle and τ_X its lifetime [135,136]. The nonobservation of extreme-energy photons can be used to constrain the $\tau_X - M_X$ parameter space. In Fig. 27 we show the lower limit on the lifetime of SHDM particles from the nonobservation of UHECR photons at Auger together with the sensitivity of POEMMA operating in stereo mode [122]. CMB observations set a bound $M_X \lesssim 10^{16}$ GeV at 95% C.L. [120]. Detection of an extreme-energy photon would be a momentous discovery. If this were the case POEMMA could be switched into limb mode to rapidly increase statistics. Note that for energies $E \gtrsim 10^{20}$ eV, the average $X_{\max}$ of photon and proton showers differs by more than 100 g/cm^2 [94]. This implies that POEMMA operating in limb-viewing mode, with $X_{\max}$ resolution ~100 g/cm^2 determined from simulated monocular reconstruction performance, will be able to deeply probe the SHDM parameter space.

3. Searches for neutrinos from decaying topological defects

Beyond SM physics often also predicts phase transitions at which topological defects are formed [137]. The decay of topological defects is also dominated by photons and neutrinos, but since these relics are expected to be distributed uniformly throughout the Universe the photon signal would cascade down to lower energies and extreme-energy neutrinos become the smoking gun.

POEMMA will be a powerful probe of extreme-energy neutrino emission. An example involves the flux neutrinos produced via decay of highly boosted (strongly coupled) moduli, radiated by relic cosmic strings [138]. These strongly coupled moduli are scalar fields, which appear to be quite generic in the string theory landscape [139,140].

In Fig. 28 we show the sensitivity of both POEMMA and the future Lunar Orbital Detector (LORD) [141], and current limits from ANITA I-IV [91] and WSRT [142]. We also show the neutrino flux range resulting from models of strongly coupled moduli in a string theory background with $G\mu \sim 10^{-20}$, where G is the Newton's constant and μ the string tension [138]. POEMMA sensitivity was estimated assuming the stereo configuration observations with 10% duty cycle and 5 years of observation time. The neutrino aperture is the result of simulations of isotropic events interacting deep in the atmosphere (observed starting point $X_{\text{Start}} \geq 2000$ g/cm^2). The sensitivity includes all flavors, charged and neutral current interactions, for two different cross sections as estimated in [143] and [144]. POEMMA UHE neutrino simulated neutrino air fluorescence response is detailed in Appendix D.

It is evident that POEMMA will probe a significant part of the parameter space, providing a method of searching for strongly coupled moduli, which complements searches based on gravitational effects of strings, like structure formation, cosmic microwave background, gravitational radiation, and gravitational lensing. The strongest current bound from lensing effects is estimated to be $G\mu \lesssim 10^{-7}$

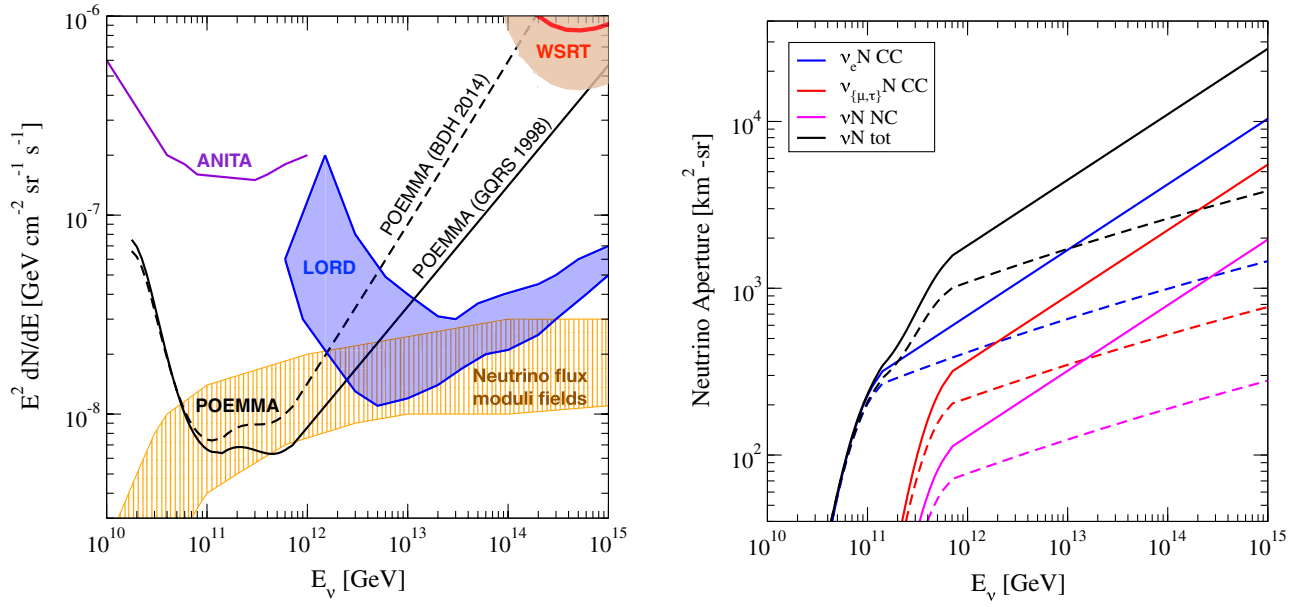

FIG. 28. POEMMA sensitivity to EAS showers produced by neutrinos interacting in the atmosphere. Left: Black curves are POEMMA sensitivity using [143] (solid) and [144] (dashed) cross sections: Predictions for strongly coupled string moduli (orange range) [138], LORD sensitivity (blue band) [141], ANITA I-IV limits (purple) [91], and WSRT [142]. Right: POEMMA neutrino aperture from fluorescence with [143] (solid) and [144] (dashed) cross sections of neutrino-nucleon scattering for CC interactions of ν_e (blue), ν_μ, and ν_τ (red), NC interactions (pink),and total (black).

[145], while millisecond pulsar observations lead to $G\mu \lesssim 4 \times 10^{-9}$ [146]. Next-generation gravitational wave detectors are expected to probe $G\mu \sim 10^{-12}$ [147,148]. Thus, POEMMA will attain sensitivity to a region of the parameter space more than 10 orders of magnitude below current limits and about 8 orders of magnitude smaller than next-generation gravitational wave detectors. It should be noted that these stereo fluorescence neutrino measurements effectively "come for free" when POEMMA is in stereo UHECR observation mode.

VI. CONCLUSIONS

The transformational UHECR physics performance of POEMMA above 40 EeV is based upon the large, all-sky exposure enabled by a stereo UHECR space-based experiment. POEMMA is designed with wide FoV Schmidt optics coupled to relatively fine pixel resolution to provide excellent angular, energy, and $X_{\rm max}$ resolutions, using stereo UHECR reconstruction. This performance translates into high sensitivity for UHECR composition determination, UHECR anisotropy and source determination, and providing fundamental physics measurements on dark matter and proton-proton cross sections along with remarkable UHE neutrino sensitivity at the highest energies ever achieved. We have shown that POEMMA will provide new multimessenger windows onto the most energetic environments and events in the Universe, enabling the study of new astrophysics and particle physics at these otherwise inaccessible energies.

ACKNOWLEDGMENTS

We thank our colleagues of POEMMA, Pierre Auger, and JEM-EUSO collaborations for some valuable discussion. This work has been supported by NASA (Grants No. 80NSSC18K0464, No. NNX17AJ82G, and No. 17-APRA17-0066), the U.S. National Science Foundation (NSF Grant No. PHY-1620661), and the U.S. Department of Energy (Grant No. DE- SC-0010113).

APPENDIX A: MODELING POEMMA USING ESAF

A first estimation of POEMMA performance in terms of trigger exposure and quality of event reconstruction has been assessed using the ESAF code assuming a clear atmosphere. Because the POEMMA PFC is baselined to use the PDMS and electronics developed for the JEM-EUSO mission, it is reasonable to adopt the JEM-EUSO trigger algorithms and reconstruction procedures to evaluate the performance of POEMMA.

Here we provide an overview of ESAF. The Greisen-Ilina-Linsley (GIL) function [149] is used as parametric generator to reproduce the profile as a function of slant depth. The GIL function is optimized to reproduce EAS from hadronic particles simulated by CORSIKA [150] with the QGSJET01 hadronic interaction model [151]. Proton showers have been simulated for the analyses presented in this paper. This is motivated by the fact that they develop deeper in the atmosphere, which results in a higher atmospheric absorption and higher cloud impact.

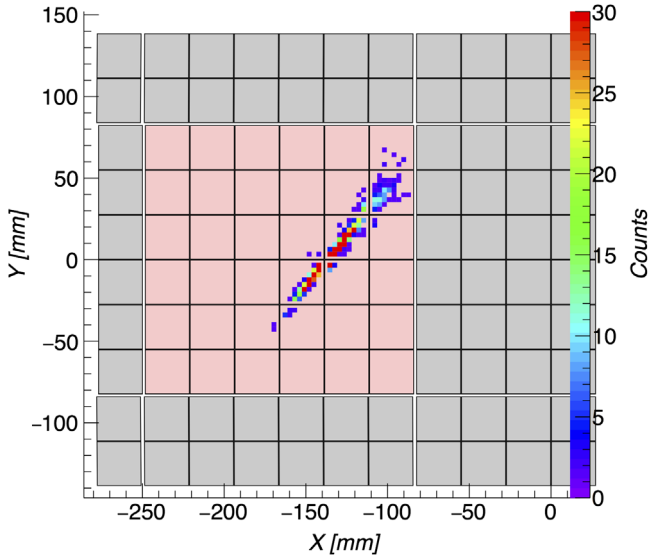

FIG. 29. EAS fluorescence image on one POEMMA PDM for a 100 EeV, 60° inclined shower. Background is not shown.

Therefore, the results that are discussed in the following sections constitute a conservative estimation on the performance of the instrument. In the present work, the fluorescence yield is taken from [152]. In the atmosphere, UV photon propagation is strongly affected by Rayleigh scattering and absorption by ozone for wavelengths < 320 nm. These processes along with the atmospheric profile are modeled with the LOWTRAN package [153].

The POEMMA detector was implemented in ESAF [154] using the parametric optical model shown in Fig. 3. A single telescope, which allows for the calculation of POEMMA's monocular mode performance, was considered since ESAF does not allow yet a stereoscopic vision. The trigger efficiency is determined at single telescope level, because POEMMA's telescopes operate independently regardless of mode of operation. The simulations were performed assuming a standard UV night glow background level of 500 photons/m^2/ns/sr in the 300–500 nm band [59], which is appropriate considering the use of a BG3 UV filter in the PFC. Taking into account the POEMMA detector response this corresponds to an average equivalent count rate 1.54 counts/μs/pixel. In Fig. 29 we show the track image in a PFC focal plane of a typical proton EAS of 100 EeV, 60° inclined from the nadir.

1. Trigger efficiency

To estimate the trigger efficiency curve of POEMMA, an overall set of 20 000 proton EAS was simulated with ESAF using the following parameters: primary energy (E) in the range $5 \leq E/\mathrm{EeV} \leq 500$, zenith angle $0 \leq \theta \leq \pi/2$, and azimuth angle $0 \leq \phi \leq 2\pi$. To avoid border effects EAS were simulated on an area that is almost twice the size,

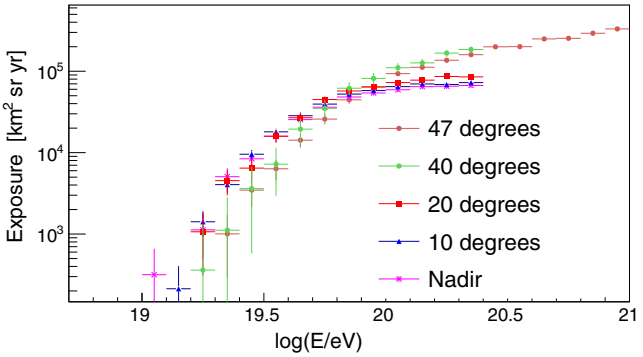

FIG. 30. Exposure curve of POEMMA monocular observation. Different curves correspond to different tilting angles.

namely, $S_{\mathrm{FoV}} \sim 145,000$ km^2 and $S_{\mathrm{sim}} \sim 271\,000$ km^2. The exposure is then calculated according to

$$\mathcal{E}(E) = A_{\mathrm{geo}}(E) t \epsilon, \tag{A1}$$

where

$$A_{\mathrm{geo}}(E) = \int_{S_{\mathrm{sim}}} dS \int_0^{2\pi} d\phi \int_0^{\pi/2} d\theta \cos\theta \sin\theta \epsilon(E) \tag{A2}$$

is the geometrical aperture, t is the observation time,

$$\epsilon(E) = \frac{N_{\mathrm{trig}}}{N_{\mathrm{sim}}} \tag{A3}$$

is the average efficiency of the detector at a given energy E, and N_{trig} and N_{sim} are respectively the number of triggering events and the number of simulated events at a certain energy E. The events were passed through the electronics, and the response of the first JEM-EUSO trigger level was applied [155]. This trigger level is based on an excess of signal in a box of 3×3 pixels for five consecutive GTUs. The thresholds for this signal excess reduce the rate of fake trigger at the level of ~7 Hz/PDM. The second trigger level, which is not applied here, looks for a signal excess on a track, lasting 15 GTUs. The thresholds are set to have a fake trigger rate of ~0.1 Hz/FS. According to simulations for the JEM-EUSO mission, the application of this second trigger level shifts the trigger efficiency curve by ~10% at higher energies. In Fig. 30 we show the exposure determined for the nadir mode and different tilt angles away from the nadir.

2. Reconstruction performance in monocular nadir observation

A first evaluation of the reconstruction performance in the monocular mode and nadir pointing was performed using the same algorithms defined for JEM-EUSO. No optimization has been introduced yet, like the use of a shorter GTU (1 μs). Therefore, the results presented in this

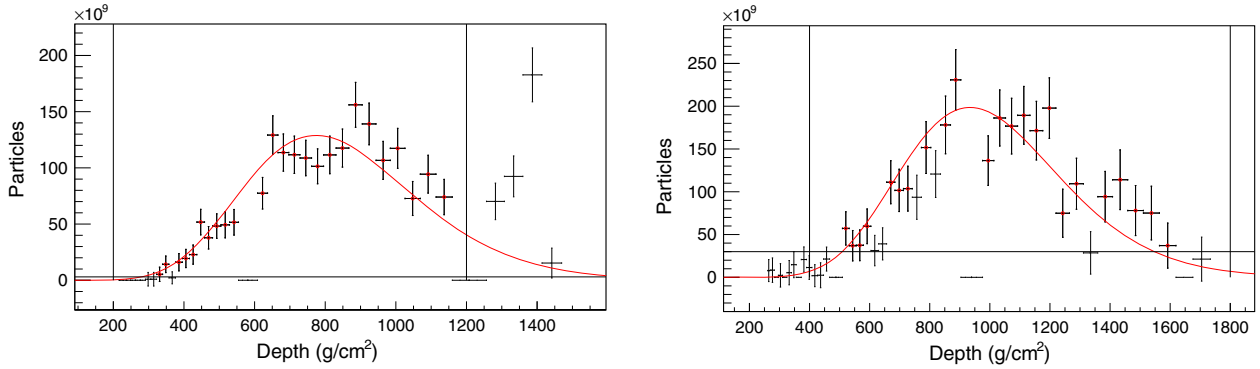

FIG. 31. Example of reconstructed events. The event on the left ($E = 1.7 \times 10^{20}$ eV, $\theta = 49.6°$ and $\phi = 9.2°$) has been reconstructed with the Cherenkov method (it is possible to recognize the Cherenkov peak—blue dotted line). The right one ($E = 2.5 \times 10^{20}$ eV, $\theta = 56.3°$ and $\phi = 344.0°$) has been reconstructed by the method based on the direction reconstruction (slant depth method). The red fitted lines are the GIL functions (an analytical approximation of the EAS longitudinal development—details can be found in [156]). The vertical black lines identify the fitting interval and the horizontal one the background level.

work have to be considered conservative. Two different pattern algorithms have been defined in ESAF to reconstruct the EAS parameters. The "LTTPatternRecognition" was developed to collect as much signal as possible from the EAS track to get a better estimation of the EAS energy, even at the expenses of the uncertainty in the direction reconstruction. The details of this method are reported in [156]. On the other hand, the *PWISE* method developed for the track direction is meant to make the track as narrow as possible to reduce the uncertainty on the direction reconstruction. In the following, results are shown applying the two chains independently. Before proceeding, it is important to underline that a failure of the PWISE algorithm does not imply that the event cannot be reconstructed, as the chain for the reconstruction of the energy would anyway provide a first estimation of the arrival direction. Naturally, the ideal case would be to use both algorithms in parallel in order to get as much information as possible for the same event.

The triggered EAS were passed through JEM-EUSO reconstruction algorithms discussed in [156] to evaluate the quality in the EAS reconstruction for the POEMMA detector.

In JEM-EUSO two methods have been developed to determine the altitude of the shower maximum: the Cherenkov method and the method based on the direction reconstruction (slant depth method). The Cherenkov method uses the Cherenkov reflection mark, which identifies the location and time at which the EAS reaches the ground. This method can be applied only for vertical EAS, for which the Cherenkov mark is bright enough and it is located on a limited number of pixels. For more inclined EAS, such a peak is spread in time and space and cannot be identified. The slant depth method assumes a parametrization for the depth of the shower maximum and relies on the direction delivered by the direction reconstruction.

Before applying the reconstruction algorithms, a pattern recognition algorithm is applied to the data to identify the

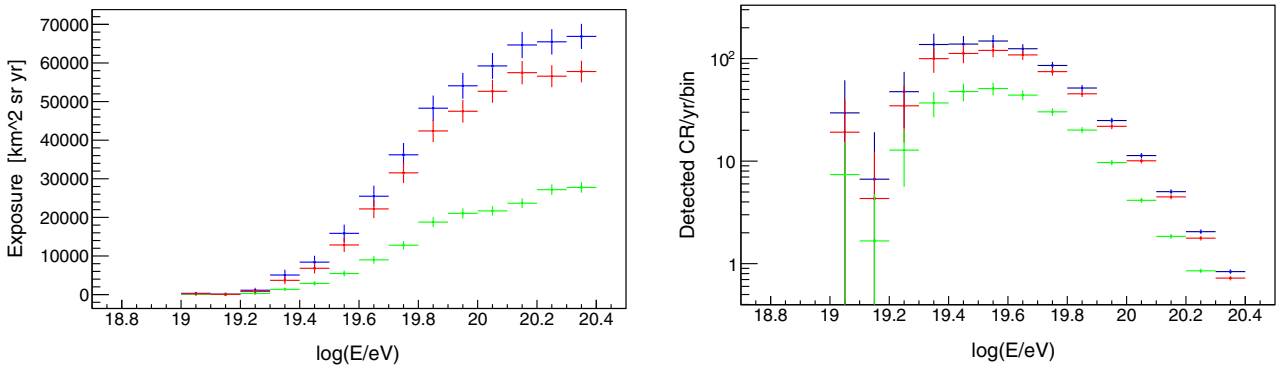

FIG. 32. Left: Comparison between the exposures obtained from POEMMA simulations (triggered events, blue; events reconstructed by Cherenkov method, green; events reconstructed by the slant depth method, red). Right: Comparison between the triggered spectra obtained from POEMMA simulations (triggered events, blue; events reconstructed by Cherenkov method, green; events reconstructed by the slant depth method, red).

TABLE III. Comparison between the number of triggered and reconstructed events above an energy $log(E/\mathrm{eV}) = 19.6$.

	Cherenkov method	Slant depth method
Triggered	305	305
Reconstructed	110 (→ 36%)	267 (→ 88%)

center of the spot in each GTU. Indeed, for each event, the background is simulated on all the PDMs that were crossed by the EAS event. Therefore, the signal due to the EAS cascade has to be extracted from background. This is done to mimic the real conditions expected on flight.

The reconstruction of events was performed using both methods separately. In Fig. 31 we show two examples of reconstructed events. On the left panel, it is possible to recognize the Cherenkov peak. This event can be reconstructed using the Cherenkov method and the slant depth method. Instead, on the right panel, the Cherenkov peak is not present and the event can be reconstructed only using the slant method.

To perform a reconstruction, we carry out a chi-square goodness of fit test with a number of degrees of freedom > 4 and the likelihood satisfying $0.1 < \chi^2 < 3$. For this analysis, 11,200 events were simulated in the energy range $19.2 \leq \log(E/\mathrm{eV}) \leq 20.8$. Out of the total, 3,879 events (∼35%) were triggered and passed through the pattern recognition algorithm and EAS reconstruction chain. From this selected sample, 3,253 events (equivalent to ∼84%) were successfully reconstructed by the slant method and 1,472 events (equivalent to ∼38%) by the Cherenkov method. It is not surprising that in the Cherenkov method only about half of the events were reconstructed. As mentioned before this is due to the fact that this method is usable up to zenith angles ∼50° [the value depends on energy and EAS location on the focal surface (FS)]. At higher zenith angles the Cherenkov signal is too dim to be isolated from background fluctuations.

In the left panel of Fig. 32 we show a comparison between the triggered and reconstructed spectra using both reconstruction methods. In the right panel of this figure we show the expected number of detected and reconstructed events per year assuming the Pierre Auger energy spectrum.

A comparison between the number of triggered events and the number of events automatically reconstructed with the two reconstruction methods for $log(E/eV) > 19.6$ is provided in Table III. When a selection cut is placed at

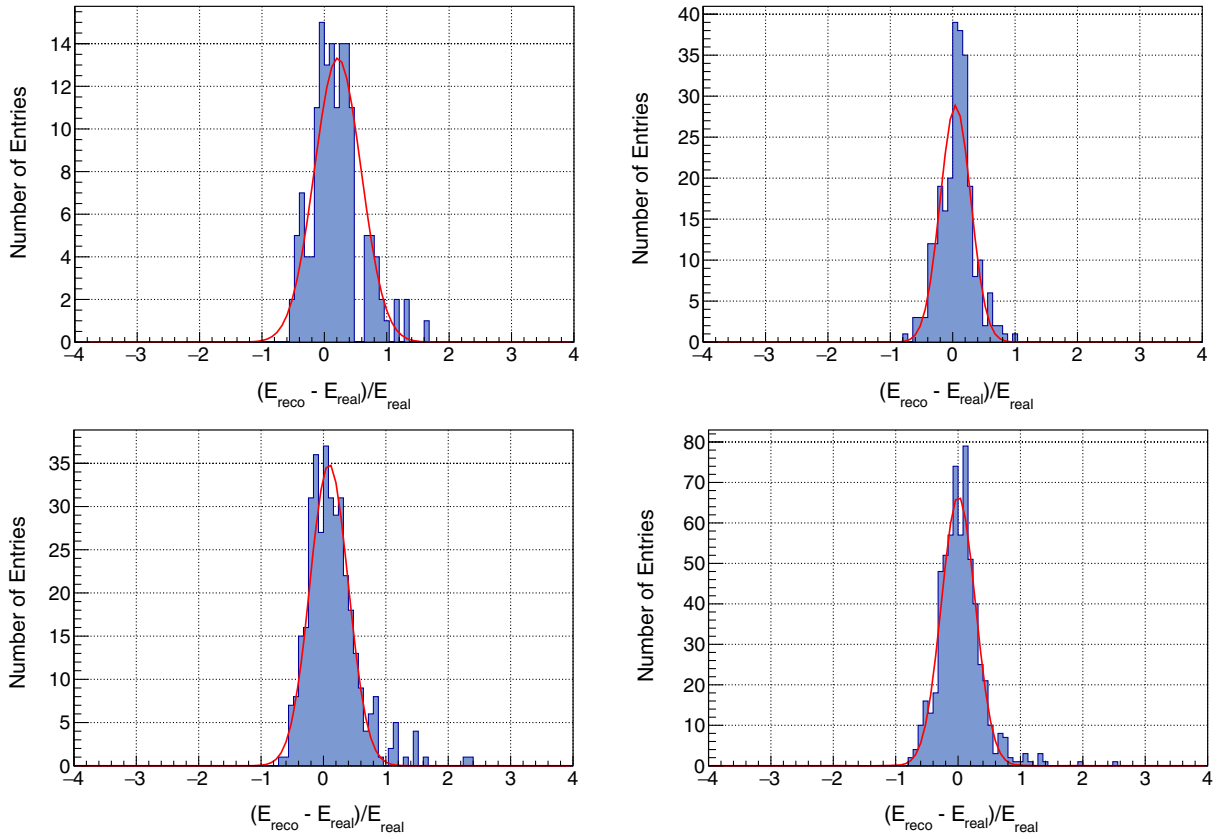

FIG. 33. Energy resolution $(E_{\mathrm{reco}} - E_{\mathrm{real}})/E_{\mathrm{real}}$ for events belonging to two different energy intervals (low energy on the left panels and high energy on the right panels). The top plots refer to the performance of the Cherenkov method while the bottom ones refer to the slant depth method.

TABLE IV. X_{max} and energy resolutions (all EAS included) for the two methods adopting either an automatic or a manual reconstruction procedure.

Lower E		X_{max} (g/cm^2) Cherenkov method	Bias	σ
Bias	21%	Automatic	12	128
Resolution	37%	Manual	−13	107
Higher E		E (%) Cherenkov method	Bias	σ
Bias	4%	Automatic	−10	25
Resolution	20%	Manual	−11	25
Lower E		X_{max} (g/cm^2) Cherenkov method	Bias	σ
Bias	9%	Automatic	37	100
Resolution	30%	Manual	34	110
Higher E		E (%) Slant depth method	Bias	σ
Bias	0.5%	Automatic	8	21
Resolution	27%	Manual	11	21

$log(E/eV) = 19.6$, the overall fraction of reconstructed events above this energy is slightly higher than using all the data sample. In particular, the slant depth method approaches 90% efficiency in EAS reconstruction.

In Fig. 33 we show the relative energy resolution $(E_{reco} - E_{real})/E_{real}$ applying the two methods for two different energy intervals. All zenith angles are included. In Table IV we describe the performance on X_{max} and energy reconstruction including all the reconstructed EASs using the two methods. To test the validity of the automatic procedure, in parallel the same EASs have been reconstructed manually. As one can easily verify in Table IV the results of the automatic procedure are consistent with those obtained adopting the manual reconstruction. This indicates that the automatic algorithm is quite effective on its own. However, the manual procedure allowed to remove four events for which the result of the automatic procedure was providing a very bad result. This might happen when the EAS goes through gaps between PDMs and the automatic algorithm fails to reject those points for the fitting procedure.

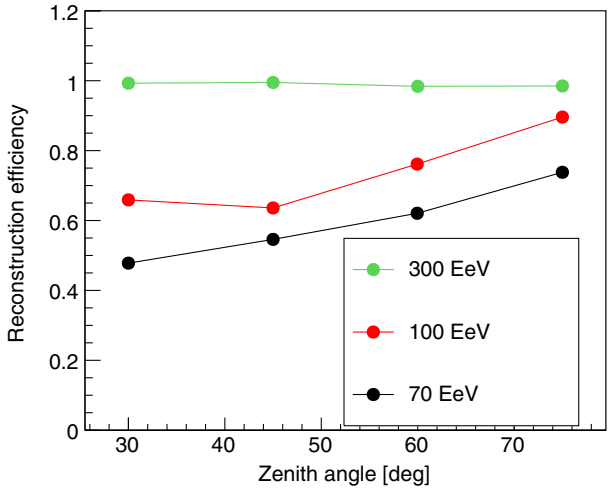

FIG. 34. Efficiency in the angular reconstruction for POEMMA as a function of zenith angle for different EAS energies.

3. Angular reconstruction

The angular reconstruction for POEMMA was evaluated at fixed zenith angles ($\theta = 30°, 45°, 60°$ and 75°) for three different energies (E = 7×10^{19}, 10^{20} and 3×10^{20} eV). The same methodology defined for JEM-EUSO reconstruction performance was applied to POEMMA, with a fine-tuning of the parameters of the *PWISE* algorithm. Figure 34 shows the reconstruction efficiency as a function of zenith angle for the three different energies. The reconstruction efficiency is defined as the ratio $\epsilon_{reco} = \frac{N_{reco}}{N_{trig}}$. About 1000 EAS are simulated in each condition (see Table V for details). In order to define that the pattern recognition is successful at least ten pixels should have been selected in the track by the *PWISE* algorithm. The same pixel can be selected more than once in the track, i.e., in consecutive GTUs. These selection criteria tend to make the angular reconstruction less efficient at lower energies and for lower zenith angles. This is an important parameter that needs to be explored with more details in the future. Moreover, by reducing the GTU to 1 μs, the number of selected pixels might increase considerably. To estimate the expected angular resolution of POEMMA, as in JEM-EUSO, we compared the angle (γ) between the injected shower axis and the reconstructed one. We define $\gamma_{68\%}$ as the value at which the cumulative distribution of γ reaches 0.68. It is worth mentioning that both systematic errors and statistical fluctuations are included within the definition of $\gamma_{68\%}$. We use this parameter as a measurement of the overall performance of the reconstruction capabilities. Figure 35 shows the results in terms of $\gamma_{68\%}$ for different zenith angles and energies. Details can be found in Table V. It is important to underline that a more detailed study of the bias

TABLE V. Angular performance for θ, ϕ and $\gamma_{68\%}$. All numbers are expressed in degrees. The number of triggered and reconstructed events and their ratio are reported as well.

E(eV)	θ_{sim}	N_{trig}	N_{reco}	ϵ_{reco}	$\langle\Delta_\theta\rangle$	$\sigma(\Delta_\theta)$	$\langle\Delta_\phi\rangle$	$\sigma(\Delta_\phi)$	$\gamma_{68\%}$
7×10^{19}	30	697	333	0.47	2.5	2.9	0.3	7.4	9.9
	45	780	426	0.54	1.0	2.0	0.1	3.3	6.4
	60	910	563	0.61	−0.5	2.2	0.1	2.0	3.9
	75	1063	785	0.73	−0.7	2.6	−0.1	1.1	5.1
10^{20}	30	948	625	0.65	2.8	3.0	−4.1	6.6	9.1
	45	1022	651	0.63	0.4	2.1	−0.1	2.7	4.2
	60	1062	808	0.76	−0.5	2.3	0.3	2.0	3.5
	75	1127	1010	0.89	−1.0	1.6	0.0	0.9	4.1
3×10^{20}	30	1101	1094	0.99	4.7	2.1	0.0	3.8	6.2
	45	1119	1114	0.99	−0.9	1.5	0.0	1.3	2.3
	60	1128	1111	0.98	−1.0	1.0	0.0	0.7	2.1
	75	1136	1119	0.98	−0.5	0.8	0.0	0.4	1.4

should be performed. The reduction of the bias would be capable of improving the overall performance of $\gamma_{68\%}$ as it includes both statistical and systematic uncertainties. The reconstruction performance improves also by reducing the GTU to 1 μs.

4. ESAF estimate of stereo energy resolution

The ESAF simulation was used to estimate the stereo reconstructed energy resolution via imposing an angular resolution defined by Gaussian distributions with $\sigma = 1°$ for the zenith and azimuth angles. Isotropic UHECRs were generated from 0°–90° zenith angles at two energies, 50 and 100 EeV, assuming nadir pointing of a single POEMMA telescope. The events were then reconstructed assuming 1° resolutions. The results for the energy reconstruction are shown in Fig. 36. For 50 EeV, the energy resolution is 26% with a +3.5% bias, while for 100 EeV the energy resolution is 24% with a −1.5% bias. Since the two POEMMA telescopes provide independent measurements of each EAS, the combined resolution is obtained by dividing by $\sqrt{2}$, yielding 18% at 50 EeV and 17.0% at 100 EeV.

5. Summary

A first estimation of POEMMA performance in terms of trigger exposure and quality of event reconstruction has been assessed using the ESAF code for the clear atmosphere case. The same trigger algorithms and reconstruction procedures developed for JEM-EUSO have been applied to POEMMA. A parametrized optics has been adopted. Results of the EAS reconstruction refer to the nadir configuration, while the trigger exposure has been obtained also for tilted configurations. It is important to underline that a 2.5 μs GTU has been used in this study. POEMMA is expected to adopt a shorter GTU of 1 μs; therefore, the

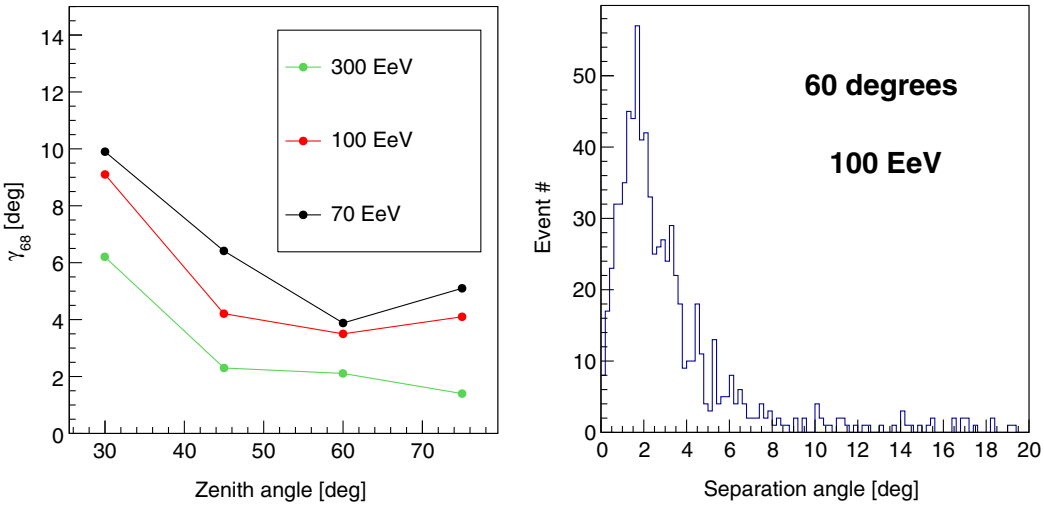

FIG. 35. Left: Angular resolution for POEMMA defined through the $\gamma_{68\%}$ parameter. The circled point indicates that a limited bias exists for these points; see Table V for details. Right: Distribution of the $\gamma_{68\%}$ parameter for $E = 10^{20}$ eV and $\theta = 60°$.

TABLE VI. TS values for various astrophysical scenarios.

Catalog	$f_{\rm sig}$	Θ	TS	σ	$f_{\rm sig}$	Θ	TS	σ
SBG	5%	5°	33.6	5.4	15%	5°	228.1	14.9
	5%	10°	12.8	3.1	15%	10°	101.9	9.8
	5%	15°	6.2	2.0	15%	15°	54.2	7.1
	5%	20°	3.4	1.3	15%	20°	29.5	5.1
	5%	25°	1.7	0.8	15%	25°	16.1	3.6
	10%	5°	115.4	10.5	20%	5°	369.8	19.1
	10%	10°	48.1	6.6	20%	10°	170.9	12.9
	10%	15°	24.7	4.6	20%	15°	92.9	9.4
	10%	20°	13.0	3.2	20%	20°	51.4	6.9
	10%	25°	7.0	2.2	20%	25°	27.9	4.9
2MRS	5%	5°	7.7	2.3	15%	5°	63.2	7.7
	5%	10°	3.7	1.4	15%	10°	31.4	5.2
	5%	15°	2.4	1.0	15%	15°	20.0	4.1
	5%	20°	1.5	0.7	15%	20°	13.6	3.3
	5%	25°	0.9	0.5	15%	25°	8.9	2.5
	10%	5°	29.8	5.1	20%	5°	105.7	10.0
	10%	10°	14.2	3.4	20%	10°	55.2	7.1
	10%	15°	8.7	2.5	20%	15°	35.2	5.6
	10%	20°	5.9	1.9	20%	20°	23.5	4.5
	10%	25°	3.9	1.5	20%	25°	15.1	3.5
Swift-BAT AGN	5%	5°	39.9	6.0	15%	5°	248.5	15.6
	5%	10°	19.1	4.0	15%	10°	137.7	11.5
	5%	15°	10.4	2.8	15%	15°	82.4	8.8
	5%	20°	6.7	2.1	15%	20°	53.2	7.0
	5%	25°	4.2	1.5	15%	25°	36.4	5.7
	10%	5°	129.9	11.2	20%	5°	392.3	19.6
	10%	10°	67.2	7.9	20%	10°	224.4	14.8
	10%	15°	39.6	6.0	20%	15°	139.3	11.6
	10%	20°	24.9	4.6	20%	20°	91.5	9.3
	10%	25°	16.1	3.6	20%	25°	62.4	7.6

quality in trigger reconstruction and in the trigger efficiency will improve. Therefore, the results obtained in this study have to be considered as conservative ones. It is worth mentioning finally that ∼88% of the triggered events were successfully reconstructed for the energy parameter above $log(E/eV) = 19.6$. This is important because it indicates that the exposure curve provides already reliable information on the number of events that could be retained for further analysis.

The angular reconstruction still needs improvements in terms of reconstruction efficiency. Most probably a too severe threshold on the number of points has been applied.

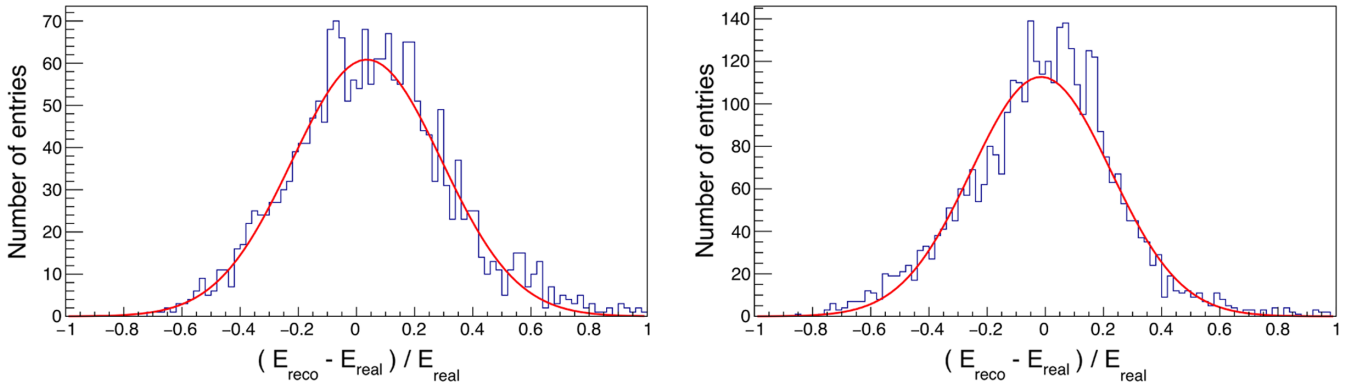

FIG. 36. ESAF simulated energy resolution assuming 1° zenith and azimuth angular resolution: Left, 50 EeV results; right, 100 EeV results.

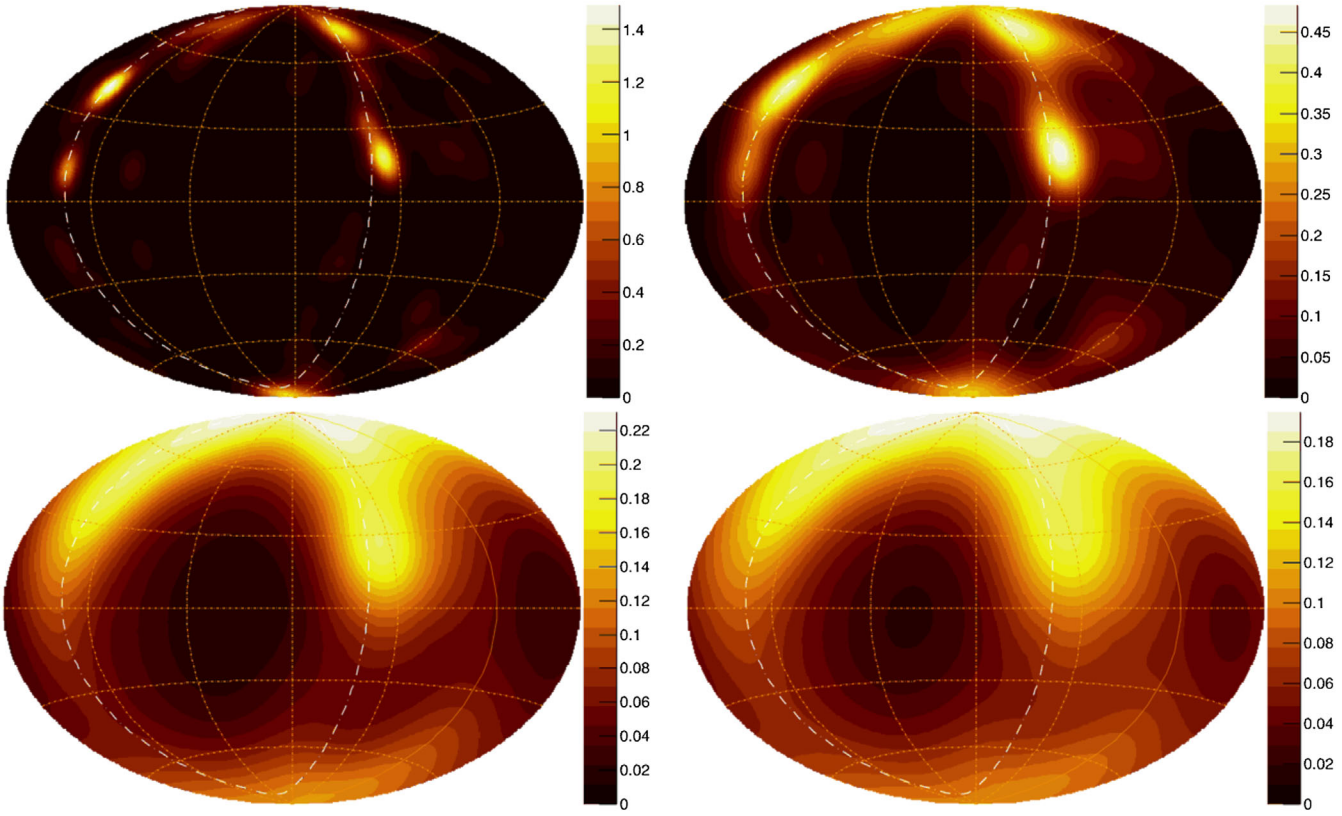

FIG. 37. Normalized source sky maps for nearby galaxies from the 2MRS catalog [105] weighted by K-band flux corrected for Galactic extinction, the attenuation factor accounting for energy losses incurred by UHECRs through propagation, and the exposure of POEMMA. The maps have been smoothed using a von Miser-Fisher distribution with concentration parameters corresponding to angular spreads of $\Theta = 5°$ (top left), 10° (top right), 20° (bottom left), and 25° (bottom right). The color scales indicate $\mathcal{F}_{\rm src}$ as a function of position on the sky. The white dot-dashed line indicates the supergalactic plane.

Nevertheless, because the energy reconstruction provides also an angular reconstruction, in case of a failing of the *PWISE algorithm*, the information of the angular resolution could be retained from the chain employed for the energy reconstruction.

APPENDIX B: METHODOLOGY FOR ANISOTROPY SEARCHES CROSS-CORRELATING WITH ASTROPHYSICAL CATALOGS

In order to determine the reach of POEMMA in detecting anisotropy through cross-correlating with astrophysical catalogs, we perform a detailed statistical study simulating POEMMA data sets assuming either the starburst or AGN hypothesis and comparing them against the null hypothesis of isotropy. In so doing, we follow the likelihood ratio approach of Abbasi *et al.* [[36]; see also, [3,35,106]]. For each constructed mock data set (see Sec. V C 2), we express the astrophysical hypotheses as sky models in which the flux of UHECRs consists of either a purely isotropic distribution or an isotropic component with an anisotropic component arising from astrophysical sources,

$$\mathcal{F}_{\rm sky}(\hat{n}) = \frac{\omega(\hat{n})}{\mathcal{C}}\left[(1-f_{\rm sig})\frac{1}{4\pi} + f_{\rm sig}\mathcal{F}_{\rm src}(\hat{n})\right], \quad \text{(B1)}$$

where $\mathcal{F}_{\rm sky}(\hat{n})$ is the probability density sky map, $\hat{n}$ is the unit vector for a given location on the sky, $\omega(\hat{n})$ is the exposure in the direction of $\hat{n}$, $f_{\rm sig}$ is the signal fraction (the fraction of UHECRs originating from the sources), $\mathcal{F}_{\rm src}$ is the normalized source sky map for the flux of UHECRs originating from the sources, and $\mathcal{C}$ is a normalization factor to ensure that $\int \mathcal{F}_{\rm sky}(\hat{n})d\Omega$. We construct $\mathcal{F}_{\rm src}$ as the weighted sum of the UHECR flux from sources of the source class under consideration, assuming that the flux of UHECRs from each individual source is proportional to its electromagnetic flux. Each source is weighted by a von Mises-Fisher distribution[3] with angular spread Θ and an attenuation factor that accounts for UHECR energy losses through propagation. We then construct normalized source sky maps from sources in one of the flux-limited

[3]The equivalent of a Gaussian distribution on the surface of a sphere. For the 2-sphere, it is given by $\mathcal{G}(\hat{n},\hat{s};\kappa) = \kappa \exp(\hat{n}\cdot\hat{s})/(4\pi\sinh\kappa)$, where $\kappa = \Theta^{-2}$ is the concentration parameter.

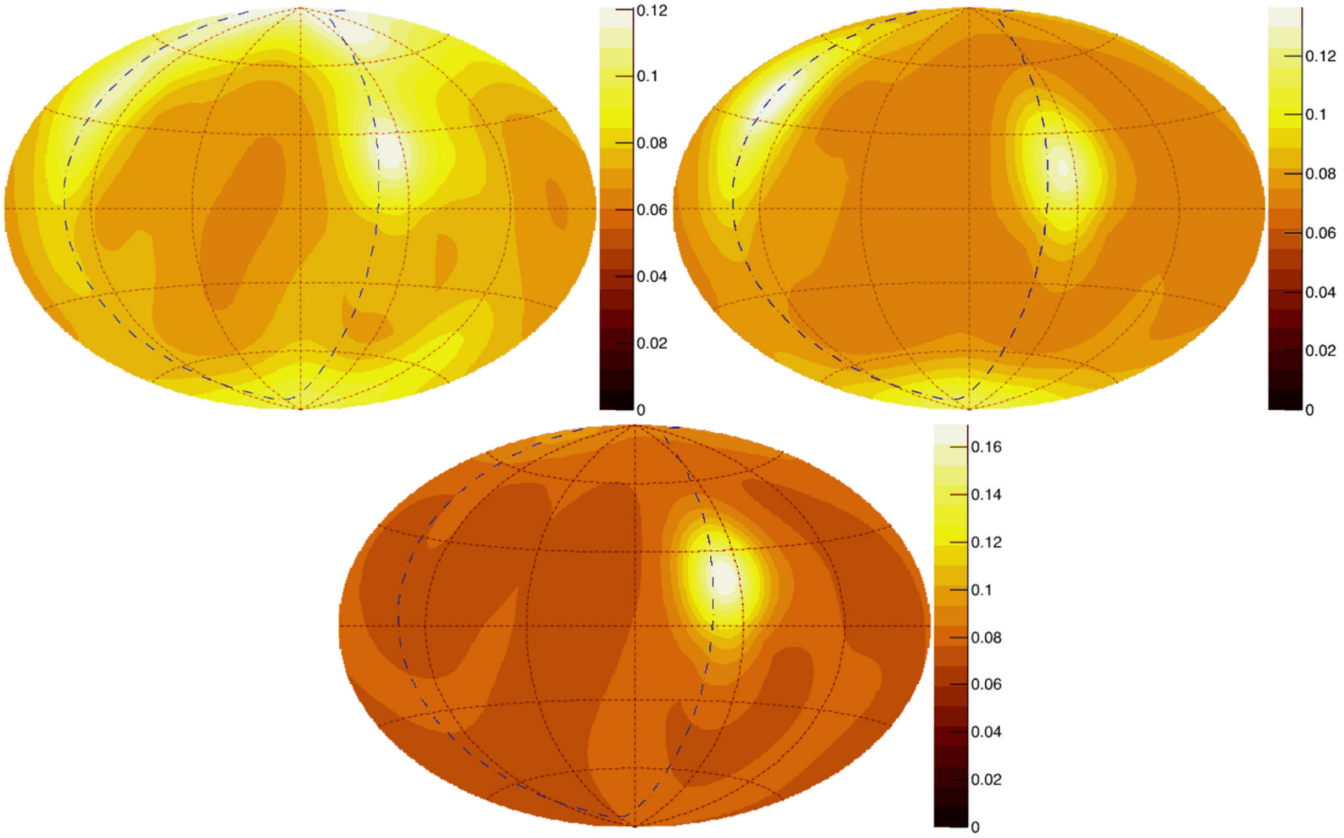

FIG. 38. Probability density sky maps corresponding to the select astrophysical scenarios with parameters selected based on the best-fit parameters from Ref. [103]. Top left: 2MRS galaxies with $f_{\rm sig} = 19\%$ and $\Theta = 15°$. Top right: Starburst galaxies with $f_{\rm sig} = 11\%$ and $\Theta = 15°$. Bottom: *Swift*-BAT AGNs with $f_{\rm sig} = 8\%$ and $\Theta = 15°$. The color scales indicate $\mathcal{F}_{\rm sky}$ as a function of position on the sky. The blue dot-dashed line indicates the supergalactic plane.

catalogs used for this study (see Sec. V C 2). In Fig. 37, we provide examples of normalized source sky maps ($\mathcal{F}_{\rm src}(\hat{n})$) constructed from nearby galaxies in the 2MRS catalog for various values for the concentration parameter. In Fig. 38, we provide examples of probability density sky maps ($\mathcal{F}_{\rm sky}(\hat{n})$) corresponding to select astrophysical scenarios in which the flux of UHECRs consists of an isotropic component and an anisotropic component as defined above. Parameters for the displayed scenarios are chosen to coincide with the best-fit search parameters reported by Ref. [103] for the given astrophysical source catalogs.

The null and alternative hypotheses are tested using mock data sets of a given number of events drawn from the astrophysical source sky maps assuming a given signal fraction and angular spread. For each mock data set, we calculate the TS as a function of the search parameters; see Table VI. The TS value is computed as the likelihood ratio for the modeled sky maps for the null and alternative hypotheses,

$$\mathrm{TS} = 2\ln\left(\frac{L(\mathcal{F}_{\rm sky})}{L(\mathcal{F}_{\rm iso})}\right), \tag{B2}$$

where $\mathcal{F}_{\rm iso} = \omega(\hat{n})/4\pi$ and the likelihood is given by

$$L(\mathcal{F}) = \frac{1}{\mathcal{N}}\prod_i \mathcal{F}(\hat{n}_i). \tag{B3}$$

APPENDIX C: DETERMINATION OF THE *p*-AIR INTERACTION LENGTH

To assess POEMMA's ability to measure $\sigma_{p\text{-air}}$, we use the method of fitting the shape of the large $X_{\rm max}$ tail of $\mathrm{d}N/\mathrm{d}X_{\rm max}$ with an exponential $\exp(-X_{\rm max}/\Lambda_\eta)$ [107], where Λ_η is proportional to the p-air interaction length, which is, in turn, proportional to the inverse of the proton-air cross section. Here, η refers to the fraction of the showers included in the tail, predominantly proton induced, as discussed in Sec. V D 1.

The value of η in our analysis is translated to a starting value of $X_{\rm max}$, $X_{\rm max}^{\rm start}$. The attenuation parameter Λ_η is determined from the unbinned events, including smearing to account for the detector. With a large enough number of events, one can find the extremum of log likelihood (see, e.g., Ref. [109]), but for POEMMA's total ∼1, 400

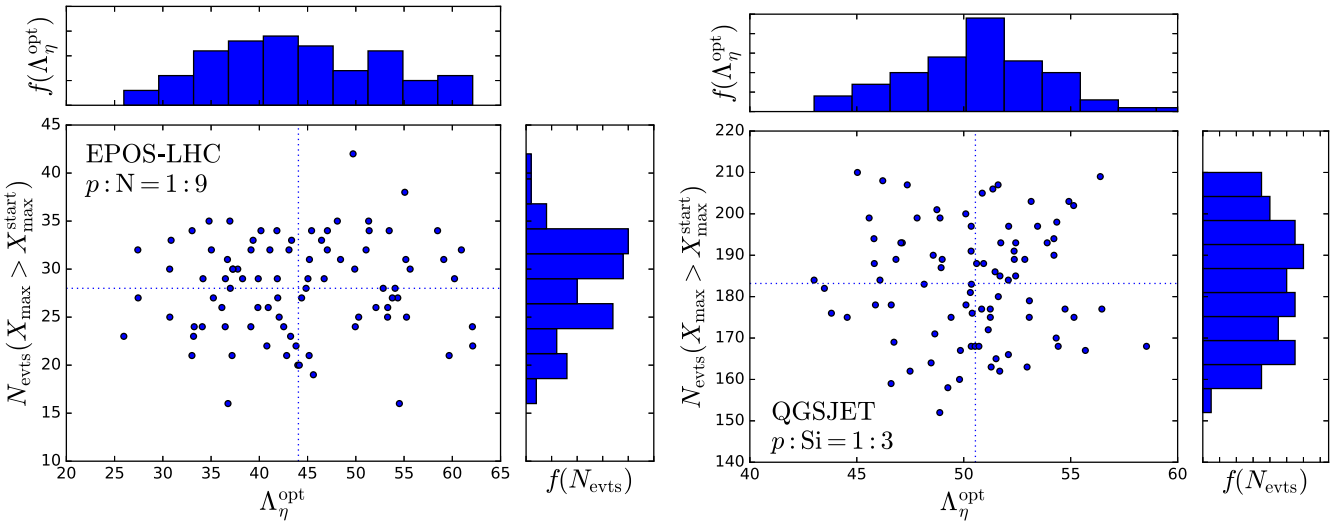

FIG. 39. Values of $\Lambda_\eta^{\mathrm{opt}}$ and the number of events for $E_{\mathrm{CR}} > 40$ EeV and $X_{\mathrm{max}} > X_{\mathrm{max}}^{\mathrm{start}}$ for $p:N = 1:9$, $\eta = 0.02$ with EPOS-LHC (left) and $p:\mathrm{Si} = 1:3$, $\eta = 0.13$ with QGSJET (right). The blue histograms show the frequencies of $\Lambda_\eta^{\mathrm{opt}}$ and $N_{\mathrm{evts}}(X_{\mathrm{max}} > X_{\mathrm{max}}^{\mathrm{start}})$. The vertical and horizontal dotted lines show the mean values of $\Lambda_\eta^{\mathrm{opt}}$ and $N_{\mathrm{evts}}(X_{\mathrm{max}} > X_{\mathrm{max}}^{\mathrm{start}})$, respectively.

cosmic ray events above 40 EeV, a reasonable approximation is

$$\Lambda_\eta^{\mathrm{opt}} = \sum_{i=1,N_{\mathrm{evts}}} (X_{\mathrm{max},i} - X_{\mathrm{max}}^{\mathrm{start}})/N_{\mathrm{evts}}. \tag{C1}$$

With a high statistics Monte Carlo, we generate events according to a cosmic-ray spectrum above the ankle parametrized by

$$J(E) = J_0 \left(\frac{E}{E_{\mathrm{ankle}}}\right)^{-\gamma_2} \left[1 + \left(\frac{E_{\mathrm{ankle}}}{E_s}\right)^{\Delta\gamma}\right] \times \left[1 + \left(\frac{E}{E_s}\right)^{\Delta\gamma}\right]^{-1}, \tag{C2}$$

where we take the central values of $E_{\mathrm{ankle}} = 5.08$ EeV, $E_s = 39$ EeV, $\gamma_2 = 2.53$, $\Delta\gamma = 2.5$ as measured by the Auger Collaboration and reported in Ref. [157]. We model the X_{max} distribution with the generalized Gumbel form with parameters determined in Ref. [158] for the QGSJETII.04 [159] and EPOS-LHC [160] shower models. The cosmic-ray energies are smeared according to

$$\ln(E/E_{\mathrm{norm}}) = \ln(E_0/E_{\mathrm{norm}}) + \Delta \tag{C3}$$

for $E_{\mathrm{norm}} = 10^{18}$ eV, with Δ generated with a Gaussian distribution with $\sigma_\Delta = 0.2$. The X_{max} values are smeared with a Gaussian distribution with $\sigma_X = 35$ g/cm^2. For the QGSJETII.04 (EPOS-LHC) model, $X_{\mathrm{max}}^{\mathrm{start}} = 896(906)$ g/cm^2 for the cosmic-ray composition of $p:N = 1:9$ and $\eta = 0.02$. We find $X_{\mathrm{max}}^{\mathrm{start}} = 834(851)$ g/cm^2 for $p:\mathrm{Si} = 1:3$ with the QGSJETII.04 (EPOS-LHC) model with $\eta = 0.13$. Examples of ~80–90 Monte Carlo trials of the 1,400 events POEMMA will measure with smeared energy above 40 EeV and $X_{\mathrm{max}} > X_{\mathrm{max}}^{\mathrm{start}}$ are shown in Fig. 39.

Figure 40 shows the smeared, high statistics histograms of the unit normalized X_{max} distributions of all cosmic rays above 40 EeV (blue histograms) and the proton component (green histograms). The X_{max} distributions for one sample of $N_{\mathrm{evts}} = 1,400$ for two composition models and a hadronic interaction model are shown with the data points in the panels in Fig. 40. The error bars show $\sqrt{N_i}/N_{\mathrm{evts}}/\Delta X_{\mathrm{max}}$ for $\Delta X_{\mathrm{max}} = 10$ g/cm^2 for this set of 1,400 events. The red points show the X_{max} bins which are above the bin that includes $X_{\mathrm{max}}^{\mathrm{start}}$. In the right panels, the shaded red bands show the range of slopes of the tail determined by $\Lambda_\eta^{\mathrm{opt}}$ with 1σ statistical errors on both $\Lambda_\eta^{\mathrm{opt}}$ and the number of events above $X_{\mathrm{max}}^{\mathrm{start}}$, given 1,400 total events for POEMMA. Thus, $\Lambda_\eta^{\mathrm{opt}}$ can be converted to $\sigma_{p\text{-air}}$ with the associated statistical uncertainty shown in Fig. 26.

APPENDIX D: POEMMA's SIMULATED UHE NEUTRINO SENSITIVITY

In stereo observation mode, POEMMA monitors ~10^{13} metric tons of atmosphere. Thus, POEMMA has high sensitivity via air fluorescence EAS observations for UHE neutrino interactions that occur deep in the atmosphere that are well separated from UHECR EASs. The POEMMA stereo simulation package was used to simulate neutrino interactions above 30 EeV assuming an isotropic flux. For neutrino energies above a PeV, the neutrino and antineutrino interaction cross sections are virtually equal, and we just denote these as neutrinos. For neutrino energies above 10 EeV, the y-dependence of the cross section puts, on average, 80% of the neutrino energy into the daughter

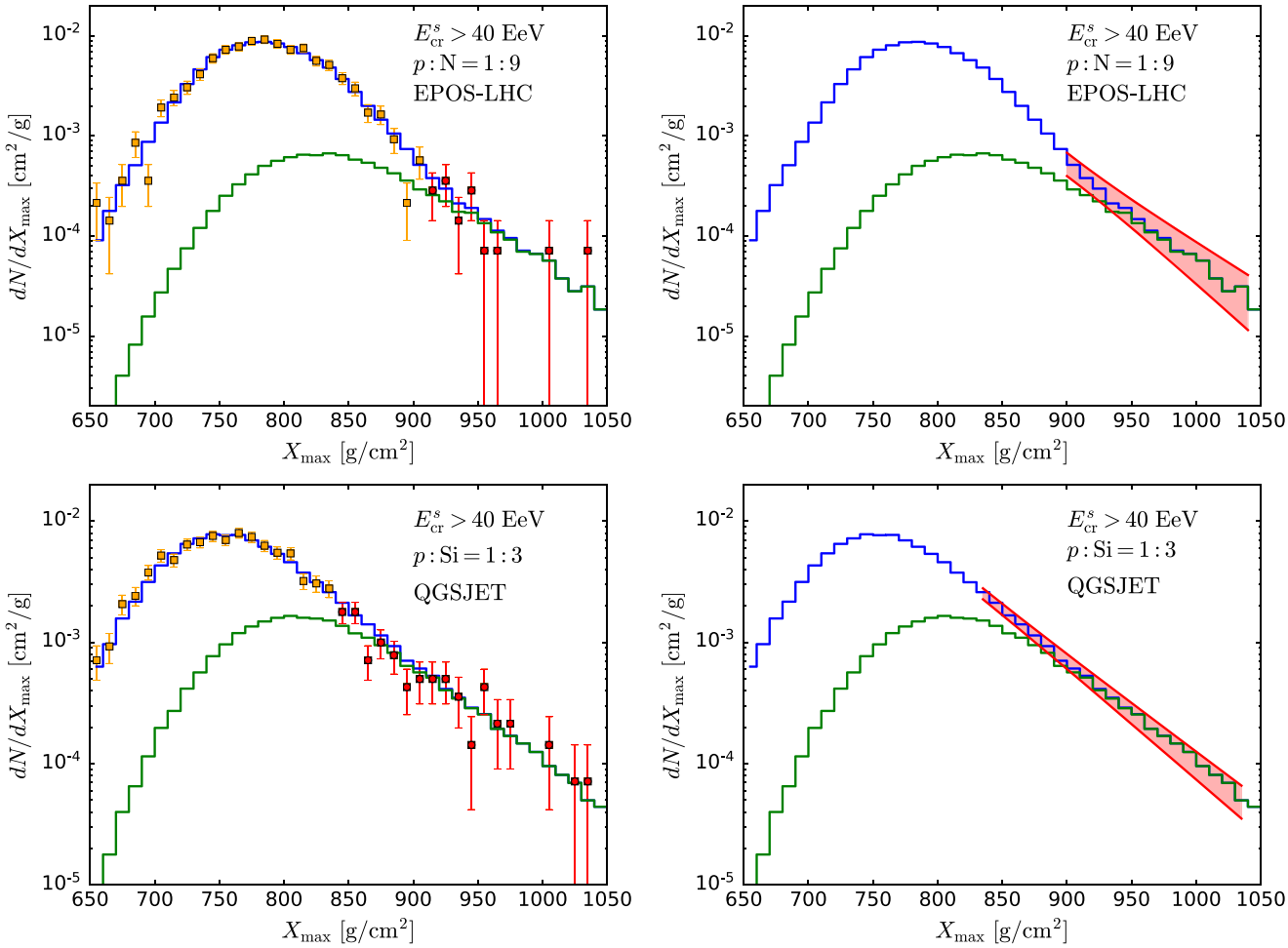

FIG. 40. The energy and $X_{\rm max}$ smeared distribution $\mathrm{d}N/\mathrm{d}X_{\rm max}$ for QGS JETII.04 (upper panels) and EPOS-LHC (lower panels) from the parametrization of Ref. [158] for $E_{\rm CR} > 40$ EeV and $p\!:\!N = 1\!:\!9$, $\eta = 0.02$ (upper) and $p\!:\!{\rm Si} = 1\!:\!3$, $\eta = 0.13$ (lower). The blue histograms show the full $X_{\rm max}$ distributions, while the green histograms show the proton components. The data points, with error bars, show the distribution of events for one sample of $N_{\rm evts} = 1,400$ events with error bars according to $\sqrt{N_i}/N_{\rm evts}$, for N_i being the number of events in the bin i. The red data points show $X_{\rm max}$ bins above $X^{\rm start}_{\rm max}$. In the right panels, the shaded red band shows the slope of the tail determined by $\Lambda^{\rm opt}_\eta$ with 1σ statistical errors on $\Lambda^{\rm opt}_\eta$ and the number of events above $X^{\rm start}_{\rm max}$.

lepton and 20% into a hadronic shower. For charged-current (CC) electron neutrino interactions this leads to an EAS with 100% of the neutrino energy. The EAS development is simulated as that of a proton, but initiated at the neutrino interaction point. On one hand this is conservative since a pure electromagnetic EAS will have ∼20% higher $N_{\rm part}$ at EAS maximum, but on the other hand, the Landau–Pomeranchuk–Migdal effect [161,162] will reduce this. Given this, proton EAS profiles are used since a model of the LPM effect is included in the EAS generator. The selection of $X_{\rm Start} \geq 2000$ g/cm^2 is based on the analysis of the $X_{\rm Start}$ distributions for UHECR protons at 40, 60, 100, and 200 EeV. The event selection is based on the stereo selection described earlier, which yields approximately 1° angular resolution which implies a 1.5×10^{-4} fractional error on the determination of $X_{\rm Start}$. Figure 41 shows the distribution of $X_{\rm Start}$ for UHECRS along with parametric fits used to define the quasi-Gaussian peaks and exponential tails of the distributions. These parametric fits define probability distributions that can be evaluated to determine the probability for $X_{\rm Start} \geq 2000$ g/cm^2 and $X_{\rm Start} \geq 1500$ g/cm^2; the latter is used for comparison to the effects on the neutrino aperture for different selection criteria. Table VII provides the UHECR background probabilities as a function of $X_{\rm Start}$ and EAS energies. Note that the assumption that the UHECR flux is pure protons is the most conservative assumption for this background analysis. Table VII also provides the anticipated statistics in representative energy ranges based on the Auger and TA spectra assuming 5 years of observation as shown in Fig. 18 for stereo (nadir) observations.

Using the background probabilities and anticipated UHECR event statistics, the mean number of background

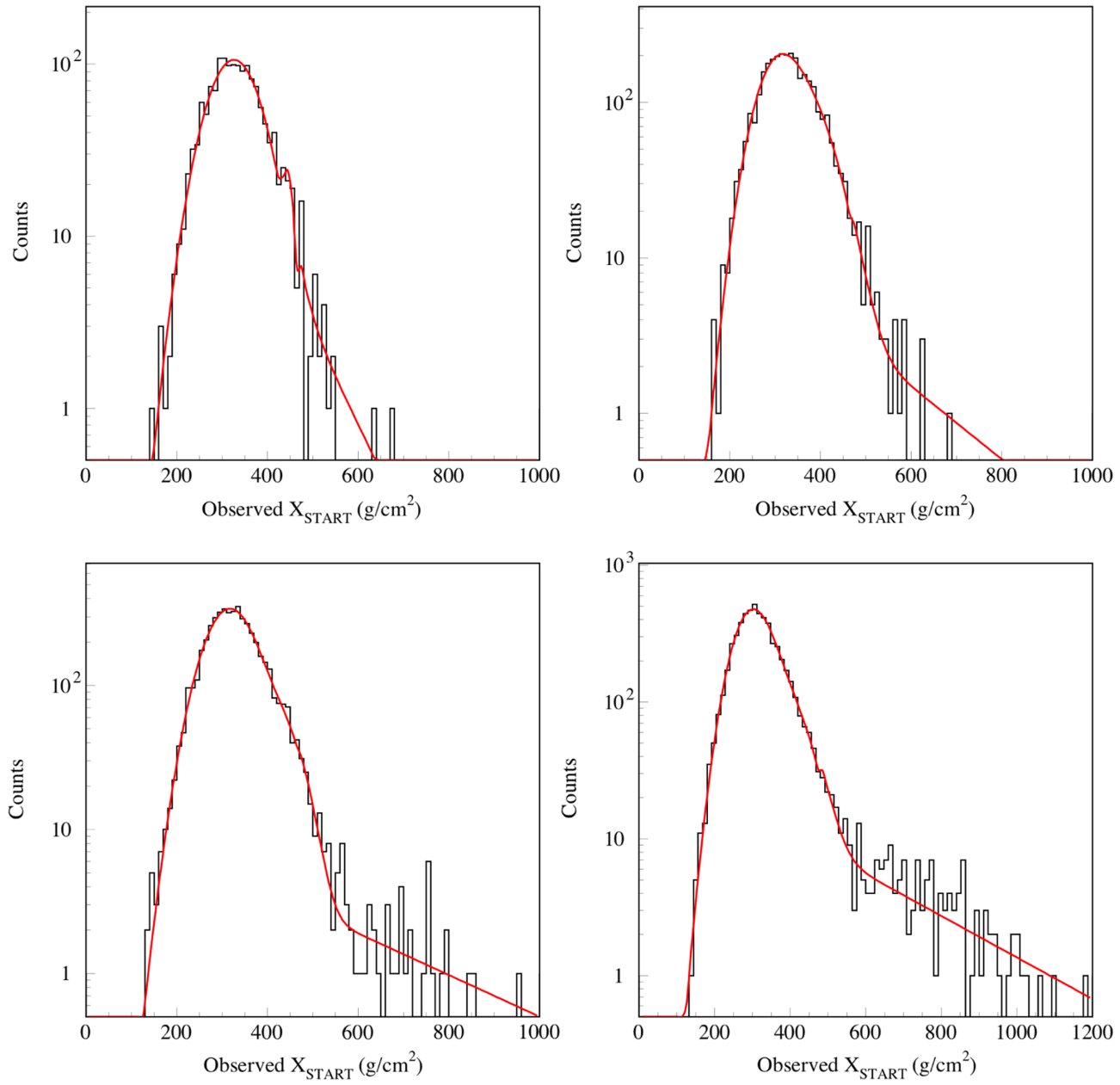

FIG. 41. The X_{Start} distributions defined by the observed starting point of proton EASs and a parametric fit using two Gaussian and an exponential distribution. Top left: 40 EeV (fit reduced $\chi^2 = 1.13$); Top right: 60 EeV (fit reduced $\chi^2 = 1.34$); bottom left: 100 EeV (fit reduced $\chi^2 = 0.95$); bottom right: (fit reduced $\chi^2 = 0.85$).

TABLE VII. UHECR proton background probabilities as a function of energy and X_{Start} as well as the anticipated UHECR statistics in representative energy ranges based on 5-year observation with the Auger and TA measured spectra.

X_{Start}	40 EeV	60 EeV	100 EeV	200 EeV
$\geq$1500 g/cm^2	4.9×10^{-8}	7.2×10^{-5}	5.8×10^{-4}	9.1×10^{-4}
$\geq$2000 g/cm^2	9.0×10^{-11}	4.8×10^{-6}	1.1×10^{-4}	2.1×10^{-4}
Spectrum	$E_{\mathrm{prot}} < 50$ EeV	50 EeV $\leq E_{\mathrm{prot}} <$ 100 EeV	100 EeV $\leq E_{\mathrm{prot}} <$ 200 EeV	$E_{\mathrm{prot}} \geq 200$ EeV
Auger (5 years)	3106	271	66	5
TA (5 Years)	5006	925	327	10

TABLE VIII. UHECR observed proton background probabilities as a function of energy and $X_{\rm Start}$ based on 5-year observation with the Auger and TA measured spectra.

$X_{\rm Start}$	40 EeV	60 EeV	100 EeV	200 EeV	Sum
Auger spectrum: $N_{\rm Obs} \geq 1$					
$\geq 1500 {\rm g/cm}^2$	1.5×10^{-4}	1.9×10^{-2}	3.8×10^{-2}	4.5×10^{-3}	6.1×10^{-2}
$\geq 2000 {\rm g/cm}^2$	2.8×10^{-7}	1.3×10^{-3}	7.2×10^{-3}	1.0×10^{-3}	9.6×10^{-3}
Auger spectrum: $N_{\rm Obs} \geq 2$					
$\geq 1500 {\rm g/cm}^2$	1.2×10^{-8}	1.9×10^{-4}	7.1×10^{-4}	1.0×10^{-5}	9.1×10^{-4}
$\geq 2000 {\rm g/cm}^2$	3.9×10^{-14}	8.4×10^{-7}	2.6×10^{-5}	5.3×10^{-7}	2.8×10^{-5}
TA spectrum: $N_{\rm Obs} \geq 1$					
$\geq 1500 {\rm g/cm}^2$	2.5×10^{-4}	6.4×10^{-2}	1.7×10^{-1}	9.0×10^{-3}	2.5×10^{-1}
$\geq 2000 {\rm g/cm}^2$	4.7×10^{-7}	4.4×10^{-3}	3.5×10^{-2}	2.1×10^{-3}	4.2×10^{-2}
Ta spectrum: $N_{\rm Obs} \geq 2$					
$\geq 1500 {\rm g/cm}^2$	3.0×10^{-8}	2.1×10^{-3}	1.6×10^{-2}	4.1×10^{-5}	1.8×10^{-2}
$\geq 2000 {\rm g/cm}^2$	1.0×10^{-13}	9.8×10^{-6}	6.3×10^{-4}	2.1×10^{-6}	6.4×10^{-4}

events can be calculated and evaluated assuming Poisson statistics to calculate the probability of observing ≥ 1 and ≥ 2 UHECR background events with POEMMA in 5 years. These are also detailed in Table VIII.

The results show that assuming the POEMMA UHECR statistics based on the measured Auger UHECR spectrum, the probability of getting at least one UHECR background event in the neutrino sample is 6.1% for $X_{\rm Start} \geq 1500$ g/cm^2 while it is $< 1\%$ for $X_{\rm Start} \geq 2000$ g/cm^2. Assuming the POEMMA UHECR statistics based on the measured TA UHECR spectrum, the probability of getting at lease one UHECR background event in the neutrino sample is 25% for $X_{\rm Start} \geq 1500$ g/cm^2 while it is 4.2% for $X_{\rm Start} \geq 2000$ g/cm^2. This motivates the use of $X_{\rm Start} \geq 2000$ g/cm^2 for the POEMMA air fluorescence neutrino acceptance.

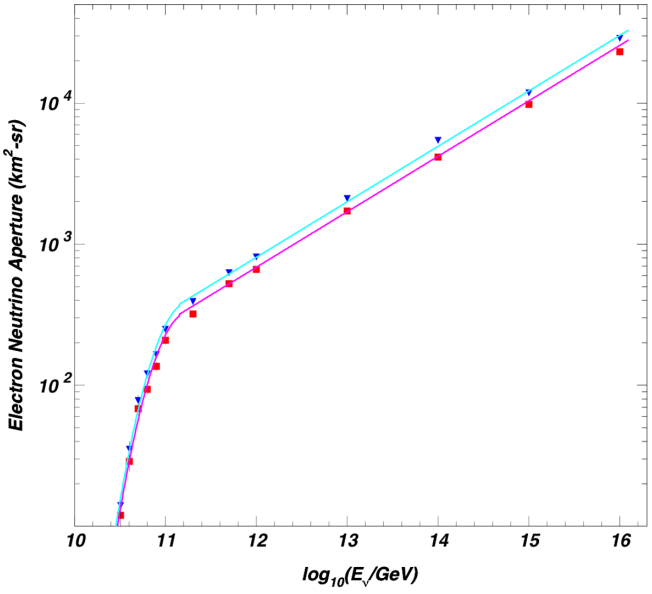

FIG. 42. Comparison of the instantaneous electron neutrino apertures based on stereo air fluorescence measurements. Upper points and curve are for $X_{\rm Start} \geq 1500$ g/cm^2 while the lower points and curve are for $X_{\rm Start} \geq 2000$ g/cm^2. The lower curve is 85% of the upper curve over the energy band.

The effects of the $X_{\rm Start}$ selection on the simulated electron neutrino aperture is shown in Fig. 42. A parametric fit is used to describe the aperture based on simulations at specific energies. The comparison of the results for $X_{\rm Start} \geq 2000$ g/cm^2 shows a modest 15% reduction over the entire energy band as compared to the $X_{\rm Start} \geq 1500$ g/cm^2 results. This comparison shows the relative insensitivity of the electron neutrino aperture for modest changes in the observed $X_{\rm Start}$ requirement.

Using the CC electron neutrino aperture, the apertures of the other neutrino flavors for both CC and NC can be obtained. For the NC, the emergent lepton is a neutrino and thus an EAS with 20% of the incident neutrino energy is produced but with a lower rate given by the ratio of NC to CC neutrino cross sections. Effectively this shifts the NC neutrino aperture curve up by a factor of 5 in neutrino energy, compared to the CC electron neutrino aperture, with a reduction given by $\frac{\sigma_{\rm NC}(E_\nu)}{\sigma_{\rm CC}(E_\nu)}$ for each of the three neutrino flavors. For the CC μ_μ and ν_τ apertures, we conservatively assume that only 20% of the neutrino energy is observed; e.g., the EAS generated by the emergent muon or τ lepton is not observed. While these UHE muons are well above their critical energy, the charged-particle production in these muonic EASs versus electron-initiated EAS is much reduced [163]. Thus it is assumed that the air fluorescence signal is below POEMMA's detection threshold. For τ-leptons, the decay length given by $\gamma c\tau$ is nearly 5,000 km at 100 EeV. The conservative approach is to assume the τ lepton decays outside POEMMA's FoV and

only 20% of the incident neutrino is observed in the EAS. These assumptions lead to the muon and τ-lepton CC neutrino apertures shifted up by a factor of 5 in neutrino energy, compared to the CC electron neutrino aperture. The ensemble of these results are presented in the rightmost plot in Fig. 28.

[1] P. Auger, P. Ehrenfest, R. Maze, J. Daudin, and A. F. Robley, Extensive cosmic ray showers, Rev. Mod. Phys. **11**, 288 (1939).

[2] K. Kotera and A. V. Olinto, The astrophysics of ultrahigh energy cosmic rays, Annu. Rev. Astron. Astrophys. **49**, 119 (2011).

[3] L. A. Anchordoqui, ultrahigh-energy cosmic rays, Phys. Rep. **801**, 1 (2019).

[4] R. A. Batista *et al.*, Open questions in cosmic-ray research at ultrahigh energies, Front. Astron. Space Sci. **6**, 23 (2019).

[5] J. Abraham *et al.* (Pierre Auger Collaboration), Trigger and aperture of the surface detector array of the Pierre Auger Observatory, Nucl. Instrum. Methods Phys. Res., Sect. A **613**, 29 (2010).

[6] J. Abraham *et al.* (Pierre Auger Collaboration), The fluorescence detector of the Pierre Auger Observatory, Nucl. Instrum. Methods Phys. Res., Sect. A **620**, 227 (2010).

[7] J. Aab *et al.* (Pierre Auger Collaboration), The Pierre Auger Observatory: Contributions to the 35th International Cosmic Ray Conference (ICRC 2017), arXiv:1708.06592.

[8] T. Abu-Zayyad *et al.*, The surface detector array of the Telescope Array experiment, Nucl. Instrum. Methods Phys. Res., Sect. A **689**, 87 (2012).

[9] H. Tokuno *et al.*, New air fluorescence detectors employed in the Telescope Array experiment, Nucl. Instrum. Methods Phys. Res., Sect. A **676**, 54 (2012).

[10] R. U. Abbasi *et al.* (HiRes Collaboration), First Observation of the Greisen-Zatsepin-Kuzmin Suppression, Phys. Rev. Lett. **100**, 101101 (2008).

[11] J. Abraham *et al.* (Pierre Auger Collaboration), Observation of the Suppression of the Flux of Cosmic Rays above 4×10^{19} eV, Phys. Rev. Lett. **101**, 061101 (2008).

[12] J. Abraham *et al.* (Pierre Auger Collaboration), Measurement of the energy spectrum of cosmic rays above 10^{18} eV using the Pierre Auger Observatory, Phys. Lett. B **685**, 239 (2010).

[13] T. Abu-Zayyad *et al.* (Telescope Array Collaboration), The cosmic ray energy spectrum observed with the surface detector of the Telescope Array experiment, Astrophys. J. **768**, L1 (2013).

[14] T. Array (Telescope Array and Pierre Auger Collaborations), Pierre Auger Observatory and Telescope Array: Joint Contributions to the 35th International Cosmic Ray Conference (ICRC 2017), arXiv:1801.01018.

[15] J. Linsley, Structure of large air showers at depth 834 G/sq.cm. 3. Applications, Izv. Fiz. Inst. Bulg. Akad. Nauk. **12**, 56 (1978).

[16] J. Linsley and A. A. Watson, Validity of Scaling to 10^{20} eV and High-Energy Cosmic Ray Composition, Phys. Rev. Lett. **46**, 459 (1981).

[17] R. U. Abbasi *et al.*, Study of ultrahigh energy cosmic ray composition using telescope array's middle drum detector and surface array in hybrid mode, Astropart. Phys. **64**, 49 (2015).

[18] R. U. Abbasi *et al.* (Telescope Array Collaboration), Depth of ultra high energy cosmic ray induced air shower maxima measured by the Telescope Array black rock and long ridge FADC fluorescence detectors and surface array in hybrid mode, Astrophys. J. **858**, 76 (2018).

[19] J. Abraham *et al.* (Pierre Auger Collaboration), Measurement of the Depth of Maximum of Extensive Air Showers above 10^{18} eV, Phys. Rev. Lett. **104**, 091101 (2010).

[20] A. Aab *et al.* (Pierre Auger Collaboration), Depth of maximum of air-shower profiles at the Pierre Auger Observatory. I. Measurements at energies above $10^{17.8}$ eV, Phys. Rev. D **90**, 122005 (2014).

[21] A. Aab *et al.* (Pierre Auger Collaboration), Depth of maximum of air-shower profiles at the Pierre Auger Observatory. II. Composition implications, Phys. Rev. D **90**, 122006 (2014).

[22] A. Aab *et al.* (Pierre Auger Collaboration), Inferences on mass composition and tests of hadronic interactions from 0.3 to 100 EeV using the water-Cherenkov detectors of the Pierre Auger Observatory, Phys. Rev. D **96**, 122003 (2017).

[23] R. Abbasi *et al.* (Pierre Auger and Telescope Array Collaborations), Report of the working group on the composition of ultra high energy cosmic rays, J. Phys. Soc. Jpn. Conf. Proc. **9**, 010016 (2016).

[24] W. Hanlon, J. Bellido, J. Belz, S. Blaess, V. de Souza, D. Ikeda, P. Sokolsky, Y. Tsunesada, M. Unger, and A. Yushkov, Report of the working group on the mass composition of ultrahigh energy cosmic rays, J. Phys. Soc. Jpn. Conf. Proc. **19**, 011013 (2018).

[25] A. Aab *et al.* (Pierre Auger Collaboration), Evidence for a mixed mass composition at the 'ankle' in the cosmic-ray spectrum, Phys. Lett. B **762**, 288 (2016).

[26] M. S. Pshirkov, P. G. Tinyakov, and F. R. Urban, New Limits on Extragalactic Magnetic Fields from Rotation Measures, Phys. Rev. Lett. **116**, 191302 (2016).

[27] E. Waxman and J. Miralda-Escude, Images of bursting sources of high-energy cosmic rays. 1. Effects of magnetic fields, Astrophys. J. **472**, L89 (1996).

[28] G. R. Farrar, R. Jansson, I. J. Feain, and B. M. Gaensler, Galactic magnetic deflections and Centaurus A as a UHECR source, J. Cosmol. Astropart. Phys. 01 (2013) 023.

[29] G. R. Farrar and M. S. Sutherland, Deflections of UHECRs in the Galactic magnetic field, J. Cosmol. Astropart. Phys. 05 (2019) 004.

[30] K. Greisen, End to the Cosmic Ray Spectrum?, Phys. Rev. Lett. **16**, 748 (1966).

[31] G. T. Zatsepin and V. A. Kuzmin, Upper limit of the spectrum of cosmic rays, Pis'ma Zh. Eksp. Teor. Fiz. **4**, 114 (1966) [JETP Lett. **4**, 78 (1966)].

[32] A. Aab *et al.* (Pierre Auger Collaboration), Observation of a large-scale anisotropy in the arrival directions of cosmic rays above 8×10^{18} eV, Science **357**, 1266 (2017).

[33] A. Aab *et al.* (Pierre Auger Collaboration), Large-scale cosmic-ray anisotropies above 4 EeV measured by the Pierre Auger Observatory, Astrophys. J. **868**, 4 (2018).

[34] R. U. Abbasi *et al.* (Telescope Array Collaboration), Indications of intermediate-scale anisotropy of cosmic rays with energy greater than 57 EeV in the Northern Sky measured with the surface detector of the Telescope Array experiment, Astrophys. J. **790**, L21 (2014).

[35] A. Aab *et al.* (Pierre Auger Collaboration), An indication of anisotropy in arrival directions of ultrahigh-energy cosmic rays through comparison to the flux pattern of extragalactic gamma-ray sources, Astrophys. J. **853**, L29 (2018).

[36] R. U. Abbasi *et al.* (Telescope Array Collaboration), Testing a reported correlation between arrival directions of ultrahigh-energy cosmic rays and a flux pattern from nearby Starburst Galaxies using Telescope Array data, Astrophys. J. **867**, L27 (2018).

[37] P. Blasi, R. I. Epstein, and A. V. Olinto, Ultrahigh-energy cosmic rays from young neutron star winds, Astrophys. J. **533**, L123 (2000).

[38] K. Fang, K. Kotera, and A. V. Olinto, Newly-born pulsars as sources of ultrahigh energy cosmic rays, Astrophys. J. **750**, 118 (2012).

[39] K. Fang, K. Kotera, and A. V. Olinto, Ultrahigh energy cosmic ray nuclei from extragalactic pulsars and the effect of their Galactic counterparts, J. Cosmol. Astropart. Phys. 03 (2013) 010.

[40] P. L. Biermann and P. A. Strittmatter, Synchrotron emission from shock waves in active galactic nuclei, Astrophys. J. **322**, 643 (1987).

[41] J. P. Rachen and P. L. Biermann, Extragalactic ultrahigh-energy cosmic rays. 1. Contribution from hot spots in FR-II radio galaxies, Astron. Astrophys. **272**, 161 (1993).

[42] G. E. Romero, J. A. Combi, L. A. Anchordoqui, and S. P. Bergliaffa, A possible source of extragalactic cosmic rays with arrival energies beyond the GZK cutoff, Astropart. Phys. **5**, 279 (1996).

[43] J. H. Matthews, A. R. Bell, K. M. Blundell, and A. T. Araudo, Fornax A, Centaurus A, and other radio galaxies as sources of ultrahigh energy cosmic rays, Mon. Not. R. Astron. Soc. **479**, L76 (2018).

[44] L. A. Anchordoqui, G. E. Romero, and J. A. Combi, Heavy nuclei at the end of the cosmic ray spectrum?, Phys. Rev. D **60**, 103001 (1999).

[45] L. A. Anchordoqui, Acceleration of ultrahigh-energy cosmic rays in starburst superwinds, Phys. Rev. D **97**, 063010 (2018).

[46] L. A. Anchordoqui and J. F. Soriano, Evidence for UHECR origin in starburst galaxies, Proc. Sci., ICRC2019 (**2019**) 255.

[47] E. Waxman, Cosmological Gamma-Ray Bursts and the Highest Energy Cosmic Rays, Phys. Rev. Lett. **75**, 386 (1995).

[48] M. Vietri, On the acceleration of ultrahigh-energy cosmic rays in gamma-ray bursts, Astrophys. J. **453**, 883 (1995).

[49] C. D. Dermer and A. Atoyan, Ultrahigh energy cosmic rays, cascade gamma-rays, and high-energy neutrinos from gamma-ray bursts, New J. Phys. **8**, 122 (2006).

[50] X.-Y. Wang, S. Razzaque, and P. Meszaros, On the origin and survival of UHE cosmic-ray nuclei in GRBs and Hypernovae, Astrophys. J. **677**, 432 (2008).

[51] K. Murase, K. Ioka, S. Nagataki, and T. Nakamura, High-energy cosmic-ray nuclei from high- and low-luminosity gamma-ray bursts and implications for multimessenger astronomy, Phys. Rev. D **78**, 023005 (2008).

[52] P. Baerwald, M. Bustamante, and W. Winter, UHECR escape mechanisms for protons and neutrons from GRBs, and the cosmic ray-neutrino connection, Astrophys. J. **768**, 186 (2013).

[53] N. Globus, D. Allard, R. Mochkovitch, and E. Parizot, UHECR acceleration at GRB internal shocks, Mon. Not. R. Astron. Soc. **451**, 751 (2015).

[54] B. T. Zhang, K. Murase, S. S. Kimura, S. Horiuchi, and P. Mészáros, Low-luminosity gamma-ray bursts as the sources of ultrahigh-energy cosmic ray nuclei, Phys. Rev. D **97**, 083010 (2018).

[55] A. V. Olinto *et al.*, POEMMA: Probe of extreme multi-messenger astrophysics, Proc. Sci., ICRC2017 (**2018**) 542.

[56] E. Kido, Status and prospects of the TAx4 experiment, EPJ Web Conf. **210**, 06001 (2019).

[57] A. Aab *et al.* (Pierre Auger Collaboration), The Pierre Auger Observatory Upgrade–Preliminary Design Report, arXiv:1604.03637.

[58] F. W. Stecker, J. F. Krizmanic, L. M. Barbier, E. Loh, J. W. Mitchell, P. Sokolsky, and R. E. Streitmatter, Observing the ultrahigh-energy universe with OWL eyes, Nucl. Phys. B, Proc. Suppl. **136C**, 433 (2004).

[59] J. H. Adams *et al.* (JEM-EUSO Collaboration), An evaluation of the exposure in nadir observation of the JEM-EUSO mission, Astropart. Phys. **44**, 76 (2013).

[60] A. Neronov, D. V. Semikoz, L. A. Anchordoqui, J. Adams, and A. V. Olinto, Sensitivity of a proposed space-based Cherenkov astrophysical-neutrino telescope, Phys. Rev. D **95**, 023004 (2017).

[61] For details, see https://idc.nasa.gov/idc/.

[62] G. Abdellaoui *et al.*, ultraviolet imaging of the night-time earth by EUSO-Balloon towards space-based ultrahigh energy cosmic ray observations, Astropart. Phys. **111**, 54 (2019).

[63] L. Wiencke and A. Olinto (JEM-EUSO Collaboration), EUSO-SPB1 Mission and Science, Proc. Sci., ICRC2017 (**2018**) 1097.

[64] L. Wiencke and A. Olinto (JEM-EUSO and POEMMA Collaboration), The extreme Universe space observatory on a superpressure Balloon II mission, Proc. Sci., ICRC2019 (**2019**) 466.

[65] A. Belov, M. Bertaina, F. Capel, F. Fausti, F. Fenu, P. Klimov, M. Mignone, and H. Miyamoto (JEM-EUSO

Collaboration), The integration and testing of the Mini-EUSO multilevel trigger system, Adv. Space Res. **62**, 2966 (2018).
[66] O. Adriani, Y. Akaike, K. Asano, Y. Asaoka, M. G. Bagliesi, G. Bigongiari, W. R. Binns, S. Bonechi, M. Bongi, and J. H. Buckley, The CALorimetric Electron Telescope (CALET) for high-energy astroparticle physics on the International Space Station, in J. Phys. Conf. Ser. **632**, 012023 (2015).
[67] T. M. Venters, M. H. Reno, J. F. Krizmanic, L. A. Anchordoqui, C. Guépin, and A. V. Olinto, POEMMA's target of opportunity sensitivity to cosmic neutrino transient sources, arXiv:1906.07209.
[68] https://www.zemax.com/products/opticstudio.
[69] P. T. Mikulski, Extensive air showers: Model dependence and the longitudinal profile. Ph.D. thesis, Johns Hopkins University, 2000.
[70] T. K. Gaisser and A. M. Hillas, Reliability of the method of constant intensity cuts for reconstructing the average development of vertical showers, in *Proceedings of the 15th ICRC (Plovdiv)* (1977), Vol. 8, pp. 353–357.
[71] T. Pierog, M. K. Alekseeva, T. Bergmann, V. Chernatkin, R. Engel, D. Heck, N. N. Kalmykov, J. Moyon, S. Ostapchenko, T. Thouw, and K. Werner, First results of fast one-dimensional hybrid simulation of EAS using CONEX, Nucl. Phys. B, Proc. Suppl. **151**, 159 (2006).
[72] T. K. Gaisser, *Cosmic Rays and Particle Physics* (Cambridge University Press, Cambridge, England, 1990), p. 34.
[73] A. M. Hillas, The sensitivity of Cerenkov radiation pulses to the longitudinal development of cosmic-ray showers, J. Phys. G **8**, 1475 (1982).
[74] A. N. Bunner, Ph.D. Thesis, Cornell-Sydney Univ. Astron. Center. Tech Report. No. 62, 1966.
[75] G. Davidson and R. O'Neil, Optical radiation from nitrogen and air at high pressure excited by energetic electrons, J. Chem. Phys. **41**, 3964 (1964).
[76] M. Tanabashi *et al.* (Particle Data Group), Review of particle physics, Phys. Rev. D **98**, 030001 (2018).
[77] F. Kakimoto, E. C. Loh, M. Nagano, H. Okuno, M. Teshima, and S. Ueno, A measurement of the air fluorescence yield, Nucl. Instrum. Methods Phys. Res., Sect. A **372**, 527 (1996).
[78] R. C. Fernow, *Introduction to Experimental Particle Physics* (Cambridge University Press, Cambridge, 1986), pp. 178–183.
[79] P. Sokolsky, *Introduction of Ultrahigh Energy Cosmic Ray Physics* (Addison-Wesley, Reading, MA, 1989), pp. 200–201.
[80] J. F. Krizmanic, Performance of the orbiting wide-angle light collector (OWL/AirWatch) experiment via Monte Carlo simulation, in *Proceedings of the 26th ICRC (Salt Lake City)* (1999), Vol. 2, pp. 388–391.
[81] R. D. McPeters *et al.*, Nimbus-7 Total Ozone Mapping Spectrometer (TOMS) data products user's guide, NASA Tech. Report No. NASA-RP-1384, 1996.
[82] G. K. Garipov, B. A. Khrenov, M. I. Panasyuk, V. I. Tulupov, A. V. Shirokov, I. V. Yashin, and H. Salazar, UV radiation from the atmosphere: Results of the MSU "Tatiana" satellite measurements, Astropart. Phys. **24**, 400 (2005).
[83] J. H. Adams *et al.* (JEM-EUSO Collaboration), The JEM-EUSO observation in cloudy conditions, Exp. Astron. **40**, 135 (2015).
[84] J. Matthews (Telescope Array Collaboration), Highlights from the Telescope Array experiment, Proc. Sci., ICRC2017 (**2018**) 1096.
[85] M. Ahlers, L. A. Anchordoqui, and A. M. Taylor, Ensemble fluctuations of the flux and nuclear composition of ultrahigh energy cosmic ray nuclei, Phys. Rev. D **87**, 023004 (2013).
[86] M. S. Muzio, M. Unger, and G. R. Farrar, Progress towards characterizing ultrahigh energy cosmic ray sources, Phys. Rev. D **100**, 103008 (2019).
[87] D. Allard, N. G. Busca, G. Decerprit, A. V. Olinto, and E. Parizot, Implications of the cosmic ray spectrum for the mass composition at the highest energies, J. Cosmol. Astropart. Phys. 10 (2008) 033.
[88] G. J. Feldman and R. D. Cousins, A Unified approach to the classical statistical analysis of small signals, Phys. Rev. D **57**, 3873 (1998).
[89] M. Unger, G. R. Farrar, and L. A. Anchordoqui, Origin of the ankle in the ultrahigh energy cosmic ray spectrum, and of the extragalactic protons below it, Phys. Rev. D **92**, 123001 (2015).
[90] M. G. Aartsen *et al.* (IceCube Collaboration), Constraints on Ultrahigh-Energy Cosmic-Ray Sources from a Search for Neutrinos above 10 PeV with IceCube, Phys. Rev. Lett. **117**, 241101 (2016); Erratum, Phys. Rev. Lett. **119**, 259902 (2017).
[91] P. W. Gorham *et al.* (ANITA Collaboration), Constraints on the ultrahigh-energy cosmic neutrino flux from the fourth flight of ANITA, Phys. Rev. D **99**, 122001 (2019).
[92] M. Ackermann *et al.* (Fermi-LAT Collaboration), Resolving the Extragalactic γ-Ray Background above 50 GeV with the Fermi Large Area Telescope, Phys. Rev. Lett. **116**, 151105 (2016).
[93] K.-H. Kampert and M. Unger, Measurements of the cosmic ray composition with air shower experiments, Astropart. Phys. **35**, 660 (2012).
[94] M. Risse and P. Homola, Search for ultrahigh energy photons using air showers, Mod. Phys. Lett. A **22**, 749 (2007).
[95] J. Krizmanic, D. Bergman, and P. Sokolsky, The modeling of the nuclear composition measurement performance of the nonImaging CHErenkov Array (NICHE), arXiv:1307.3918.
[96] L. A. Anchordoqui, V. Barger, and T. J. Weiler, Cosmic mass spectrometer, J. High Energy Astrophys. **17**, 38 (2018).
[97] R. C. dos Anjos *et al.*, Ultrahigh-energy cosmic ray composition from the distribution of arrival directions, Phys. Rev. D **98**, 123018 (2018).
[98] P. Sommers, Cosmic ray anisotropy analysis with a full-sky observatory, Astropart. Phys. **14**, 271 (2001).
[99] A. Aab *et al.* (Telescope Array, Pierre Auger Collaboration), Searches for large-scale anisotropy in the arrival directions of cosmic rays detected above energy of 10^{19} eV

at the Pierre Auger Observatory and the Telescope Array, Astrophys. J. **794**, 172 (2014).
[100] A. Aab *et al.* (Pierre Auger Collaboration), multiresolution anisotropy studies of ultrahigh-energy cosmic rays detected at the Pierre Auger Observatory, J. Cosmol. Astropart. Phys. 06 (2017) 026.
[101] L. A. Anchordoqui, C. Hojvat, T. P. McCauley, T. C. Paul, S. Reucroft, J. D. Swain, and A. Widom, Full—sky search for ultrahigh-energy cosmic ray anisotropies, Phys. Rev. D **68**, 083004 (2003).
[102] J. F. Soriano, L. A. Anchordoqui, and D. F. Torres, The Galactic magnetic field in the light of starburst-generated ultrahigh-energy cosmic rays, Proc. Sci., ICRC2019 (**2019**) 254 [arXiv:1907.06207].
[103] A. Aab *et al.* (Pierre Auger Collaboration), *The Pierre Auger Observatory: Contributions to the 36th International Cosmic Ray Conference (ICRC 2019)* (2019).
[104] W. H. Baumgartner, J. Tueller, C. B. Markwardt, G. K. Skinner, S. Barthelmy, R. F. Mushotzky, P. A. Evans, and N. Gehrels, The 70 month Swift-BAT all-sky hard x-ray survey, Astrophys. J. Suppl. Ser. **207**, 19 (2013).
[105] J. P. Huchra *et al.*, The 2MASS redshift survey—Description and data release, Astrophys. J. Suppl. Ser. **199**, 26 (2012).
[106] P. Abreu, M. Aglietta, E. J. Ahn, D. Allard, I. Allekotte, J. Allen, J. A. Castillo, J. Alvarez-Muñiz, M. Ambrosio, and A. Aminaei (Pierre Auger Collaboration), Update on the correlation of the highest energy cosmic rays with nearby extragalactic matter, Astropart. Phys. **34**, 314 (2010).
[107] P. Abreu *et al.* (Pierre Auger Collaboration), Measurement of the Proton-Air Cross-Section at $\sqrt{s} = 57$ TeV with the Pierre Auger Observatory, Phys. Rev. Lett. **109**, 062002 (2012).
[108] J. F. Soriano, L. A. Anchordoqui, and D. F. Torres, The photodisintegration of ^{4}He on the cosmic microwave background is less severe than earlier thought, Phys. Rev. D **98**, 043001 (2018).
[109] R. Ulrich (Pierre Auger Collaboration), Extension of the measurement of the proton-air cross section with the Pierre Auger Observatory, Proc. Sci., ICRC2015 (**2016**) 401.
[110] A. Aab *et al.* (Pierre Auger Collaboration), *The Pierre Auger Observatory: Contributions to the 34th International Cosmic Ray Conference (ICRC 2015)* (2015), http://lss.fnal.gov/archive/2015/conf/fermilab-conf-15-396-ad-ae-cd-td.pdf.
[111] A. M. Sirunyan *et al.* (CMS Collaboration), Measurement of the inelastic proton-proton cross section at $\sqrt{s} = 13$ TeV, J. High Energy Phys. 07 (2018) 161.
[112] M. Aaboud *et al.* (ATLAS Collaboration), Measurement of the total cross section from elastic scattering in pp collisions at $\sqrt{s} = 8$ TeV with the ATLAS detector, Phys. Lett. B **761**, 158 (2016).
[113] G. Bertone, D. Hooper, and J. Silk, Particle dark matter: Evidence, candidates and constraints, Phys. Rep. **405**, 279 (2005).
[114] J. L. Feng, Dark matter candidates from particle physics and methods of detection, Annu. Rev. Astron. Astrophys. **48**, 495 (2010).
[115] M. Klasen, M. Pohl, and G. Sigl, Indirect and direct search for dark matter, Prog. Part. Nucl. Phys. **85**, 1 (2015).
[116] T. M. Undagoitia and L. Rauch, Dark matter direct-detection experiments, J. Phys. G **43**, 013001 (2016).
[117] O. Buchmueller, C. Doglioni, and L. T. Wang, Search for dark matter at colliders, Nat. Phys. **13**, 217 (2017).
[118] B. Penning, The pursuit of dark matter at colliders—An overview, J. Phys. G **45**, 063001 (2018).
[119] S. Rappoccio, The experimental status of direct searches for exotic physics beyond the standard model at the Large Hadron Collider, Rev. Phys. **4**, 100027 (2019).
[120] M. Garny, M. Sandora, and M. S. Sloth, Planckian Interacting Massive Particles as Dark Matter, Phys. Rev. Lett. **116**, 101302 (2016).
[121] M. Garny, A. Palessandro, M. Sandora, and M. S. Sloth, Theory and phenomenology of Planckian interacting massive particles as dark matter, J. Cosmol. Astropart. Phys. 02 (2018) 027.
[122] E. Alcantara, L. A. Anchordoqui, and J. F. Soriano, Hunting for superheavy dark matter with the highest-energy cosmic rays, Phys. Rev. D **99**, 103016 (2019).
[123] D. J. H. Chung, E. W. Kolb, A. Riotto, and I. I. Tkachev, Probing Planckian physics: Resonant production of particles during inflation and features in the primordial power spectrum, Phys. Rev. D **62**, 043508 (2000).
[124] K. Kannike, A. Racioppi, and M. Raidal, Superheavy dark matter—Towards predictive scenarios from inflation, Nucl. Phys. **B918**, 162 (2017).
[125] V. Berezinsky, M. Kachelriess, and A. Vilenkin, Ultrahigh-Energy Cosmic Rays without GZK Cutoff, Phys. Rev. Lett. **79**, 4302 (1997).
[126] V. A. Kuzmin and V. A. Rubakov, Ultrahigh-energy cosmic rays: A window to postinflationary reheating epoch of the Universe?, Phys. At. Nucl. **61**, 1028 (1998).
[127] M. Birkel and S. Sarkar, Extremely high-energy cosmic rays from relic particle decays, Astropart. Phys. **9**, 297 (1998).
[128] S. Sarkar and R. Toldra, The high-energy cosmic ray spectrum from relic particle decay, Nucl. Phys. **B621**, 495 (2002).
[129] V. Berezinsky and M. Kachelriess, Monte Carlo simulation for jet fragmentation in SUSY QCD, Phys. Rev. D **63**, 034007 (2001).
[130] C. Barbot and M. Drees, Detailed analysis of the decay spectrum of a super heavy X particle, Astropart. Phys. **20**, 5 (2003).
[131] S. L. Dubovsky and P. G. Tinyakov, Galactic anisotropy as signature of CDM related ultrahigh-energy cosmic rays, JETP Lett. **68**, 107 (1998).
[132] N. W. Evans, F. Ferrer, and S. Sarkar, The anisotropy of the ultrahigh-energy cosmic rays, Astropart. Phys. **17**, 319 (2002).
[133] R. Aloisio and F. Tortorici, Super heavy dark matter and UHECR anisotropy at low energy, Astropart. Phys. **29**, 307 (2008).
[134] O. E. Kalashev and M. Y. Kuznetsov, Heavy decaying dark matter and large-scale anisotropy of high-energy cosmic rays, Pis'ma Zh. Eksp. Teor. Fiz. **106** (2017) 65; [JETP Lett. **106** (2017) 73].
[135] R. Aloisio, S. Matarrese, and A. V. Olinto, Super heavy dark matter in light of BICEP2, Planck and Ultra high

energy cosmic rays observations, J. Cosmol. Astropart. Phys. 08 (2015) 024.
[136] O. K. Kalashev and M. Yu. Kuznetsov, Constraining heavy decaying dark matter with the high energy gamma-ray limits, Phys. Rev. D **94**, 063535 (2016).
[137] T. W. B. Kibble, Topology of cosmic domains and strings, J. Phys. A **9**, 1387 (1976).
[138] V. Berezinsky, E. Sabancilar, and A. Vilenkin, Extremely high energy neutrinos from cosmic strings, Phys. Rev. D **84**, 085006 (2011).
[139] J. P. Conlon and F. Quevedo, Astrophysical and cosmological implications of large volume string compactifications, J. Cosmol. Astropart. Phys. 08 (2007) 019.
[140] S. S. AbdusSalam, J. P. Conlon, F. Quevedo, and K. Suruliz, Scanning the landscape of flux compactifications: Vacuum structure and soft supersymmetry breaking, J. High Energy Phys. 12 (2007) 036.
[141] V. A. Ryabov, V. A. Chechin, G. A. Gusev, and K. T. Maung, Prospects for ultrahigh-energy particle observation based on the lunar orbital LORD space experiment, Adv. Space Res. **58**, 464 (2016).
[142] O. Scholten, S. Buitink, J. Bacelar, R. Braun, A. G. de Bruyn, H. Falcke, K. Singh, B. Stappers, R. G. Strom, and R. al Yahyaoui, Improved Flux Limits for Neutrinos with Energies above 10^{22} eV from Observations with the Westerbork Synthesis Radio Telescope, Phys. Rev. Lett. **103**, 191301 (2009).
[143] R. Gandhi, C. Quigg, M. H. Reno, and I. Sarcevic, Neutrino interactions at ultrahigh-energies, Phys. Rev. D **58**, 093009 (1998).
[144] M. M. Block, L. Durand, and P. Ha, Connection of the virtual $\gamma^* p$ cross section of ep deep inelastic scattering to real γp scattering, and the implications for νN and ep total cross sections, Phys. Rev. D **89**, 094027 (2014).
[145] J. L. Christiansen, E. Albin, T. Fletcher, J. Goldman, I. P. W. Teng, M. Foley, and G. F. Smoot, Search for cosmic strings in the COSMOS survey, Phys. Rev. D **83**, 122004 (2011).
[146] R. van Haasteren *et al.*, Placing limits on the stochastic gravitational-wave background using European Pulsar Timing Array data, Mon. Not. R. Astron. Soc. **414** (2011) 3117; Erratum, Mon. Not. R. Astron. Soc. **425**, 1597 (2012).
[147] T. Damour and A. Vilenkin, Gravitational radiation from cosmic (super)strings: Bursts, stochastic background, and observational windows, Phys. Rev. D **71**, 063510 (2005).
[148] S. Olmez, V. Mandic, and X. Siemens, Gravitational-wave stochastic background from Kinks and Cusps on cosmic strings, Phys. Rev. D **81**, 104028 (2010).
[149] N. P. Ilina, N. N. Kalmykov, and V. V. Prosin, Cherenkov radiation and parameters of extensive air showers, Yad. Fiz. **55**, 2756 (1992); [Sov. J. Nucl. Phys. **55**, 1540 (1992)].
[150] D. Heck, J. Knapp, J. N. Capdevielle, G. Schatz, and T. Thouw, CORSIKA: A Monte Carlo code to simulate extensive air showers, Tech. Report No. FZKA-6019, 1998.
[151] N. N. Kalmykov and S. S. Ostapchenko, The Nucleus-nucleus interaction, nuclear fragmentation, and fluctuations of extensive air showers, Yad. Fiz. **56**, 105 (1993) [Phys. At. Nucl. **56**, 346 (1993)].
[152] M. Nagano, K. Kobayakawa, N. Sakaki, and K. Ando, New measurement on photon yields from air and the application to the energy estimation of primary cosmic rays, Astropart. Phys. **22**, 235 (2004).
[153] F. X. Kneizys, E. Shettle, L. W. Abreu, J. H. Chetwynd, and G. P. Anderson, User guide to LOWTRAN 7, Air Force Geophysics Laboratory Tech. Report No. AFGL-TR-88-0177, 1988.
[154] C. Berat, S. Bottai, D. De Marco, S. Moreggia, D. Naumov, M. Pallavicini, R. Pesce, A. Petrolini, A. Stutz, and E. Taddei, ESAF: Full simulation of space-based extensive air showers detectors, Astropart. Phys. **33**, 221 (2010).
[155] G. Abdellaoui *et al.*, Cosmic ray oriented performance studies for the JEM-EUSO first level trigger, Nucl. Instrum. Methods Phys. Res., Sect. A **866**, 150 (2017).
[156] J. H. Adams *et al.* (JEM-EUSO Collaboration), Performances of JEM-EUSO: energy and X_{max} reconstruction, Exp. Astron. **40**, 183 (2015).
[157] F. Fenu (Pierre Auger Collaboration), The cosmic ray energy spectrum measured using the Pierre Auger Observatory, Proc. Sci., ICRC2017 (**2018**) 486.
[158] L. Arbeletche and V. de Souza, On the parametrization of the distributions of depth of shower maximum of ultrahigh energy extensive air showers, Astropart. Phys. **116**, 102389 (2020).
[159] S. Ostapchenko, Monte Carlo treatment of hadronic interactions in enhanced Pomeron scheme: I. QGSJET-II model, Phys. Rev. D **83**, 014018 (2011).
[160] T. Pierog, I. Karpenko, J. M. Katzy, E. Yatsenko, and K. Werner, EPOS LHC: Test of collective hadronization with data measured at the CERN Large Hadron Collider, Phys. Rev. C **92**, 034906 (2015).
[161] L. D. Landau and I. I. Pomeranchuk, The limits of applicability of the theory of Bremsstrahlung by electrons and of the creation of pairs at large energies, Dokl. Akad. Nauk SSSR **92**, 535 (1953).
[162] A. B. Migdal, Bremsstrahlung and pair production in condensed media at high-energies, Phys. Rev. **103**, 1811 (1956).
[163] T. Stanev and C. P. Vankov, Air shower detection of ultrahigh-energy muons and neutrinos, Phys. Rev. D **40**, 1472 (1989).